ICRM Technical Series on Radionuclide Metrology
ISSN 2522-4328

INTERNATIONAL COMMITTEE
FOR RADIONUCLIDE METROLOGY

Proceedings of the

22nd International Conference on Radionuclide Metrology and its Applications (ICRM 2019) 27-31 May 2019, Salamanca, Spain

Editors
Uwe Wätjen, Begoña Quintana Arnés
and Eduardo García-Toraño

The International Committee for Radionuclide Metrology (ICRM) is an association of radionuclide metrology laboratories whose membership is composed of delegates of these laboratories together with other scientists (associate members) actively engaged in the study and applications of radioactivity.

It explicitly aims at being an international forum for the dissemination of information on techniques, applications and data in the field of radionuclide metrology. This discipline provides a range of tools for tackling a wide variety of problems in numerous other fields, for both basic research and industrial applications. Radionuclide metrology continues to play an important role in the nuclear industry, supporting activities such as radionuclide production, nuclear medicine, measurement of environmental radioactivity and of radionuclides in food and drinking water, decommissioning of nuclear facilities, nuclear security and emergency preparedness, nuclear physics research, etc.

International Committee for Radionuclide Metrology (ICRM)
http://physics.nist.gov/ICRM/
Ljubljana, Slovenia

Contact information
Denis Glavič-Cindro
ICRM Secretary
E-mail: denis.cindro@ijs.si

Legal notice
Neither the International Committee for Radionuclide Metrology nor any person acting on behalf of the Committee is responsible for the use which might be made of this publication.

ICRM technical series on radionuclide metrology
ISSN 2522-4328
URL: https://physics.nist.gov/ICRM/ICRM_technicalseries_2.pdf

Contents

Proceedings of the 22nd International Conference on Radionuclide Metrology and its Applications (ICRM 2019), 27-31 May 2019, Salamanca, Spain

Editors: Uwe Wätjen, Begoña Quintana Arnés and Eduardo García-Toraño

Contents 3

Preface 5

Conference papers 13

Session: Radionuclide Metrology in Life Sciences

M. Capogni, S. Donatiello, P. De Felice, V. Cannatà, M.C. Garganese, ^{90}Y on-site calibration of the OPBG ionisation chamber 13

F. Juget , Y. Nedjadi, T. Buchillier, T. Durán, F. Bochud, C. Bailat, Efficiency curve of an ionization chamber and its application for short-lived isotope measurement in hospitals 18

Session: Gamma-ray Spectrometry

A. Wadjinny, M.-C. Lépy, PUFI: A tool to prepare geometry files for PENELOPE Monte Carlo simulation in gamma-ray spectrometry 23

T. Vidmar, Sensitivity of TCS correction factors to uncertainty in efficiency values .. 26

Session: Source Preparation Techniques

I.K. Mitsios, M.J. Anagnostakis, A fast method for the determination of ^{7}Be in rainwater and atmospheric humidity samples 29

Session: Measurement Standards and Reference Materials

Yanliang Chen, Chao Zhao, Linfeng He, Fangdong Tang, Preparation of area ^{90}Sr reference sources using Nafion ion exchange membrane 33

Session: Low-level Radioactivity Measurement Techniques

J. Vaquero, J.C. Lozano, M.C. Pedrosa, Implications of the sampling method on the determination of ^{222}Rn in groundwater 37

D. Borrego, B. Quintana, J.C. Lozano, M.C. Pedrosa, M.T. Marcos, Towards a suitable gross α and β activity determination in drinking water 42

Session: Quality Assurance and Uncertainty Evaluation in Radioactivity Measurements

M.A. Saizu, Uncertainty analysis on the response of a thyroid gamma spectrometer using different calibration phantoms 48

Session: Intercomparisons

A. Gudelis, I. Gorina, P. Dryak, Z. Vesela, A. Javornik, M. Krivosik, J. Ometakova, K. Skovorodko, The follow-up intercomparison of the radionuclide calibrators between FTMC, CMI and SMU 52

Appendix:

Conference papers published in *Applied Radiation and Isotopes* 57

PREFACE

This second issue of the ICRM Technical Series on Radionuclide Metrology is devoted to the 22nd International Conference on Radionuclide Metrology and its Applications (ICRM 2019), which was held from 27 - 31 May 2019 at the Hospedería Fonseca, Salamanca, España. The conference was hosted by the University of Salamanca, which had celebrated its 800 years of existence one year earlier (2018). The local organisation was undertaken by a team from the *Departamento de Física Fundamental*. The city of Salamanca provided the ideal setting for this conference. With a very old university tradition, this human-size city has plenty of historical buildings worth visiting and also features numerous places to meet colleagues in an informal atmosphere.

Plenary meetings of the International Committee for Radionuclide Metrology (ICRM) are held biennially and have developed into scientific ICRM conferences, a successful instrument of communication among various specialists, truly encouraging international cooperation, also across borders of their disciplines. This series of meetings dates back to the 1st International Summer School on Radionuclide Metrology which was held in 1972 at Herceg Novi, Yugoslavia. After two previous meetings on radionuclide metrology, organised by the International Atomic Energy Agency (IAEA) in 1959 and 1966, contacts among radionuclide metrologists from several countries had grown stronger at the Herceg Novi summer school bringing forth the idea of a permanent committee to promote applications of radionuclide metrology. ICRM was founded at Paris in 1974, subsequently inviting more laboratories to join, and by 1976 ICRM counted 15 members. More than 40 years later, ICRM has grown to be a truly worldwide association with, at present, 47 member institutions.

The International Committee for Radionuclide Metrology (ICRM) is an association of radionuclide metrology laboratories whose membership is composed of appointed delegates of these laboratories together with other scientists (associate members) actively engaged in the study and applications of radioactivity. It explicitly aims at being an international forum for the dissemination of information on techniques, applications and data in the field of radionuclide metrology. This discipline provides a range of tools for tackling a wide variety of problems in numerous other fields, for both basic research and industrial applications. Radionuclide metrology continues to play an important role in the nuclear industry, supporting activities such as radionuclide production, nuclear medicine, measurement of environmental radioactivity and of radionuclides in food and drinking water, decommissioning of nuclear facilities, nuclear security and emergency preparedness, and nuclear physics research. Papers presented at the ICRM 2019 conference covered the metrological aspects pertaining to many of these fields.

The 22nd International Conference on Radionuclide Metrology and its Applications (ICRM 2019) was attended by 138 participants from 34 countries worldwide and 4 international organisations plus 5 registered sponsors. Of the 166 submitted abstracts, the scientific programme committee had selected 130 contributions for presentation, either as oral (39) or as poster (91). Finally, during the four very busy symposium days from 27 to 31 May, 2 invited talks, 36 oral contributions and 68 posters were presented.

Fig. 1. Conference opening ceremony: (a) Eduardo García-Toraño, ICRM President, Raúl Rivero, Rector of the University of Salamanca (center) and Begoña Quintana, Scientific Secretary of ICRM 2019; (b) The audience

Participants were welcomed during the conference opening by Prof. Raúl Rivero, Rector of the University of Salamanca, Prof. Begoña Quintana, Scientific Secretary of the meeting and by the ICRM President Dr Eduardo García-Toraño. The scientific programme of the conference opened with two invited talks: Prof. J.A. Flores Villarejo from University of Salamanca who lectured on *"Deciphering the age of the ocean"* and Dr Emilio Prieto from the Spanish Center for Metrology (CEM) who discussed *"The New International System of Units"*. The scientific programme continued with a session on Radionuclide Metrology in Life Sciences followed by all other sessions covering the fields in which ICRM is active during the four days of the scientific conference.

Whereas much of the presented work was published in Applied Radiation and Isotopes[1],

[1] Applied Radiation and Isotopes, Vol. 153 (Nov. 2019) – Vol. 167 (Jan. 2021), see the Appendix for a detailed list.

ten papers are published in this issue of the ICRM Technical Series on Radionuclide Metrology. They were only accepted after a very rigorous reviewing process to standards comparable to the review of papers for Applied Radiation and Isotopes. As foreseen in 2017, the number of contributions to the present issue far exceeds that of the first one. This is due to the increasing constraints on the publication of papers coming from conference proceedings in any journal.

Fig. 2. Lively coffee break between sessions

Business meetings of all ICRM Working Groups were integrated into the conference programme. An exhibition of scientific equipment, literature and services, exposed by 5 companies, was held during all four symposium days, combined with the scientific poster presentations. The scientific conference was followed by an ICRM Executive Board meeting. The final day was devoted to the General Meeting of the ICRM.

The social programme encompassed an informal get-together on Sunday at the cloister of Colegio Arzobipo Fonseca, a visit to the Historical University building, followed by a welcome reception on Monday, and a conference dinner at Hacienda Zorita, in the countryside, on Wednesday.

Our appreciation and thanks go to all who contributed to this very successful and busy meeting. In particular we recognize the contributions made by Begoña Quintana and her Local Organising Committee. Many thanks are also addressed to the Scientific Programme Committee, the ICRM Executive Board, the ICRM Working Group coordinators, the referees and session chairs, and to the authors of papers. We are particularly thankful to the coordinating referees for the efficient organisation of the review process for their conference sessions. We are indebted for the support received from the hosting institution, Universidad de Salamanca. We are also thankful for the financial support received from the exhibitors and all other sponsors named below.

Fig. 3. Poster presentations: (a) exhibition hall; (b) Vincent Thomas, winner of the Best Poster Award

There are 47 institutions now represented by delegates in the ICRM. The ICRM has no membership fee and no paid secretariat or other staff. Its overall direction is determined by the delegates at General Meetings, which convene usually every two years, during which organisational guidelines and directions for the work programmes are agreed upon. The following officers of ICRM were elected by the delegate members at the General Meeting of 31 May 2019.

President	Brian Zimmerman[2]
Vice-Presidents	John Keightley[3]
	Mikael Hult[4]
	Akira Yunoki[5]
Past President	Eduardo García-Toraño[6]
Secretary	Denis Glavič-Cindro[7]

We express our thanks to Dirk Arnold[8] and Franz Josef Maringer[9] for their contributions as Past President and Secretary, respectively, during their terms.

ICRM activities are largely the responsibility of its working groups. Each group is guided by a coordinator who acts as a centre for ideas and communications and may organise conferences and workshops. There are now eight working groups with the following fields of interest and assigned coordinators:

(1) Radionuclide Metrology Techniques: Ryan Fitzgerald[2], Christophe Bobin[10], John Keightley[3], Steven Bell[3], Ole Nähle[8]
(2) Alpha-Particle Spectrometry: Stefaan Pommé[4]
(3) Gamma-Ray Spectrometry: Marie-Christine Lépy[10]
(4) Life Sciences: Jeffrey T. Cessna[2]
(5) Liquid Scintillation Counting: Karsten Kossert[8]
(6) Low-Level Measurement Techniques: Simon Jerome[11]
(7) Beta-Particle Spectrometry: Xavier Mougeot[10]
(8) Nuclear Decay Data: Mark Kellett[10]

Anyone wishing to participate in ICRM's activities or to receive further information is encouraged to contact one of the officers above. Details of ICRM and its Working Groups are available from the ICRM web site at http://physics.nist.gov/icrm. An ICRM Newsletter reporting activities in the member laboratories is issued biennially. The most recent one, Issue 31 and several past annual Newsletters may be viewed at http://www.lnhb.fr/seminaires-et-publications/icrm-newsletter/.

The next biennial ICRM conference (ICRM 2021) will be held from 31 May to 4 June 2021 in Bucharest, Romania, organised by the National Institute of Physics and Nuclear Engineering Horia Hulubei, IFIN-HH. The contact person of the local organising

[2] National Institute of Standards and Technology, 100 Bureau Drive, MS 8462, Gaithersburg, MD, 20899-8462, USA.
[3] National Physical Laboratory, Hampton Road, Teddington, Middlesex, TW11 0LW, UK.
[4] European Commission, Joint Research Centre, Retieseweg 111, B-2440 Geel, Belgium.
[5] National Metrology Institute of Japan, National Institute of Advanced Industrial Science and Technology, Tsukuba Central 2, 1-1-1, Umezono, Tsukuba, Ibaragi, Japan, 305-8568.
[6] Centro de Investigaciones Energéticas, Medioambientales y Tecnológicas (CIEMAT), Avda. Complutense 40, Madrid 28040, Spain.
[7] Institut Jožef Stefan, Jamova 39, SI-1001 Ljubljana, Slovenia.
[8] Physikalisch-Technische Bundesanstalt, Bundesalle 100, D-38116 Braunschweig, Germany.
[9] Bundesamt für Eich- und Vermessungswesen, Arltgasse 35, 1160 Wien, Austria.
[10] CEA, LIST, Laboratoire National Henri Becquerel (LNE-LNHB), F-91191 Gif-sur-Yvette Cedex, France.
[11] Norges Miljø- og Biovitenskapelige Universitet (NMBU), P.O. Box 5003, NO-1432 Ås, Norway.

committee and Scientific Secretary of the conference is Dr Aurelian Luca (aluca@nipne.ro). The meetings will be open to all interested persons. They will follow guidelines similar to those of ICRM 2019 comprising a general conference on

Fig. 4. a) ICRM 2019 conference dinner; b) Flamenco show and c) our Scientific Secretary in action

radionuclide metrology and its applications that will cover the fields of aspects of international metrology, intercomparisons, measurement standards and reference materials, radionuclide metrology techniques, alpha-particle and beta-particle spectrometry, gamma-ray spectrometry, liquid scintillation counting techniques, nuclear decay data, low-level radioactivity measurement techniques, radionuclide metrology in life sciences, source preparation techniques, and quality assurance and uncertainty evaluation in radioactivity measurements, together with working group meetings that will offer a less formal frame for scientific discussions. We are wishing the organisers and participants of the 23rd edition of the ICRM conference in Bucharest as much success, joy and excitement as we had with the ICRM 2019 conference.

Fig. 5. ICRM 2019 conference photo. Meeting attendees gather at the cloister of Colegio Arzobispo Fonseca

Begoña Quintana Arnés
Laboratorio de Radiaciones Ionizantes-Datación
Universidad de Salamanca
Salamanca, Spain
E-mail address: quintana@usal.es

Eduardo García-Toraño
Ciemat,Madrid, Spain
E-mail address: egtorano@outlook.com

Uwe Wätjen
Kievermondeveld 74, B-2440 Geel, Belgium
E-mail address: Uwe.Watjen@telenet.be

Scientific Programme Committee:

Pablo Arenillas, CNEA, Argentina
Dirk Arnold, PTB, Germany
Christophe Bobin, LNE-LNHB, France
Michel Bruggeman, SCK·CEN, Belgium
Philippe Cassette, LNE-LNHB, France
Jeffrey Cessna, NIST, USA
Teresa Crespo, CIEMAT, Spain
Pierino De Felice, ENEA, Italy
Andrew Fenwick, NPL, UK
Raphael Galea, NRC·CNRC, Canada
Eduardo García-Toraño, CIEMAT, Spain
Mikael Hult, EC-JRC, EU
Simon Jerome, NPL, UK
Steven Judge, BIPM, International
Lisa Karam, NIST, USA
John Keightley, NPL, UK
Mark Kellett, LNE-LNHB, France
Matjaž Korun, JSI, Slovenia
Karsten Kossert, PTB, Germany
Marie-Christine Lépy, LNE-LNHB, France
Aurelian Luca, IFIN-HH, Romania
Franz Josef Maringer, BEV, Austria
Xavier Mougeot, LNE-LNHB, France
Ohle Nähle, PTB, Germany
Tae Soon Park, KRISS, Korea
Stefaan Pommé, EC-JRC, EU
Begoña Quintana, U. Salamanca, Spain
Guy Ratel, BIPM, International
Miguel Roteta, CIEMAT, Spain
Octavian Sima, Univ. Bucharest, Romania
Milton Van Rooy, NMISA, South Africa
Freda van Wyngaardt, ANSTO, Australia
Uwe Wätjen, Belgium
Akira Yunoki, NMIJ/AIST, Japan
Brian Zimmerman, NIST, USA

Coordinating referees:

Christophe Bobin, LNE-LNHB, France
Michel Bruggeman, SCK·CEN, Belgium
Jeffrey Cessna, NIST, USA
Pierino De Felice, ENEA, Italy
Ryan Fitzgerald, NIST, USA
Mikael Hult, EC-JRC, EU
Simon Jerome, NPL, UK
Steven Judge, BIPM, International
Lisa Karam, NIST, USA
John Keightley, NPL, UK
Mark Kellett, LNE-LNHB, France
Karsten Kossert, PTB, Germany
Marie-Christine Lépy, LNE-LNHB, France
Stefaan Pommé, EC-JRC, EU

Financial Support:

Universidad de Salamanca
Instituto de Física Fundamental y Matemáticas (USAL)
Consejo de Seguridad Nuclear

Exhibitors:

ATI Sistemas, La Coruña, España
GAMMA Technical Corporation, Budapest, Hungary
Perkin Elmer, Groningen, The Netherlands
PTW-Freiburg, Freiburg, Germany
Tecnasa Tecnologías Asociadas, Madrid, España

^{90}Y on-site calibration of the OPBG ionisation chamber

Marco Capogni[a,*], S. Donatiello[b‡], P. De Felice[a], V. Cannatà[b], Maria Carmen Garganese[b]

[a] ENEA – Italian National Institute of Ionizing Radiation Metrology (ENEA-INMRI),

Casaccia Research Centre, Via Anguillarese 301 I-00123 Rome (Italy)

[b] Bambino Gesù Children's Hospital (OPBG), Piazza S. Onofrio 4, I-00165 Rome (Italy)

Abstract

The Triple-to-Double-Coincidence-Ratio (TDCR) portable instrument, owned by ENEA-INMRI, was used to carry out an extensive $^{90}YCl_3$ activity calibration of the Ionization Chamber of the OPBG Hospital in Rome. A ^{90}Y master solution was standardized by the TDCR method using the ENEA-INMRI portable TDCR, as transfer instrument, and the Hidex 300SL 'Metro' version counter. This work highlights some issues faced with on-site calibration of instruments, such as ionization chambers, usually used for activity measurements of short-lived radionuclides. The achieved results open interesting perspectives for Nuclear Medicine applications.

Keywords: ^{90}Y, nuclear medicine, TDCR, IC calibration on-site

* Corresponding author: marco.capogni@enea.it; ‡salvatore.donatiello@opbg.net

1. Introduction

Due to the sharp increase in using radiopharmaceuticals in Italy, both for diagnostic and therapy in Nuclear Medicine (NM), an extensive research programme was started at ENEA-INMRI some years ago in the area of activity measurements of short-lived radionuclides (Capogni et al., 2008). This allowed the development of new primary standards of interest for NM and the discovery of new solutions to the problems encountered in on-site calibration of the instruments, such as Ionization Chambers (ICs), gamma cameras, etc., used for activity determination of radiopharmaceuticals directly at a Nuclear Medicine Department (NMD) of a Hospital. In particular, in this work the ENEA-INMRI TDCR portable instrument (Capogni, De Felice, 2014) was used to perform the calibration of the well-type Bambino Gesù Children's Hospital (OPBG) Ionization Chamber (IC) directly on site for a ^{90}Y solution, in chloride form, kindly provided by the Sirtex Medical Limited (North Sydney, Australia) which purchased the radioactive solution from the PerkinElmer company. This manuscript highlights the main technical solutions, in terms of quality control, linearity check, mass determination and the traceability of measurements to primary standards by a portable instrument, provided to meet the specific requests of the remote calibration of a device for a high-energy pure beta emitter. For this purpose, a primary standard of ^{90}Y was also developed at ENEA-INMRI, under high metrological conditions, by using the TDCR absolute technique in Liquid Scintillation (LS) mode; this also permitted the evaluation of the performances of the ENEA-INMRI TDCR counters for Čerenkov radiation (Broda et al., 2007). The entire work was performed within the project MRTDosimetry of the Call Health 2016 of the European Metrology Programme for Innovation and Research (EMPIR) (MRTDosimetry project, 2016).

From a more specific medical point of view, in recent years, ^{90}Y is used in radiometabolic medicine for the treatment of hepatocellular neoplasms and metastases. Although radical treatment for hepatocellular carcinoma, in the absence of metastasis, is represented by resection or liver transplantation, only 10-15% of patients (all ages) are eligible for these types of treatment. The currently-followed methods are based on intra-arterial embolism, using ^{131}I-Lipiodol (Raoul et al., 1994; Chua et al., 2010; Lau et al., 2008) or microspheres marked with ^{90}Y (Riaz et al., 2009; Hilgard et al., 2010). The benefits of this type of therapy consist of a favorable profile of toxicity and the possibility of combining it with other therapies (such as systemic chemotherapy or hepatic resection) without increasing toxicity (Kennedy, Sangro, 2014). Similarly, somatostatin radiolabelled therapy has been, for more than a decade, a promising option for the treatment or dissemination of neuroendocrine neoplasms. Beta emitting radioisotopes, such as ^{131}I and ^{90}Y, are used in the treatment of lymphomas, such as the non-Hodgkin lymphomas, by using radionuclide monoclonal antibodies (Sharkey et al., 2010; Jacene et al., 2007). In Europe, the radioimmuno-conjugated ^{90}Y-Ibritumomab tiuxetan (IDEC-Y2B8, ZevalinR, Schering, Berlin, based on the same Rituximab antibody) is the only approved radiopharmaceutical for the treatment of follicular lymphomas.

2. Experimental methods

The on-site calibration of the well-type OPBG IC (model Capintec CRC-25R) was based on the study of its linearity in a wide activity range, typical useful for nuclear medicine applications (such as activity delivered to patients and/or cross-check calibration between an IC and PET and/or SPECT scanners used in a NMD), and on its calibration by using the ENEA-INMRI portable TDCR counter in LS mode. The characteristics of the $^{90}YCl_3$ master solution, provided by Mr. M. Tapner from Sirtex Company, are indicated in the technical data sheet, as reported in Table 1. The master solution was prepared on 23rd January 2017 with a nominal activity of 2.109 GBq at the calibration date/time of 27th January 2017 17:00 UTC and in a volume of 1.39 mL in 0.05 M HCl contained in a P2 glass vial.

2.1 OPBG IC linearity

Before performing the calibration of the OPBG Ionisation Chamber, a preliminary study of the linearity of its response was carried out by placing a P2-vial, filled with ^{90}Y in the geometry provided by the manufacturer (as shown in Fig. 1), inside the well-type OPBG IC and using the IC vial/syringe-sample holder. Different

readings were taken at different times in a range of nominal activity between 2.7 GBq (Upper Level - UL) and 1.8 MBq (Lower Level - LL). All the recorded readings, I_n, and the readings I_{nc} corrected for the ^{90}Y half-life ($T_{1/2}$ = 2.6684 (13) d) (DDEP Y-90 table, 2014) were compared in order to estimate the percentage deviation $\Delta(\%) = 100*(I_{nc}-I_r)/I_r$ between a reference reading value, I_r, defined around 20 MBq, and each corrected reading I_{nc}.

Fig. 1: $^{90}YCl_3$ master solution in a P2-vial in the manufacturer's geometry.

Table 1: Characteristics of the $^{90}YCl_3$ solution as given in the Technical Data Sheet of the Sirtex company.

Parameter	Product specification (as of production date)	Value at production	Value at calibration
$^{90}Sr/^{90}Y$ activity ratio	< 1.8E-07	< 1.0E-07	2.8E-07
radiochemical purity	≥95%		

2.2 Source preparation for primary standardization

Two different approaches were taken into account to calibrate the OPBG IC. Two sets of sources were prepared to standardize the ^{90}Y master solution: one at the OPBG site and the other one at ENEA INMRI. Both sets were measured in both laboratories by using TDCR counters owned by ENEA-INMRI. In particular, when the ^{90}Y activity of the master solution used for IC calibration, measured in the OPBG IC, reached the nominal value of about 12 MBq, the master P2-vial was weighed at OPBG by using the OPBG electronic balance Sauter August mod. AR 1014 (10^{-4} g precision); this balance calibration was previously checked by the ENEA-INMRI set of mass standards traceable to the Italian National Institute for Metrology Research (INRiM). A first set (high-mass set) of 6 sources were then prepared at the OPBG site: 3 in 10 mL of LS cocktail, contained in 20 mL high performance glass vial, and 3 in 10 mL of distilled water, contained in 20 mL anti-static plastic vials, with masses ranging from 100 to 150 mg, which were weighed by using the balance mentioned above. These sources were directly measured at the OPBG site by using the ENEA-INMRI portable TDCR counter. A second set (low-mass set) of 6 sources, similar to previous ones but with low masses ranging between 22 to 48 mg, were prepared at the ENEA-INMRI Radioactivity Laboratory (ENEA-INMRI-RL) by using a small aliquot (about 250 mg) of the master solution, dispensing in each of them the radioactive aliquots by the pycnometer method and determining the masses using the ENEA-INMRI high precision Mettler Toledo XP56 balance (10^{-6} g precision). The two sets of sources allowed the study of the effect on the activity measurements due to the different precision of the balances used. After all measurements were completed and the ^{90}Y had completely decayed, the original master P2-vial was emptied completely, rinsed with water, put into a fume hood for 48 h and then weighed by using the same OPBG balance mentioned above. This procedure allowed the determination of the mass of the original master solution, which was 1.3830 ± 0.0060 g, and hence the activity of the master solution at the reference date could be determined by the direct measurement of the activity concentration with the TDCR technique.

2.3 ^{90}Y primary activity measurements

Using the three low-mass LS sources prepared at ENEA-INMRI-RL, it was possible to perform direct activity measurements of the ^{90}Y solution by using the ENEA Hidex 300 SL 'Metro' version TDCR detector. This allowed the determination, by an absolute and robust method, of the activity concentration of the master solution with adequate uncertainty. The activity concentration was estimated by a set of 10 repeated measurements for each LS vial. From each measurement it was possible to know the count rate of the Logical Sum of the Double (*D*) coincidences, the Triple (*T*) coincidences and the double coincidences (*AB*, *BC* and *AC*) coming from the three couples of the three *A*, *B*, *C* photomultipliers of the TDCR counter. Furthermore, the ratios *T/AB*, *T/BC* and *T/AC* were computed and used as input to the TDCR07c.for code (TDCR07c, 2012), provided by Dr P. Cassette from LNHB-CEA, to calculate the ^{90}Y double, ε_D, and triple, ε_T, efficiencies for the ENEA-INMRI Hidex TDCR counter and then the activity concentration of the measured sources. The same sources were then measured at the OPBG site by using the ENEA-INMRI TDCR portable instrument. The high mass set of sources, prepared at OPBG, were also measured by the ENEA-INMRI TDCR portable instrument directly on-site and in the HIDEX TDCR counter at ENEA-INMRI.

2.4 On-site IC calibration

Using this new ^{90}Y primary activity standard, the calibration factor, *CF*, for the OPBG IC in the Sirtex P2-vial geometry was then obtained as ratio of the IC readings (in nominal units) and the activity provided by TDCR LS measurements performed at the ENEA-INMRI-RL and directly on OPBG site.

3. Data analysis and results

In this section the main results achieved in this work are presented. In particular, the results of the OPBG IC linearity study, the ^{90}Y activity primary measurements and the OPBG IC calibration are discussed and reported.

3.1 Linearity of the OPBG IC

In Table 2, the recorded readings I_n, the readings I_{nc} corrected for decay and the percentage deviation $\Delta(\%)$ are reported. This table shows a linearity response of the OPBG IC lower than 1.5% from UL to about 10 MBq nominal activity values. The procedure studied here allowed the evaluation of the linearity around the calibration point, selected at 20 MBq, and can be considered as a first such evaluation of the linearity contribution to the uncertainty of the calibration factor of the OPBG IC. Taking into account the results listed in Table 2 it was possible to state that the calibration made at 20 MBq can be extended to the whole linearity activity range of the OPBG IC with an uncertainty lower than 2%.

3.2 Activity measurements

The activity measurement results of the ^{90}Y solution obtained by using the second set of sources prepared at ENEA-INMRI-RL, as described in section 2.3, are reported in Table 3, column (*a*), and the uncertainty budget of these results is reported in Table 4, column (*a*). Typical values of ε_D and ε_T for ^{90}Y measured in LS vials using the Hidex counter were 0.9970±0.0005 and 0.9933±0.0005, respectively.

Table 2: Linearity of the OPBG Ionization Chamber.

I_n (MBq)	I_{nc} (MBq)	Δ (%)
2720	2720,00	-0,36
2230	2704,29	0,22
2030	2710,19	0,01
1026	2711,30	-0,04
945,0	2710,86	-0,02
792,0	2714,72	-0,16
721,5	2712,85	-0,09
616,0	2727,40	-0,63
563,5	2716,68	-0,23
474,0	2734,47	-0,89
440,5	2712,70	-0,09
364,5	2716,19	-0,22
336,0	2713,09	-0,10
166,3	2709,24	0,04
154,0	2708,77	0,06
128,7	2713,01	-0,10
120,4	2745,44	-1,30
99,50	2720,82	-0,39
92,65	2727,00	-0,61
75,70	2714,20	-0,14
70,33	2716,83	-0,24
59,00	2711,91	-0,06
54,40	2705,57	0,18
26,53	2683,19	0,89
20,43	**2710,34**	**0,00**
19,07	2706,55	0,14
16,06	2737,97	-1,02
14,90	2727,17	-0,62
12,47	2712,48	-0,08
11,03	2690,92	0,72
9,48	2695,06	0,56
7,23	2643,79	2,46
4,10	2556,61	5,67
3,84	2551,81	5,85
3,49	2799,83	-3,30
3,22	2766,45	-2,07
2,60	2984,47	-10,11
2,04	2806,59	-3,55
1,79	2603,82	3,93

By knowing the activity concentration reported in Table 3 and the *D* and *T* count rates measured in the ENEA-INMRI Hidex TDCR counter for the anti-static plastic vials, prepared at the ENEA-INMRI-RL, it was possible to determine the ^{90}Y double, ε_D, and triple, ε_T, efficiencies in Čerenkov mode; typical Čerenkov efficiency values obtained for the ENEA-INMRI Hidex counter were 0.6604±0.0041 and 0.4548±0.0028, respectively. The typical *D*-and *T*-count rates, for anti-static plastic vials measured in this counter, were about 2 and 1 kcounts·s^{-1}, respectively, and the typical time of measurement was 1200 s. The uncertainty budget on the Čerenkov efficiency values is mainly due to: counting statistics (0.06%), decay factor correction (0.25%) and activity uncertainty (0.57%).

The activity determined by the ENEA portable TDCR device is in agreement with those measured by the ENEA Hidex TDCR counter to 0.3%, well within the uncertainties of the measurements, confirming the robustness of our method. Using the known activity, it was possible to deduce the Čerenkov efficiencies also for the ENEA-INMRI portable TDCR detector, and we found $\varepsilon_D = 0.6266 \pm 0.0039$ and $\varepsilon_T = 0.3978 \pm 0.0025$. Typical *D*- and *T*-count rates in this detector were 4 and 2 kcounts·s^{-1} and a typical time of measurement was 1200 s. The efficiency uncertainty was estimated as in the previous cases. The first set of sources, prepared at OPBG, was measured on site using the ENEA-INMRI portable TDCR counter and also using the Hidex counter at ENEA-INMRI. The activity concentration results and its uncertainty are reported in Table 3, column (*b*). The detailed uncertainty budget for this measurement is reported in Table 4, column (*b*). The larger uncertainty in the mass was due to the less precise balance used at the OPBG site.

Table 3: ^{90}Y activity concentrations at reference date, carried out at ENEA-INMRI by the TDCR LS primary method, with corresponding relative uncertainties (*k=1*).
(*a*) measurements performed by the ENEA HIDEX 300 SL 'Metro' version TDCR counter in Liquid Scintillation (LS) mode using the low-mass set of sources prepared at ENEA-INMRI-RL.
(*b*) measurements performed by the ENEA-INMRI portable TDCR counter in Liquid Scintillation (LS) mode using the high-mass set of sources directly prepared at the OPBG site.

Primary method/final results	TDCR (LS) (*a*)	TDCR (LS) (*b*)
Activity concentration (Bq·g^{-1})	$8.70 \cdot 10^6$	$8.64 \cdot 10^6$
Combined relative standard uncertainty (%)	0.57	0.77

3.3 OPBG IC Calibration Factor

By the direct ^{90}Y activity measurements presented in section 2.3, discussed in section 3.2 and reported in Table 3, it was possible to calibrate the OPBG Ionization Chamber. In particular, using the activity concentration obtained using the low-mass set of sources, prepared at ENEA-INMRI-RL, a calibration factor $CF = 1.010 \pm 0.013$ of the well-type OPBG IC was determined using the dial setting for ^{90}Y of "48x10" as suggested by the manufacturer. In Table 5, column (*) a detailed uncertainty budget for the OPBG IC calibration factor, determined by using the activity measurements reported in Table 3, column (*a*), is reported. By using the activity concentration value reported in Table 3, column (*b*), obtained by the measurements performed directly at the OPBG site using the ENEA-INMRI portable TDCR and the high-mass set of sources directly prepared at OPBG, we found an OPBG IC calibration factor of $CF = 1.017 \pm 0.014$, as reported in Table 5, column ($^+$), in agreement within the uncertainty with the value obtained previously. All the measurements in the OPBG IC were performed for a volume of the solution equal to 1.39 mL.

4. Discussions and Conclusions

This work highlights the techniques used and the issues encountered in performing on-site calibration of instruments, such as Ionization Chambers, which are used routinely in a Nuclear Medicine Department to measure high-energy pure beta emitters, such as ^{90}Y. Thanks to the close proximity between ENEA-INMRI and OPBG, the differences in providing calibration by using an absolute activity method with an instrument, such as the Hidex TDCR counter, in a

Table 4: Uncertainty assessment for the ^{90}Y activity concentration carried out at ENEA-INMRI by primary TDCR-LS method; *u* is a relative standard uncertainty (*k* = 1).
(*a*) measurements performed by the ENEA HIDEX 300 SL 'Metro' version TDCR counter in Liquid Scintillation (LS) mode using the low-mass set of sources prepared at ENEA-INMRI-RL.
(*b*) measurements performed by the ENEA-INMRI portable TDCR counter in Liquid Scintillation (LS) mode using the high-mass set of sources directly prepared at OPBG site.

Method Counter		TDCR-LS Hidex (*a*)	TDCR-LS portable (*b*)
Uncertainty component	Assessment type	*u* (%)	*u* (%)
counting statistics	A	0.32	0.32
weighing	B	0.25	0.55
dead time	B	0.15	0.15
background	A	0.02	0.10
counting time	B	0.01	0.01
coincidence resolving time	B	0.15	0.20
input parameters and statistical model	B	0.20	0.20
half-life	B	0.10	0.10
decay scheme parameters	B	0.25	0.25
combined uncertainty	A	0.32	0.34
(as quadratic sum of all uncertainty components)	B	0.47	0.69
	total	0.57	0.77

National Metrology Institute (NMI) laboratory or directly at a NMD site, such as using the portable TDCR counter, were also investigated. The comparison was valuable as the same sets of sources, prepared in two different laboratories with two different balances and different precision level, were counted in two different instruments and different environments. The balances used in a NMD and mass determination, being less accurate than in a NMI laboratory, resulted in larger uncertainty (equal to 1.4%) on the calibration factor of the NMD instruments, than that which can be determined at a NMI (equal to 1.3%). This fact is mainly due to the on-site calibration procedure in which a balance typical used at a Nuclear Medicine Department is used to determine the mass of the calibration sources.

Table 5: Uncertainty budget of the OPBG IC calibration factor *CF* determined by the activity concentrations reported *(*)* in Table 3, column *a*, and *(+)* in Table 3, column *b*.

Uncertainty component	Assessment type	*u* (%) *(*)*	*u* (%) *(+)*
primary standardisation	B	0.57	0.77
TDCR counters	B	0.30	0.30
linearity	A	0.90	0.90
current measurements	A	0.60	0.60
position of the vial in the well	B	0.40	0.40
combined uncertainty	A	1.08	1.08
(as quadratic sum of all uncertainty components)	B	0.76	0.92
	total	1.32	1.42

Due to the high activities (ranging between a few GBq to tens of MBq) usually measured in an IC used in a NMD of a Hospital and the small activities (lower than tens of kBq) that can be measured by the ENEA-INMRI portable TDCR device, it was necessary to perform a preliminary study of the linearity of the OPBG IC. This was necessary in order to select the best calibration working point which allowed the linking of measurements performed in the TDCR counter with the readings of the OPBG IC. On-site activity measurements carried out by the TDCR technique can suffer limitations due to the fact that the typical activity range, few tens of kBq, which can be measured by a TDCR counter, does not cover the whole range of an IC used for radiopharmaceutical activity measurements. However, the typical working range of a portable TDCR can be extended by using higher performance electronics associated with the counter and using the Čerenkov technique for measurement in secondary mode. When this is possible, for example with high-energy beta emitters such as ^{90}Y, it is also easier to prepare the calibration sources on-site. TDCR Čerenkov efficiencies, which were also measured in this study, can be calculated by direct computation using the Monte Carlo method or an analytical code for the TDCR method based on the Frank and Tamm theory of Čerenkov light (Kossert, 2010), and in this case the relative uncertainty can be reduced. This aspect is, in fact, under investigation at ENEA-INMRI and can contribute to open interesting perspectives in the field of on-site activity measurements for pure beta emitters used as emerging radiopharmaceuticals in NM.

Acknowledgments

The authors are very grateful to Mr M. Tapner from Sirtex for supporting this work by providing ^{90}Y raw material which allowed an accurate study of the linearity of the OPBG IC and accurate and precise activity measurements by the ENEA-INMRI TDCR counters. This work was carried out within the MRTDosimetry project of the Call Health 2016 funded by the European Metrology Programme for Innovation and Research (EMPIR).

References

Broda, R., Cassette, P., Kossert, K., 2007. Radionuclide metrology using liquid scintillation counting. Metrologia 44, S36-S52.

Capogni, M., De Felice, P., Fazio, A., 2008. New procedures for radionuclide impurity determination and traceability of activity measurements of short-lived radiopharmaceuticals. Proceedings of the International Workshop 'Traceability to support CIPM MRA and other international arrangements' organized by the Imeko Technical Committee 8 'Traceability in Metrology', 6-7 November, Torino, Italy.

Capogni, M., De Felice, P., 2014. A prototype of a portable TDCR system at ENEA. Appl. Radiat. Isot. 93, 45-51.

Chua, T.C., Chu, F., Butler, S.P., Quinn, R.J., Glenn, D., Liauw, W., Morris, D.L., 2010. Intra-arterial iodine-131-lipiodol for unresectable hepatocellular carcinoma. Cancer 116, 4069-4077.

DDEP Y-90 table, 2014.
http://www.nucleide.org/DDEP_WG/Nuclides/Y-90_tables.pdf

Hilgard, P., Hamami, M., Fouly, A.E., Scherag, A., Müller, S., Ertle, J., Heusner, T., Cicinnati, V.R., Paul, A., Bockisch, A., Gerken, G., Antoch, G., 2010. Radioembolization with yttrium-90 glass microspheres in hepatocellular carcinoma: European experience on safety and long-term survival. Hepatology 52(5), 1741-1749.

Jacene, H.A., Filice, R., Kasecamp, W., Wahl, R.L., 2007. Comparison of ^{90}Y-ibritumomab tiuxetan and ^{131}I-tositumomab in clinical practice. J. Nucl. Med. 48, 1767-1776.

Kennedy, A.S., Sangro, B., 2014. Nonsurgical Treatment for Localized Hepatocellular Carcinoma. Curr. Oncol. Rep. 16(3), 373.

Kossert, K., 2010. Activity standardization by means of a new TDCR-Čerenkov counting technique. Appl. Radiat. Isot. 68(6), 1116-1120.

Lau, W.Y., Lai, E.C., Leung, T.W., Yu, S.C., 2008. Adjuvant intra-arterial iodine-131-labeled lipiodol for resectable hepatocellular carcinoma: a prospective randomized trial-update on 5-year and 10-year survival. Ann. Surg. 247, 43-48.

MRTDosimetry project, 2016. http://mrtdosimetry-empir.eu/

Raoul, J.L., Guyader, D., Bretagne, J.F., Duvauferrier, R., Bourguet, P., Bekhechi, D., Deugnier, Y.M., Gosselin, M., 1994. Randomized controlled trial for hepatocellular carcinoma with portal vein thrombosis: intra-arterial iodine-131-iodized oil versus medical support. J. Nucl. Med. 35(11), 1782-1787.

Riaz, A., Kulik, L., Lewandowski, R.J., Ryu, R.K., Giakoumis Spear, G., Mulcahy, M.F., Abecassis, M., Baker, T., Gates, V., Nayar, R., Miller, F.H., Sato, K.T., Omary, R.A., Salem, R., 2009. Radiologic-pathologic correlation of hepatocellular carcinoma treated with internal radiation using yttrium-90 microspheres. Hepatology 49(4),1185-1193.

Sharkey, R.M., Karacay, H., Goldenberg, D.M., 2010. Improving the treatment of non-Hodgkin lymphoma with antibody-targeted radionuclides. Cancer 116 (4 Suppl), 1134–1145.

TDCR07c, 2012.
http://www.nucleide.org/ICRM_LSC_WG/icrmsoftware.htm

Efficiency curve of an ionization chamber and its application for short-lived isotope measurement in hospitals

Frédéric Juget , Youcef Nedjadi, Thierry Buchillier, Teresa Durán, François Bochud, Claude Bailat

Institute of Radiation Physics, Grand Pré 1, 1007 Lausanne, Switzerland

Abstract

The Institute of Radiation Physics (IRA) developed, in collaboration with the Federal Institute of Metrology (METAS), a portable ionization chamber (TCIR), with measurements traceable to its reference ionization chamber (CIR). The TCIR is designed to be movable to hospitals to measure the activity of samples with around 1% standard uncertainty.
We used the TCIR to calibrate on-site automatic injectors for F-18, Ga-68 and Rb-82 in Swiss hospitals. For F-18, the calibration coefficient of the TCIR is determined using samples traceable to international standards through the Swiss reference ionization chamber (CIR). However, the rather short half-life of Rb-82 (76s) precludes a similar procedure. Its calibration coefficient was obtained using a calculated efficiency curve of the ionization chamber, which has been validated during the last couple of years with long-lived radioisotopes.
The functional form of the CIR's efficiency curve was determined using measurements of more than 20 isotopes. Since the CIR and TCIR have similar chambers (Centronic IG11 and IG12 respectively), the efficiency curve of the latter was assumed to be a normalized version of the former. The normalizing procedure involved using Co-57, Co-60, Tc-99m, I-131, Cs-137 and F-18 TCIR measurements. The resulting curve was used to calculate the calibration coefficients for Ga-68 and Rb-82, which were used to calibrate automatic injectors on-site in three hospitals in Switzerland.
We compared the activity measured by the embedded dose calibrators of the injectors to aliquots measured in the TCIR. The agreement was around 1% for Ga-68, 0.4% for Rb-82 and 3% for F-18.

Keywords: Ionization chamber, Efficiency curve, short-lived nuclides, on-site measurement, nuclear medicine, Ga-68, Rb-82

* Corresponding author, e-mail address: Frederic.Juget@chuv.ch (F. Juget)

1. Introduction

The institute of radiation physics (IRA) developed a portable ionization chamber (TCIR) to measure the activity of short-lived radionuclide samples on-site, which is tailored for nuclear medicine departments or isotope production centers, and has around 1% standard uncertainty (Juget, 2018). This instrument consists of an ionization chamber read directly by an electrometer. The chamber was calibrated using F-18, Tc-99m, I-131, Cs-137, Co-57 and Co-60 samples traceable to international standards through the Swiss reference ionization chamber (CIR). In order to extend the measurement to any gamma emitters, in particular for short half-life isotopes used in hospitals, and since the CIR chamber is a Centronic IG11 (Centronic LTD, Croydon, United-Kingdom) which is similar to the Centronic IG12 used for the TCIR, we first calculated the efficiency curve of the CIR, using more than 20 isotopes. More details about the CIR ionization chamber are given in (Gostely, 1992) and (Juget, 2016). The form of the resulting curve was used for the TCIR after it with the F-18, Tc-99m, I-131, Cs-137, Co-57 and Co-60 TCIR currents. Then, this curve was used to calculate calibration coefficient for Rb-82 and Ga-68. This paper reports our method to calculate the efficiency curve for the CIR and TCIR as well as the measurement of F-18, Ga-68 and Rb-82 performed on-site in nuclear medicine department in three hospitals in Switzerland, where automatic injectors are used to measure the activity injected to patients.

2. Instruments and methods

2.1 Efficiency curve for the CIR

The ionization current produced in the chamber depends on the nature of the gas, the chamber geometry, the source container and the energy and emission probabilities of each gamma emitted from the source. We assume that the efficiency ε(E) for a gamma with energy E is given by:

$$\varepsilon(E) = (aE^b + cE^d)exp\left[-\left(\frac{E}{e}\right)^f\right]$$

where a, b, c, d, e, f are parameters to be determined by fitting procedure and E is the gamma energy. This efficiency curve is empirical and not based on physical considerations (Švec, 2002). In the case of β+ emitter, the following term is used for the emission at 511 keV:

$$\varepsilon = \varepsilon(511\ keV) * (1 + \mu/E_{\beta^+}^{Max})$$

where μ is a parameter and $E_{\beta^+}^{Max}$ is the end-point energy of the positron spectrum. This function takes into account the influence of the energy on the location of the annihilation process, which corresponds to a change of the effective geometry (Niedergesäß, 2011).

To know the current produced for a given isotope, we have to sum up the contributions of all gamma and beta emissions. The efficiency for an isotope N is then:

$$\varepsilon_{N=} \sum_i P_i(E_i)\varepsilon_i(E_i) + \sum_j P_{\beta_j}\varepsilon_{\beta_j}$$

where P_i is the emission probability of gamma emission i with energy E_i. P_β is the emission probability of the electron and E_β its energy. Actually, the electron contribution is small compared to the gamma one. A 500 keV electron will produce a current of 0.1 pA/MBq which corresponds to less than 1% of the current produced by a gamma of 100 keV (Gostely, 2000). In what follows we therefore neglect the electrons contribution as all the isotopes used in this study have only low energy electrons.

The global shape of the efficiency curve is first obtained using a Monte Carlo simulation performed with GEANT software, which takes into account the full geometry of the chamber including the glass ampoule containing the radioactive source (Gostely, 2000).

The obtained curve is matched to the following mono-gamma emitters responses, Cs-137, Tc-99m, Cd-109, Cr-51, F-18, Mn-54 at 661, 140, 88, 320, 511 and 834 keV respectively. Then, the final curve is obtained using all the isotopes measured in the chamber, which are I-131, Cs-137, Co-60, Co-57, Tc-99m, Ba-133, Cd-109, Ce-139, Cr-51, Cs-134, I-125, Lu-177, Mn-54, Yb-169, I-123, Ho-166m, Ir-192, Eu-152, Zn-65, and Y-88 to which we add the following β^+ emitters, Ga-68, F-18 and Na-22.

For the CIR the calibration coefficient, called equivalent activity A_e, is defined as the activity needed for a given nuclide to produce a current of 750 pA. The relation between ε_N and A_e can be written:

$$\varepsilon_N = 1/A_e = \sum_i p_i(E_i)\varepsilon_i(E_i)$$

The probabilities p_i of the gamma emissions are taken from the Decay Data Evaluated Project (DDEP, 2019).

The fit is performed using the Microsoft Excel Solver (Solver, 2019), which minimizes the following quantity using a least-squares method:

$$\sum \frac{(\frac{1}{A_e} - \varepsilon_N)^2}{\varepsilon_N}$$

Figure 1 gives the efficiency curve after the fitting procedure and Table 1 gives all the calibration coefficients obtained with the curve as well as the comparison with the measured values.

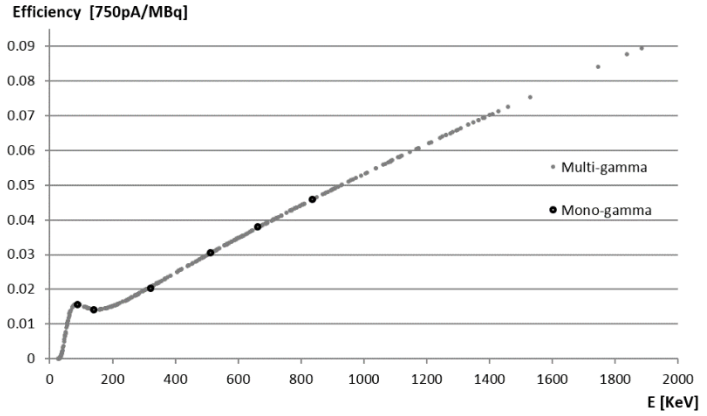

Fig. 1: Efficiency curve for the CIR.

All the differences between the measured and calculated values are less than or equal to 2% except for Lu-177 (6.35%) and Y-88 (3.90%). For the latter isotope, the difference comes from a poor estimate of the curve at high energy. Indeed, we have only a few points to fit the curve in this region and it may be overestimated. Y-88 has a significant peak at 1836 keV (99.346%) and another at 2734 keV (0.608%); it is the only isotope in our list with significant energy peaks above 1800 keV. We suspect that the efficiency curve is overestimated at high energies.

As for the Lu-177, the difference can be explained by a poor estimate of the low energy region between 50 and 70 keV which contributes to more than 20% of the total current produced in the chamber by the gammas of the Lu-177.

Thus, it would be nice to have additional low energy and high energy measurement points in order to be able to fit the efficiency curve more precisely. Am-241 is a good candidate for low energies, because even if it has a multitude of peaks, mainly the one at 59.5 keV will contribute to the signal in the chamber. Its other peaks with too low probability or low energy can be neglected.

Table 1: Comparison between the calculated and the measured value of the calibration coefficient using the efficiency curve for the CIR. The last column gives the difference between the measured and the calculated value. The six first rows give the mono-gamma emitters by energy order.

Isotope	A_e [MBq]	s(%)	$1/\varepsilon_N$[MBq]	s(%)	Δε(%)
Cd-109	1766	0.52	1748.51	1.34	- 1.00
Tc-99m	79.64	0.37	79.39	0.54	0.32
Cr-51	498.95	1.8	489.17	2.04	**- 2.00**
F-18	16.91	0.38	16.83	0.66	0.5
Cs-137	30.895	0.16	31.133	0.81	- 0.76
Mn-54	21.662	0.12	21.826	0.13	- 0.05
Na-22	8.4006	0.39	8.3002	0.31	**1.21**
Co-57	71.31	0.31	71.01	0.45	0.42
Co-60	7.9279	0.1	7.8102	0.09	**1.51**
Zn-65	33.5547	0.34	33.1870	0.25	**1.11**
Ga-68	17.47	0.52	17.76	0.74	**- 1.63**
Y-88	7.774	0.41	7.482	0.15	**3.90**
I-123	76.69	0.47	78.26	0.60	**- 2.00**
I-125	9389	0.42	9296.04	1.12	1.00
I-131	41.88	0.5	41.82	2.16	0.01
Ba-133	36.81	0.19	36.97	1.49	- 0.44
Cs-134	11.29	0.5	11.40	0.46	- 1.00
Ce-139	82.86	0.31	83.59	0.47	0.87
Eu-152	15.3118	0.26	15.3208	0.29	- 0.06
Ho-166m	10.1166	0.23	10.2365	0.73	**- 1.23**
Yb-169	26.73	0.11	27.00	0.53	- 1.00
Lu-177	289.51	0.34	309.14	0.67	**- 6.35**
Ir-192	19.0937	0.23	19.0668	1.2	0.14

2.2 Efficiency curve for the TCIR

The TCIR and the CIR have similar chambers using the same gas, Argon at 20 atmospheres pressure, and have the same external diameter and length. They only differ by the inside diameter of their well, which is 25.4 mm for the CIR and 50.7 mm for the TCIR, and therefore, by the source geometry we used, which is a 5 mL ampoule for the CIR and a 10 mL vial for the TCIR (Juget, 2018). Assuming the efficiency curves have a similar shape, the efficiency curve obtained for the CIR is fitted with the Excel Solver to match the TCIR response of the following isotopes: I-131, Cs-137, Co-60, Co-57, Tc-99m and F-18. The calibration coefficient k, given in kBq/pA, and the efficiency, in pA/kBq are then defined as:

$$\varepsilon_N = 1/k = \sum_i p_i(E_i)\varepsilon_i(E_i)$$

In the fitting procedure, we first normalize the curve using the mono-gamma emitters (Cs-137, F-18 and Tc-99m) and then the final fit is performed by minimizing:

$$\sum \frac{(\frac{1}{K} - \varepsilon_N)^2}{\varepsilon_N}$$

where the sum is taken over the six nuclides measured in the chamber. The results given in Figure 2 and in Table 2 show that the difference

between the measured and calculated calibration coefficient is around 1%.

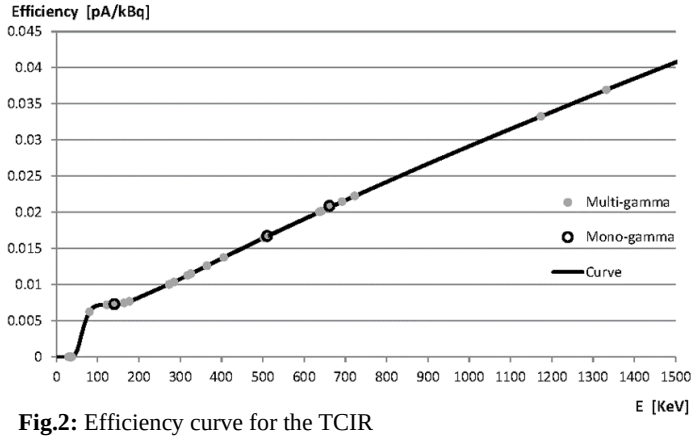

Fig.2: Efficiency curve for the TCIR

In order to validate the efficiency curve, two isotopes, I-123 and Ba-133, are used to compare the measured calibration coefficient and the one predicted using the efficiency curve. A discrepancy lower than 1% is obtained for each isotope which confirms the validity of the efficiency curve (see Table 2).

Table 2: Comparison between the calculated and the measured value of the calibration coefficient using the efficiency curve for the TCIR. The last column gives the difference between the measured and the calculated value.

Isotope	*K* [kBq/pA] (Measured)	s(%)	$1/\varepsilon_N$ [kBq/pA]	s(%)	Δε(%)
I-131	76.88	0.51	76.46	1.54	0.37
Cs-137	56.35	0.18	57.03	1.04	-1.29
Co-60	14.38	0.17	14.31	1.01	0.50
Co-57	146.89	0.32	147.66	1.05	-0.67
Tc-99m	154.98	0.79	156.22	1.14	-1.00
F-18	30.92	0.39	31.08	0.68	-0.66
I-123	147.66	0.71	148.75	1.25	-0.94
Ba-133	75.40	0.76	75.83	1.55	-0.73
Rb-82			27.94	0.68	
Ga-68			32.52	0.76	

As for the CIR, the efficiency curve has to be improved using more isotopes in particular for the low and high-energy parts. However, for the energy range of the main calibration isotopes, typically between 100 kev and 1000 keV, the efficiency curve is accurate. For the calibration coefficients, the uncertainty includes the contributions from the emission probability (DDEP, 2019), the fit (which is around 1%) and the uncertainty of the measured calibration factor (which is below 1%) (see Table 2).

2.3 Calibration coefficient for short half-life isotopes

With the obtained TCIR efficiency curve, we can calculate the calibration coefficient for any isotopes with sufficient gammas, especially for short-lived isotopes that cannot be characterized easily. As the TCIR is for on-site use and in particular in nuclear medicine departments, we were requested to calibrate automated injectors for F-18, Ga-68 and Rb-82 with 1.82890(23) h, 67.83(20) min, and 1.2652(45) min half-lives, respectively. These isotopes are all beta plus emitters with additional gamma contributions in the case of Rb-82 and Ga-68. The calibration coefficients are calculated using the efficiency curve obtained in section 2.2 and the gamma emission probabilities from the DDEP. The resulting values are given in Table 2.

3. Measurements and results

The nuclear medicine departments at Centre Hospitallier Universitaire Vaudois (CHUV) in Lausanne and at Hôpital Neuchâtelois (HNe) in La-Chaux-de-Fonds use an injector, Lemerpax Posijet (Posijet, 2019), for F-18 and Ga-68 injections directly to patients. The TCIR was transported to these hospitals to compare the measurements of the imbedded dose calibrator of the injector with those of the TCIR.

3.1 Measurement in "patient mode" for F-18

The procedure in order to measure directly the prescribed activity at the output of the injector is as follows. For the patient, the injected active solution is first taken from a mother vial with a syringe embedded in the dose calibrator of the Posijet, where its activity is measured. Ten mL are then injected into the patient by mixing a cold solution and the radioactive solution. The syringe is then rinsed twice with 10 mL of cold solution and next injected into the patient. Thus, 30 mL in total are injected. As the TCIR is calibrated only for vials filled at 5 mL (Juget, 2018), the total activity can be measured with the TCIR if all the solution is directly injected successively into 6 vials of about 5 mL. Measuring these 6 vials with the TCIR will give us the total activity injected into the patient.

Each individual vial is weighed first empty and then filled to ensure the radioactive solutions masses are around 5 g. Due to geometrical effects, a filling correction factor has to be applied if the mass is different than 5 g (Juget, 2018). Table 3 gives the results obtained at CHUV for F-18 measurements. It shows that the relative difference between the activity measured in the TCIR and in the Posijet is 3.0%, which is in agreement with the usual precision of dose calibrator measurements (typically a few percent). This procedure was repeated a second time for a total activity of 366.25 MBq measured with the TCIR and 354.95 MBq with the Posijet. The relative difference is 3.1% which confirms the acceptable measurement precision of the dose calibrator of the injector found during the first measurement.

Table 3: F-18 measurement of the 6 vials measured with the TCIR. The uncertainty calculation is explained in (Juget, 2018).

Vial number	Mass [g]	Measured current [pA]	Activity [MBq]	s [MBq]
1	4.785	29.308	0.995	0.004
2	4.785	2631.637	93.621	0.375
3	4.826	3644.79	135.962	0.544
4	4.955	727.001	28.053	0.112
5	5.182	118.641	4.712	0.019
6	4.921	29.364	1.1658	0.005
Sum	**29.454**		**264.509**	**0.671**
Syringe injector measurement			**256.71**	

The same measurement procedure was applied at HNe and the difference found was 1.32%. In addition, after the filling of the last vial we checked if there was some residual activity in the tubes between the syringe and the vial, after dispensing of the 30 mL. The remaining liquid in the tubes was put into a vial, filled with a carrier solution up to 5 mL and measured with the TCIR. The activity found corresponds to 0.2% of the total activity, confirming that all the active solution is well injected into the patient.

These measurements show that our measurement procedure enables the measurement of the activity injected into the patient. In addition, we validated F-18 Posijet calibration coefficients routinely used at the hospitals. However, with this procedure, the filling of the vials requires many manual handlings, which is not appropriate in

routine, due to radiation protection considerations. Nevertheless, this procedure proved the adequacy of the injector.

3.2 Measurement and calibration coefficient for Ga-68

Alternatively, there is a safer (from radiation protection point of view) procedure to calibrate the injector for a given isotope. Instead of filling vials, the procedure involves measuring the activity put into the syringe before dispensing into a patient. First, a vial of 5 mL of the mother solution is measured in the TCIR. The vial is completed up to 10 mL with a carrier solution and the whole solution is put into the syringe. The remaining empty vial is refilled with 5 mL of carrier solution to measure the residual activity with the TCIR. Finally, the difference between the two measurements gives the activity contained in the syringe.

The syringe is then inserted in the dose calibrator of the injector to measure its activity. This value is used as the reference during the usual use of the injector; it corresponds to reference activity injected to the patients. The TCIR activity value is then introduced into the software of the injector which calculates the calibration coefficient.

This procedure was performed at HNe for Ga-68 with an activity of 243.37 ± 2.40 MBq put in the syringe. This value corresponds to the measured value of the vial filled with the mother solution, 249.35 MBq, minus 5.98 MBq, which is the value of the empty vial measured after syringe filling.

Several measurements, at different times, were performed in order to verify the proper functioning of the dose calibrator for the syringe. Table 4 summarizes the values obtained; it demonstrates the validity of the calculated calibration coefficient and the accuracy of the measurement over a large activity range.

Table 4: Ga-68 measurements of the syringe in the dose calibrator of the injector.

Measurement time	Syringe measurement activity	Activity value at reference time 11:46:00	Difference from TCIR measurement
12:25:30	162.7 MBq	243.78 MBq	0.17%
12:32:30	151.2 MBq	243.38 MBq	0.00%
13:38:30	77.48 MBq	245.10 MBq	0.71%

In 2017, Hôpital Universitaire de Genève (HUG) deployed a new medical imaging mobile unit that brings PET-CT imaging (PET-CT, 2017) to hospitals that do not have the financial resources to buy this type of scanner. This mobile unit consists of a truck trailer, containing a state-of-the-art PET-CT scanner, a control room, a waiting room and a robotized injection room. The trailer is towed by a lorry that travels to the places where the examinations are held. The calibration procedure for Ga-68 described previously was applied to this mobile PET-CT scanner which also uses a Posijet injector. A Ga-68 vial with an activity of 202 MBq was used to calibrate the injector and we found a relative difference of less than 3% between the syringe activity measured in the dose calibrator and the TCIR value.

3.3 Measurement of Rb-82

The CHUV uses a RUBY Rubidium Elution system (RUBY, 2019), from the Draximage Company. The injector consists of a generator of Strontium-82, decaying to Rubidium-82. When the generator is eluted, it produces a sterile solution of Rb-82 chloride used for Cardiac Positron Emission Tomography, a non-invasive imaging procedure of the myocardium, to evaluate regional myocardial perfusion in adult patients with suspected or existing coronary artery disease.

The TCIR was moved to CHUV in order to check if the calibration coefficient for this injector is valid. In the injector, the dose calibrator measures the activity of the solution directly after elution in a 35 mL vial. This vial cannot be directly measured in the TCIR because it is not calibrated for this geometry. We therefore collected several 5 mL aliquots of the elution in vials suited for measurements in the TCIR. All vials were weighed before and after filling to determine precisely the mass of solution they contain, and thus enable comparisons of the radioactive concentration of the solution. Given the short half-life of Rb-82 (76 s), measurements were made quickly to minimize uncertainties. Mass measurements of filled vials are performed after decay to avoid useless irradiation during handling. Measurements of the filled vials show that the solution masses were close to 5 g (see Table 5) and therefore it is not necessary to make a filling correction.

After elution, the activity displayed by the dose calibrator of the injector was 405.70 MBq for a solution mass of 21.215 g, giving a concentration of 19.12 MBq/g. Twenty mL of the solution were then transferred into 4 vials which were successively measured in the TCIR. Because of the short half-life, we only measured each vial 3 times for 10 seconds and took the average values. Table 5 summarizes the results. Note that vials 198 and 252 were measured twice.

Table 5: TCIR measurement results for the 4 vials of Rb-82. The uncertainty calculation is explained in (Juget, 2018).

Vial number	Mass [g]	Measured current [pA]	Measured concentration [MBq/g]	s [MBq/g]	Difference to dose calibrator measurement
198	5.209	1127.82	**19.30**	**0.16**	**- 0.94%**
198	5.209	443.08	**19.07**	**0.20**	**0.27%**
214	5.013	137.28	**19.05**	**0.26**	**0.38%**
251	5.130	61.91	**18.92**	**0.30**	**1.06%**
252	4.881	26.90	**18.95**	**0.35**	**0.91%**
252	4.881	14.63	**18.99**	**0.40**	**0.65%**
	Average:		**19.05**	**0.30**	**0.39%**

The results show that the difference between the activity concentration measured for the different vials in the TCIR and that of the dose calibrator is below 1%. The average value over the 6 measurements of the vials is 19.05±0.30 MBq/g, hence 0.39% smaller than the embedded dose calibrator measurement, which validated the calibration coefficient of the dose calibrator. The measurement time between the first and the last vial is 467 seconds, which corresponds to more than 6 half-lives and a decay factor of about 80. This therefore demonstrates the quality of the TCIR since we obtain a good agreement over a large range of measured currents. We also see that the uncertainty increases for the last measured vials; it corresponds mainly to the propagation of uncertainty of the Rb-82 half-life, which is 0.73%.

4. Conclusion

In this study, we calculated the efficiency curve of two reference ionisation chambers over a large range of energies. The precision of the calculation is around 1% for an energy range between 100 keV and 1000 keV. Additionally, isotopes like Am-241 will have to be used to improve the accuracy of the curves at low and high energy.

The calculated efficiency curve was used to calculate calibration coefficients for Rb-82 and Ga-68, which cannot be characterized easily because of their short half-life of 67.83(20) min and 1.2652(45) min, respectively. The TCIR was used to perform on-site measurements to probe the traceability of the activities of solutions injected to patients in a nuclear medicine department. It was moved to three hospitals in Switzerland to calibrate or check automatic injectors of F-18, Ga-68 and Rb-82. Procedures for activity measurements were designed to check the good operation of the injectors as well as for the calculation of the calibration coefficient, if necessary. The agreement between the TCIR measurements and the dose calibrator measurements embedded

in the automatic injector was found to be around 1%. These measurements demonstrated the adequate operation of our TCIR on-site, for short-lived isotopes, and performed for automatic injectors for Ga-68 and Rb-82.

In conclusion, the TCIR is a satisfactorily performing, fast and easy tool to operate and to measure samples on-site. Typically, it can be used to check automatic injectors for a broad range of radionuclides, as its efficiency curve can be used to calculate its calibration factor for any isotope with sufficient gammas.

References

DDEP 2019. http://www.lnhb.fr/donnees-nucleaires/donnees-nucleaires-tableau/

Gostely, J.-J., 1992. A determination of the half-life of ^{137}Cs. Int. J. Radiat. Appl. and Instrum. Part A, Appl. Radiat. Isot. 43, 949-951.

Gostely, J.-J., Laedermann, J.-P., 2000. Simulation of the response of the IG11 4$\pi\gamma$ ionization chamber using GEANT Monte Carlo code. Appl. Radiat. Isot. 52, 447-453.

Juget, F., Nedjadi, Y., Buchillier, T., Bochud F., Bailat C., 2016. Determination of ^{137}Cs with an ionization chamber. Appl. Radiat. Isot. 118, 215-220.

Juget, F., Nedjadi, Y., Buchillier, T., Durán, T., Bochud F., Kottler, C., Bailat C., 2018. A portable precision ionization chamber: The transfer reference chamber. Appl. Radiat. Isot. 134, 95-99.

Niedergesäß, Ch., Schrader, H., Kossert, K., 2011. Untersuchung von Ionisationskammer-Messsystemen für Aktivitätsbestimmungen. PTB-Bericht Ra-46, ISBN 978-3-86918-143-1.

PET-CT, 2017, https://www.hug-ge.ch/en/rapport-activite-2017/medical-imaging

Posijet, 2019, https://www.lemerpax.com/en/products/posijet-en/

RUBY, 2019, https://www.draximage.com/products/us/ruby-fill/

Solver, 2019. https://www.solver.com/

Švec A., Schrader H., 2002, Fitting methods for constructing energy-dependent efficiency curves and their application to ionization chamber measurements. Appl. Radiat. Isot. 56, 237-243.

PUFI: A tool to prepare geometry files for PENELOPE Monte Carlo simulation in gamma-ray spectrometry

Abdellah Wadjinny, Marie-Christine Lépy*

CEA, LIST, Laboratoire National Henri Becquerel (LNE-LNHB), Bât. 602 PC 111, CEA-Saclay 91191 Gif-sur-Yvette Cedex, France

Abstract

The practical use of the general-purpose Monte Carlo code PENELOPE requires the careful preparation of input geometry files to define the experimental conditions. The structure of the geometry file is strictly formatted and the correctness of the geometry definition can be difficult to achieve for new users. Thus a practical interface PUFI (PENELOPE User-Friendly Interface) has been designed to facilitate the preparation of the geometry files for typical cases of gamma-spectrometry simulations with a cylindrical symmetry including detector, volume source and shielding

Keywords: Monte Carlo simulation, PENELOPE, gamma-ray spectrometry

* Corresponding author, e-mail address: marie-christine.lepy@cea.fr

1. Introduction

PENELOPE (Salvat, 2015, Salvat and Fernández-Varea, 2009), is a general-purpose Monte Carlo code which allows simulation of coupled electron-photon transport: it is widely distributed for a wide range of applications in the energy range from a few hundred eV to about 1 GeV. Among these, it is of interest to derive practical information in gamma-ray spectrometry, such as optimization of geometrical arrangement, calculation of detection efficiency, self-attenuation transfer factors or coincidence summing corrections.

PENELOPE must be launched with a steering program, which controls the geometry and the tracking of particles, keeps score of all relevant information, and performs the required averages at the end of the simulation. Two typical steering programs are provided in the distribution package of PENELOPE: PENCYL (which simulates electron-photon transport in cylindrical geometries) and PENMAIN (for generic quadric geometries). In each case, the practical use of PENELOPE requires the careful preparation of input geometry files to define the experimental conditions, generally including different sources and detection and/or absorbing materials. The PENCYL geometry structure is quite simple and easy to implement and its use is recommended for simple cylindrical geometries, since only one input file (including both geometrical and simulation conditions) is necessary. However, to cope with more general cases, the user must use PENMAIN, which requires two input files (one for the geometry, and one for the simulation conditions). In this general case, the structure of the geometry file is very strictly formatted, using quadric surfaces which define different interaction bodies, and the geometry can be difficult to correctly define for new users.

Thus a practical interface PUFI (PENELOPE User-Friendly Interface) has been designed to facilitate the preparation of the PENMAIN geometry files for typical cases with a cylindrical symmetry which include the detector, a volume source and different absorbing materials and shielding. The detector is cylindrical (or a rounded-shape) and can include an internal hole; the volume source can be cylindrical or a Marinelli-type, and the external shielding is cylindrical.

2. PENELOPE input files

The geometry is defined from a text file, which consists of a sequence of blocks defining the different elements (surfaces, bodies or modules) according to a specific format. First, limiting surfaces must be defined: in the case of a cylindrical geometry, these are either planes or cylinders, as shown in Figure 1.

The different "bodies" are then described from the intersection of the pre-defined surfaces. It is necessary to start from the internal bodies and to add successive elements, thus the detector and the source must be defined before including these in the shielding. However, the geometry input can be tedious and errors may be caused if the format strict structure is not followed.

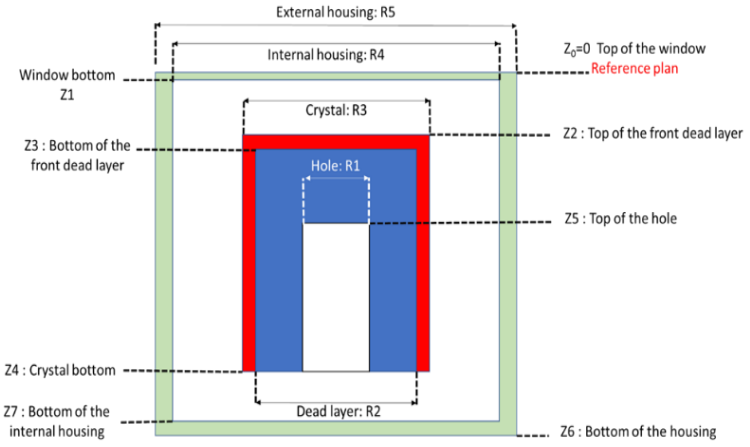

Fig. 1: Typical limiting surfaces in the case of a cylindrical detector

3. PENELOPE User-Friendly Interface (PUFI)

PUFI is the acronym for PENELOPE User-Friendly Interface which was programmed using the Python language. It has been conceived to prepare PENELOPE geometry files in an easy way. As already mentioned, the file structure is specifically formatted and the construction of the geometry must follow an order to mention if there is some intersection between the different bodies. With PUFI, only the typical dimensions of the experimental elements and their relative position are required, and must be input according to a specific order, from internal elements (detector) to external ones (shielding). It should be noted that all dimensions must be entered in millimeters by the user; they are automatically converted into centimeters to cope with the PENELOPE requested format. The PENELOPE geometry file is automatically generated from these elements and the resulting

geometry can be verified using the PENELOPE visualization tool PenGeomjar (Almansa et al., 2016).

4. PUFI practical use

As for any geometry definition, it is recommended to prepare a draft scheme of the experimental arrangement to determine the different elements, materials and relative positions, as presented in Figure 2:

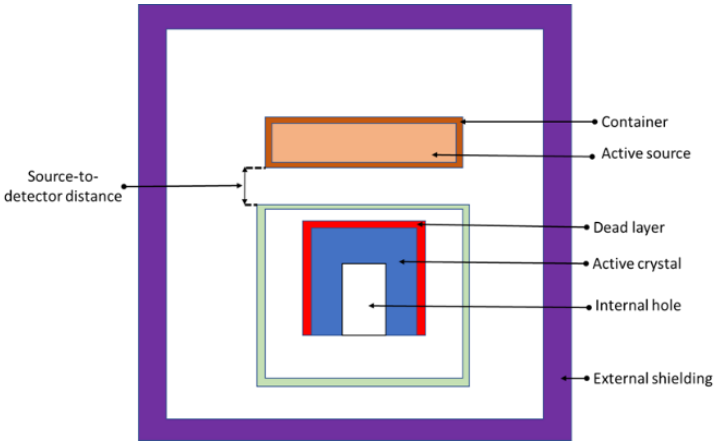

Fig. 2: Typical experimental arrangement including a volume source and a detector installed in a shielding

For the practical use, several basic shapes are pre-defined in PUFI:
- Pure cylinder
- Basic detector (cylinder with a hole and dead layer)
- Container (fully or partially filled)
- Housing (it can be used either for the detector cap or for the external shielding)
- Marinelli container

The main window of PUFI is presented in Figure 3. To prepare the geometry file, you have to select the basic shapes and, for each one, to provide a few characteristic dimensions. The first step consists in defining the detector (crystal and dead layers dimensions) and its position relative to the reference plan. This is obtained by clicking on "Add geometry" and selecting "detector" in the list of pre-defined geometrical shapes.

The basic detector includes three parts: the internal hole, the active crystal and the front dead layer. The dialog window displayed in Figure 4 includes a rough visualization of the requested dimensions and allows to specify which element is the "active body" (in most of case, this is the crystal active volume) and the materials (numbers) of the different elements. (These material numbers are correlated with the ordered list of materials in the input file). Coming back to the main window, the user can input all the characteristic dimensions. At any time, the user can generate and visualize the generated PENELOPE geometry file.

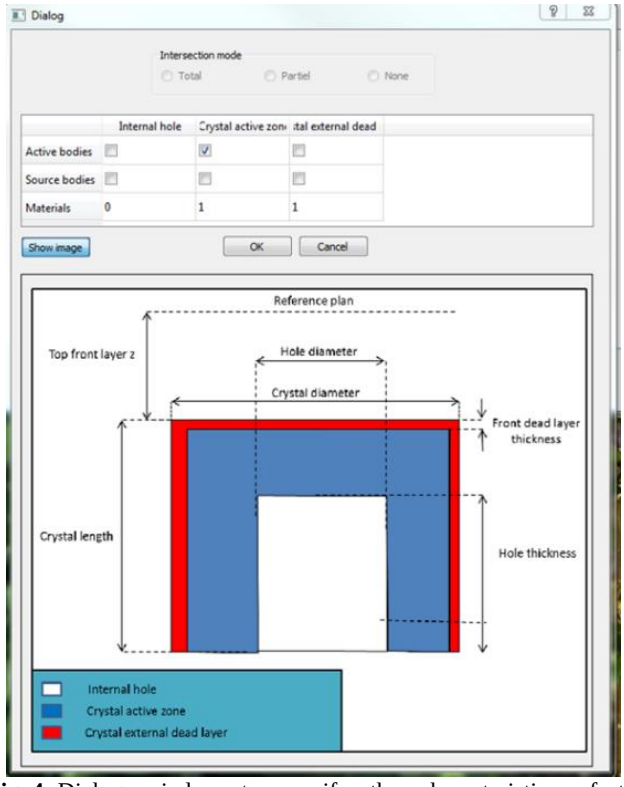

Fig. 4: Dialog window to specify the characteristics of the geometrical elements (case of the detector)

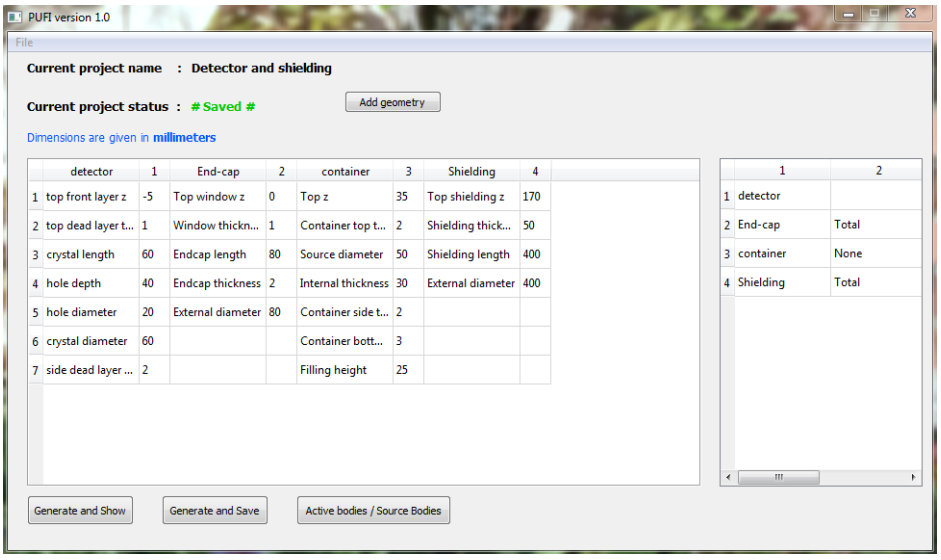

Fig. 3: Main window of PUFI

Once all the elements have been defined, the user can generate the PENELOPE geometry file and save it by clicking on "Generate and save" in the main window. For its practical use with PENELOPE, it can be necessary to use the PenGeomJar application which allows renumbering the different elements in sequential order, using the "Relabel" option, as well as visualizing the defined geometry.

5. Case of rounded detector

To improve the modeling of the detector, the roundness of the crystal entry face must be taken into account, which can be modeled as the intersection of a torus and a cylinder.

The general torus equation is:

$$\left(\sqrt{x^2 + y^2} - R^2\right)^2 + z^2 = r^2$$

where R is the distance between the axis of the cylinder and the center of the torus and r is the radius of the revolution circle generating the torus.

However, this equation is not quadratic and therefore cannot be directly modelled by PENELOPE. To overcome this difficulty, it was chosen to use an approximation method to model the rounding using several cones that can be described by quadratic equations. Figure 5 shows the projection on the plane (y,z) of the intersection of five cones and a cylinder. This structure is included as "rounded detector" in the list of basic shapes.

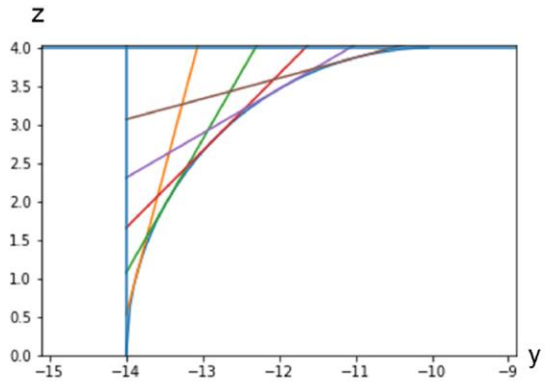

Fig. 5: Approximation of a torus using the intersection of five cones and a cylinder

6. Conclusion

PUFI provides a fast and easy mean to prepare simple PENELOPE geometry files, what should be helpful for the training of new users. The software is available on the LNHB website, together with geometry example files and the user's manual. Some example geometries are taken from the ICRM GSWG Monte Carlo exercise (Lépy et al., 2019), and include two types of detectors and three types of volume sources. The cases of Marinelli container and volume source with an absorbing screen are also included. From these prepared geometries, it is very easy to modify some dimensions directly in the main window to generate new cases: this can be useful to test the influence of changing the dimension of the source or the dead layer thickness, etc. As part of the increasingly frequent use of Monte Carlo simulation, PUFI brings a simple approach to optimize experimental conditions in gamma-ray spectrometry.

References

Almansa, J., Salvat-Pujol, F., Díaz-Londoño, G., Carnicer, A., Lallena, A.M., Salvat, F., 2016. PENGEOM -A general-purpose geometry package for Monte Carlo simulation of radiation transport in material systems defined by quadric surfaces, Computer Physics Communications 199, 102-113. (https://doi.org/10.1016/j.cpc.2015.09.019)

Lépy, M.-C., Thiam, C., Anagnostakis, M., Galea, R., Gurau, D., Hurtado, S., Karfopoulos, K., Liang, J., Liu, H., Luca, A., Mitsios, I., Potiriadis, C., Savva, M.I., Thanh, T.T., Thomas, V., Townson, R., Vasilopoulou, T., Zhang, M., 2019. A benchmark for Monte Carlo simulation in gamma-ray spectrometry. Presented at ICRM 2019, to be published in Applied Radiation and Isotopes

Salvat, F., 2015. PENELOPE-2014: A code System for Monte Carlo Simulation of Electron and Photon Transport, OECD/NEA Data Bank, NEA/NSC/DOC(2015)3. Issy-les-Moulineaux, France. Available from (http://www.nea.fr/lists/penelope.html)

Salvat, F., Fernández-Varea, J. M., 2009. Overview of physical interaction models for photon and electron transport used in Monte Carlo codes. Metrologia 46, S112–S138.

Sensitivity of TCS correction factors to uncertainty in efficiency values

Tim Vidmar *

SCK•CEN, Belgian Nuclear Research Centre, Boeretang 200, 2400 Mol, Belgium

Abstract

True coincidence summing (TCS) corrections are increasingly being calculated rather than measured. According to the established standards the uncertainty of the calculated TCS correction values has to be estimated. We carried out a systematic study of the uncertainty of the TCS correction factors resulting from uncertainty in the input efficiencies for a large number of radionuclides and we find that the relative uncertainty of the TCS correction factors is in general proportional to the value of the correction factor itself.

Keywords: Gamma-ray spectrometry, True coincidence summing corrections, Calculation, Uncertainty

* Corresponding author, e-mail address: tim.vidmar@sckcen.be

1. Introduction

The most accurate way of treating true coincidence summing (TCS) effects in gamma-ray spectrometry is by an application of the so-called relative method (Gilmore, 2008). A standard needs to be prepared that matches the sample in all of its characteristics. These include not only the sample size, density and composition, but also all the radionuclides present in the sample. To determine the activity of a given radionuclide in the sample, the ratio of the count rates in the corresponding peaks in the spectrum of the standard and the sample is established and multiplied by the known activity of the standard. No calculations of the corrections factors are required and the only uncertainties that need to be concerned are those of the standard activity and the two peak areas involved.

For an environmental laboratory dealing with perhaps thousands of samples of varied characteristics per year, this method turns out to be quite impractical. It is much less costly and time consuming to try to calculate the TCS correction factors and limit oneself to the preparation of a limited number of standards to validate the calculations and perhaps improve the detector and sample models used. The uncertainties of these models, i.e., their deviation from reality, are of course a source of the uncertainty of the calculated TCS correction factors. In fact, they constitute an error, a systematic bias that should ideally be corrected for, but this is seldom entirely possible. Instead, the resulting uncertainty (error) can be assessed and propagated to the overall uncertainty budget of the reported activities of the radionuclides present in the sample.

Determining the uncertainty of the individual calculated TCS correction factors is very demanding, especially if it has to be done on a routine basis. It involves the propagation of the particular sample efficiencies involved in the calculation through the decay scheme of the radionuclide in question, since the parameters of the decay scheme enter the formulae for the TCS correction factor value (Gilmore, 2008). Instead, some sort of a general assessment of the magnitude of such uncertainties could be used, especially if they turn out to be not too large and thus not of utmost importance for the overall uncertainty budget. It is the aim of this study to shed light on the main characteristics of the uncertainty in the calculated TCS correction factors in order to facilitate such an assessment.

2. Method

International guidance on the treatment of the uncertainties of TCS correction factors is summarized in Lépy et al, 2015. But to our knowledge, no large scale study of the uncertainty of the TCS correction factors, or better still, their computational sensitivity to input parameters, in particular efficiencies, that would have involved a large number of radionuclides has been conducted so far. Part of the reason may lie with long run times associated with large scale calculations, especially if Monte Carlo simulations are involved. We opted for the EFFTRAN code (Vidmar, 2005; Vidmar et al., 2011), which is one the one hand very fast, and the accuracy and precision of which has on the other hand been validated against other codes (Vidmar et al., 2014; Vidmar et al, 2016) and experimental data (Vidmar, 2019), at least at the level required by a typical environmental gamma-ray spectrometry laboratory.

In the case of a radionuclide that decays with a simple two-step cascade, such as Co-60, the formulae for the TCS correction factors can be easily derived analytically. If we denote the activity of a Co-60 point source by A, the full-energy-peak efficiency at the energies of 1173 keV and 1332 keV by ε_1 by ε_2, respectively, and the corresponding total efficiencies respectively by η_1 and η_2, the count rates in the full energy peak at 1173 keV, which we denote by N_1, can be written as

$$N_1 = A\, \varepsilon_1 (1 - \eta_2). \quad (1)$$

In EFFTRAN, the corresponding TCS correction factor is defined as $C_1 = 1 / (1 - \eta_2)$, so that $N_1 = A\, \varepsilon 1 / C1$. The relative uncertainty of this TCS correction factor therefore depends of the relative uncertainty of the total efficiency η_2:

$$\Delta C_1 = (dC_1 / d\eta_2)\, \Delta \eta_2 = 1 / (1 - \eta_2)^2\, \Delta\eta_2 = C^2\, \Delta\eta_2. \quad (2)$$

We thus arrive at the expression

$$\Delta C_1 / C_1 = C\, \eta_2\, (\Delta\eta_2 / \eta_2). \quad (3)$$

It should be mentioned that this kind of calculation is only true for point sources and small volume elements. For extended sources an

integration over of the products of the efficiencies over the entire sample volume elements has to be carried out in Eq. (1) and in the subsequent derivation, so that the use of the total efficiency of an extended source for the calculation of TCS correction factors is an approximation. The result of Eq. (3) can thus only serve as a general guideline.

The crucial finding is that the relative uncertainty of the TCS correction factor is proportional to its own value and to the total efficiency η_2, as well as to the relative uncertainty of the total efficiency η_2. For a sample measured on a typical medium-size detector we may have $\varepsilon_1 = 0.01$ and $\eta_2 = 0.1$, so that a relative uncertainty of the total efficiency of 10% would translate in a roughly 1% relative uncertainty of the calculated TCS correction factor. This well-known result shows that under the usual circumstances, limited knowledge of the total efficiencies should not be critical for a reasonably accurate assessment of the TCS correction factor by computational means. The question that arises is whether the linear dependence of the relative uncertainty of the TCS correction factor on its own value and on the relative uncertainty of the total efficiency is a general relationship of sorts.

To test this relationship we calculated the TCS correction factors for all the radionuclides whose decay data in contained in the KORDATEN database (Sima and Arnold, 2008) with two different detector models and four different sample models. The characteristics of the models are listed in Tables 1 and 2, and the characteristics of the materials used in their definitions are presented in Table 3.

Table 1: Detector parameters. All dimensions are given in millimetres (mm). The housing diameter is in all cases the same as the window diameter.

Parameter	Detector A	Detector B
Crystal type	p	n
Crystal material	Ge	Ge
Crystal diameter	60	60
Crystal length	60	60
Top dead layer thickness	1	0.0003
Side dead layer thickness	1	0.0003
Hole diameter	10	10
Hole depth	40	40
Window diameter	80	80
Window thickness	1	1
Window material	Al	Al
Crystal-to-window distance	5	5
Housing thickness	1	1

Table 2: Sample parameters. All dimensions are given in millimeters (mm). The container is in all cases, except for the point source, a plastic vessel of 1 mm thickness, tightly encasing the sample on all sides. The point source has no container. The parameter "Distance" refers to the distance between the container and the detector window.

Parameter	Reference	Point	Soil	Filter
Diameter	60	0	90	80
Material	Water	-	Quartz	Cellulose
Height	20	0	40	3
Distance	0	1	0	0

The entire calculation was then repeated by shifting the total efficiency curve as whole up first by 10 per cent, and then by 20 per cent. The change in the TCS correction factors with regard to the original configuration was recorded. The shifts were carried out in the negative direction as well. The same procedure was followed for the full-energy-peak efficiency curve and finally for the combination of the two efficiency curves.

Table 3: Characteristics of various detector and sample materials. All densities are given in g/cm^3.

Material	Density	Chemical formula
Ge	5.323	Ge
Al	2.700	Al
Be	1.848	Be
Water	1.000	H_2O
Quartz	1.400	SiO_2
Cellulose	0.200	$C_6H_{12}O_6$
Polystyrene	1.050	C_8H_9

Table 4: The average uncertainty in the calculated TCs correction factor induced by a shift of the total efficiency curve for a point source positioned on the detector window of the detector model B. Similar dependence on the amount of shift can be seen in the results for detector A.

Sample / Shift	10%	20%
Water	1.3	2.6
Soil	1.9	3.8
Filter	2.2	4.5
Point	3.3	6.9

3. Results and discussion

As expected, the shifting of the full-energy-peak efficiency curve had on average a very limited effect on the calculated TCS correction factors, since the summing-in events occur in general much less frequently than the summing-out ones, and this was true for both for the shifting the full-energy-peak efficiency curve on its own and in combination with a shift of the total efficiency curve. It was the shift of the latter that proved crucial.

Figure 1 shows the distribution of the relative change in the value of the TCS correction factors in the case of a point source measured on the low-energy detector when a shift of the total efficiency curve is performed upwards by 10%. We see that although the majority of the resulting relative uncertainties are within a few per cent, some may reach high values. The average relative change is 3.3%, as listed in Table 4. The same table also gives the related values for other types of samples and as expected the point-source one is the most extreme.

The values also indicate a linear dependence of the induced uncertainty on the amount of shift in the total efficiency curve, at least for not too large values of the shift.

For the same configuration, Figure 2 plots the relative change in the value of the TCS correction factors for all the gamma lines in the KORDATEN database as a function of the TCS correction factor value itself for a uniform shift of +10% (blue) and a uniform shift of +20% (red) of the entire total efficiency curve, respectively.

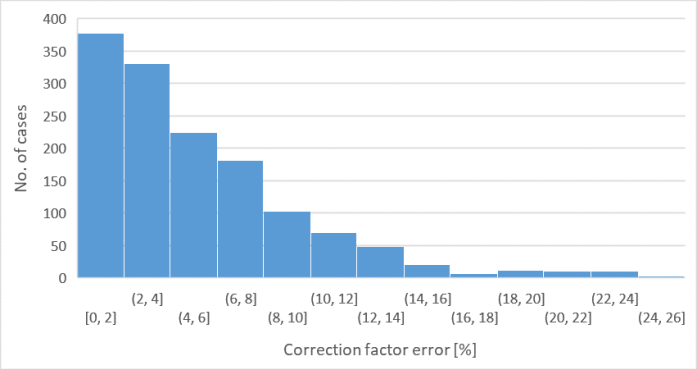

Fig. 1: The distribution of the relative change in the value of the TCS correction factors in the case of a point source measured on the low-energy detector when a shift of the total efficiency curve is performed upwards by 10%.

We can see that the approximately linear dependence on both the value of the TCS correction factor and the uncertainty in the total efficiency is present. Similar plots are obtained for other combinations of a detector and a sample model.

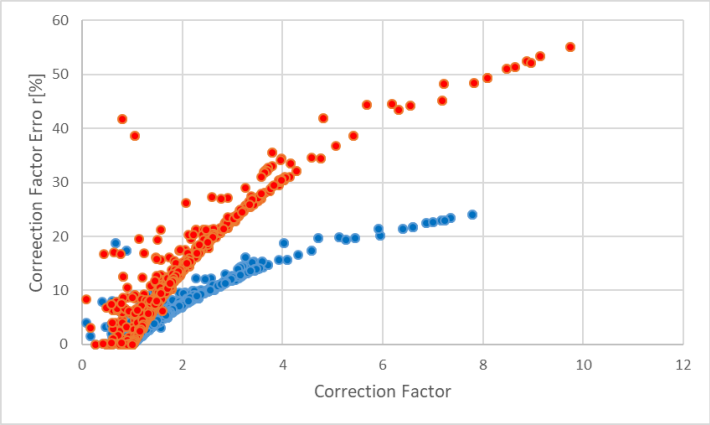

Fig. 2: The relative change in the value of the TCS correction factors in the case of a point source measured on the low-energy detector for all the gamma lines in the KORDATEN database as a function of the TCS correction factor value itself for a shift in the total efficiency of +10% (blue) and of +20% (red), respectively.

4. Conclusions

It appears that a fairly general, albeit approximate, linear relationship exists between the relative error in the calculated values of TCS correction factors due to the lack of precise knowledge of the total efficiency values and the magnitude of the correction factor itself, as long as the uncertainty in the total efficiency is not too large. Even though the uncertainties of the TCS correction factor may not in general be a major contributor to the overall uncertainty budget, in cases when the summing effects are very pronounced, be it due to the specificity of the decay scheme, or geometry of the sample-detector setup, one should pay closer attention to this issue.

References

Gilmore, G., 2008. Practical Gamma-ray Spectrometry, 2nd Edition, J. Wiley and Sons, Ltd., New-York (2008).

Lépy, M-C., et al., 2015. Uncertainties in gamma-ray spectrometry. Metrologia 52, S123-S145.

Sima, O., Arnold, D., 2008. A tool for processing decay scheme data that encompasses coincidence summing calculations. Appl. Radiat. Isot. 66, 705–710.

Vidmar, T., 2005. EFFTRAN—A Monte Carlo efficiency transfer code for gamma-ray spectrometry. Nucl. Instrum. Methods A 550, 603-608.

Vidmar, T., Kanisch, G., Vidmar, G.., 2011. Calculation of true coincidence summing corrections for extended sources with EFFTRAN. Appl. Radiat. Isot. 69, 908-911.

Vidmar, T., et al., 2014. Equivalence of computer codes for calculation of coincidence summing correction factors, Appl. Radiat. Isot. 87, 336-341.

Vidmar, T., et al., 2016. Equivalence of computer codes for calculation of coincidence summing correction factors – PartII Appl. Radiat. Isot. 109, 482-486.

Vidmar T, 2019. Validation of the EFFTRAN code for the calculation of true coincidence summing correction factors. To be published.

A fast method for the determination of ^{7}Be in rainwater and atmospheric humidity samples

Iason K. Mitsios*, Marios J. Anagnostakis

Nuclear Engineering Department, School of Mechanical Engineering, National Technical University of Athens, Iroon Polytechniou 9, 15780, Zografou, Athens, Greece

Abstract

Beryllium-7 is a cosmogenic radionuclide which can be detected in atmospheric aerosols and wet precipitations with gamma spectroscopic techniques. Aim of this study was to develop a method for the fast preparation and analysis of water samples for ^{7}Be determination. For this purpose three procedures were tested employing the mixing of cation exchange resin with the water sample and measuring the resin, or filtering the sample and measuring the filter. Based on the finally adopted procedure, rain, humidity and snow samples were collected and measured.

Keywords: Beryllium-7, rainwater, humidity, resin, gamma spectroscopy

* Corresponding author, e-mail address: iasoniatis@mail.ntua.gr

1. Introduction

Beryllium-7 is a short-lived radionuclide with a half-life of 53.22 days, produced mainly in the stratosphere (~ 70%) and in the troposphere (~ 30%), by spallation reactions of the primary cosmic rays component with the light atmospheric nuclei of C, N and O. It decays by electron capture, emitting 477.6 keV photons with emission probability of 10.44%, through which it may be detected by means of γ-spectrometry (Lal et al., 1958), (Cannizzaro et al., 2004). Beryllium-7 is a useful tracer in atmospheric transport models as well as in the study of geochemical, sedimentological and erosional processes (Sepúlveda et al., 2008), (Liu et al., 2011). It is removed continuously from the atmosphere mainly by wet deposition (Ishikawa et al., 1995) and enters the ecosystem primarily as Be^{2+}, therefore measurements of ^{7}Be in precipitations provide a good way to quantify the total amount that is deposited from the atmosphere (Jha et al., 2015).

There are many factors affecting the content of ^{7}Be in rainwater, the most important being the rainfall magnitude and intensity, the rain duration, as well as the elapsed time between rain events (Juri Ayub et al., 2014).

In the case of wet precipitation, such as rain, ^{7}Be detection usually requires large sample volumes, usually collected over long sampling periods. Many different methods are employed to prepare the samples in manageable volumes, in order to detect and/or isolate ^{7}Be. Some of these methods may include evaporation of large water samples into smaller volumes (Ródenas et al., 1997). Additionally, for high volumes, samples are filtered through ion exchange resins where most of the radionuclides are being absorbed and the resin itself is then measured via γ-spectroscopy (Harvey & Matthews, 1989), (Jungck et al., 2009), (Tokuyama et al., 1993). For smaller sample volumes, ^{7}Be can be isolated with the use of ion exchange resin columns, and the elution acquired may go through co-precipitation procedures (Miyake & Ohtsuka, 1964), (Goel, Jha et al., 1956). A simpler technique applied by some researchers is to take a sub-sample of the collected volume, filter it and measure the filtrate (Juri Ayub, et al., 2009), or filter the whole sample – using multiple filters – and analyzing the filters and the filtrate via γ-spectrometry (Papandreou, et al., 2011).

These methods of sample preparation are in most cases time consuming and have some disadvantages, including adsorption of ^{7}Be to the walls of the containers used for the evaporation, or even evaporation of ^{7}Be itself. As reported in (Jungck et al., 2009) as much as 2/3 of ^{7}Be content may be lost during the evaporation process.

The Nuclear Engineering Department of the National Technical University of Athens (NED-NTUA) has established an air monitoring program since 1986, which in 2008 was extended to include ^{7}Be concentration in air and rainwater (Papandreou, et al., 2011), (Savva et al., 2018).

In this study a method for the determination of ^{7}Be in rainwater and atmospheric humidity was developed for the fast analysis of low volume rainwater and humidity samples. It is implied that this method may be applied for the analysis of snow as well.

2. Materials and methods

2.1. Development of methodology

NED-NTUA is situated at NTUA University Campus in the vicinity of Athens (37°58´41.61´´N, 23°47´5.58´´E) 195 m above sea level. Rainwater sampling is a component of the NED-NTUA monitoring program, however in order to track variations in different rain events, or even within the same rain event, as well as to perform humidity measurements, the analysis of small volume water samples is required. To this end, the development of a fast, accurate, repeatable and high efficiency procedure for sample preparation became of high importance.

At NED-NTUA rainwater is collected in plastic basins covering an area of about 0.55m^2 that are installed on the laboratory's roof. Additionally, for humidity collection, a dehumidifier of 320 W and 2.8 l storage has been installed on the roof.

The aim of this study was to develop a method to detect ^{7}Be in small volume rainwater samples as well as in air humidity, after mixing it with a cation exchange resin, namely DOWEX® 50W-X8 hydrogen form, 100-200 mesh, which has been proved to absorb ^{7}Be in rainwater (Komura, et al., 2007), (Savva et al., 2018). Additionally, it was decided to test (i) the efficiency of the use of resin, compared to other techniques which are based simply on water filtration and the subsequent analysis of the filters (Papandreou, et al., 2011), and (ii) the effect of the use of magnetic stir bars, since certain specification sheets by the resin's producer (Sigma-Aldrich, Inc.) discouraged their use in such applications (SIGMA-ALDRICH, 2011).

To this end, on the 16th of June 2018, during a heavy rainfall event, a 22 l water sample was collected and through scooping, it was divided into 6 sub-samples, 2 samples to test each one of three different variations of the method (procedures) tested as described in Fig.1.

<table>
<tr><td>Procedure #1
Use of Resin and Magnetic Stir Bar Mixing</td><td colspan="2">Procedure #2
Use of Resin and Handheld Glass Stir Rod Mixing</td><td>Procedure #3
Use of Whatman 42 Filter Paper 90mm</td></tr>
<tr><td colspan="4">Sample Weighing</td></tr>
<tr><td colspan="4">Sieving of sample through 45μm sieve to remove large particulates</td></tr>
<tr><td colspan="3">Resin humidity determination to quantify the required dry resin equivalent mass</td><td rowspan="8">Filtering of the sample through a Whatman 42 Filter Paper 90mm</td></tr>
<tr><td colspan="3">Use of 5.5g of dry resin equivalent mass (maximum water volume ≈ 3.7 l)</td></tr>
<tr><td colspan="3">Resin conditioning in 150 ml of deionized water</td></tr>
<tr><td colspan="3">Sample pH ≈ 5 adjustment with HNO_3</td></tr>
<tr><td colspan="3">Addition of conditioned resin to the sample</td></tr>
<tr><td colspan="2">Mixing of the sample-resin for 120 min using a magnetic stirrer</td><td>Mixing of the sample-resin for 120 min using a handheld glass rod</td></tr>
<tr><td colspan="3">Resting of the sample in order for the resin to precipitate</td></tr>
<tr><td colspan="3">Filtering of the whole sample through a Whatman 42 Filter Paper 90mm and resin collection</td></tr>
<tr><td colspan="3">Air drying of the collected resin at room temperature (21 ºC)</td><td>Air drying of the collected filter at room temperature (21 ºC)</td></tr>
<tr><td colspan="3">Packing of the resin in 8.72 cm^3 cylindrical geometry and analysis via γ-spectrometry</td><td>Folding of filter in a 3.2×3.2cm^2 geometry and analysis via γ-spectrometry</td></tr>
</table>

Fig. 1: Steps of the three different procedures tested for rainwater sample preparation

It should be noted that it is important to let the resin precipitate after mixing it with the sample, since this greatly improves the filtration time. Also, for Procedures #1 and #2, the filters used for the filtration, as well as the filtrate were also measured via γ-spectrometry, in order to verify that most of ^{7}Be was absorbed by the resin.

2.2. Gamma spectrometry analysis

The sample geometry used for packing and measuring the resin was cylindrical 8.72 cm^3 with 1.95 cm radius. This geometry was specifically introduced and calibrated for this study and its efficiency calibration curve for the XtRa detector which will be used for routine measurements is presented in the next paragraph. The Whatman 42 90 mm paper filters from all three Procedures were analyzed in a folded 3.2×3.2 cm^2 geometry with 1.5 mm height. The aliquots from the filtered water samples of Procedures #1 & #2 were analyzed in standard Marinelli geometry to confirm that no ^{7}Be was detectable in the filtered water, in order to verify the absorption efficiency of the resin.

For the gamma-spectrometry analysis of the samples, two of the detectors of NED-NTUA were used. A closed-end coaxial High Purity Germanium (HPGe) detector with 40.9% relative efficiency was used for the comparison of the three procedures. A closed-end coaxial Extended Range (XtRa) Germanium detector, with 104.5% relative efficiency, housed in an old steel shield and equipped with a Compton Suppression System, was used for the analysis of rain, humidity and snow samples, based on the adopted procedure (Savva et al., 2014). Gamma spectroscopic analysis was performed using the in-house developed code SPUNAL (Simopoulos, 1989).

2.3. Calibration of the gamma ray spectrometry system

For the efficiency calibration of the detector XtRa for sample geometry volume 8.72 cm^3, a numerical method based on Monte Carlo simulation was applied. For this purpose, the 2011 version of Monte Carlo code PENELOPE was used (Salvat et al., 2011). The detector has been characterized in a previous work (Savva & Anagnostakis, 2016). Using this specific detector model a combined standard uncertainty of 2.7% is introduced. The full energy peak efficiency of XtRa detector for the 8.72 cm^3 sample geometry is given in Fig.2.

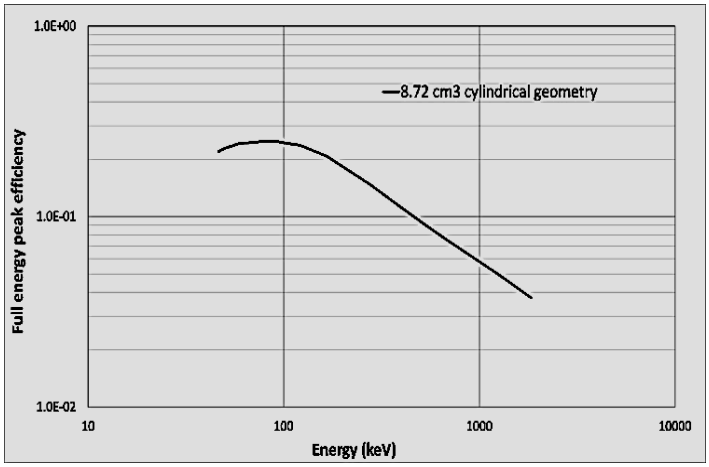

Fig. 2: Full energy peak efficiency curve of XtRa detector for 8.72 cm^3 cylindrical geometry.

For the efficiency calibration of HPGe for the 8.72 cm^3 geometry, the Marinelli geometry as well as the folded 3.2×3.2 cm^2 paper filter geometry, Monte Carlo simulation was applied as well. The detector has been previously characterized using Monte Carlo simulation techniques and the combined standard uncertainty for the efficiency introduced by the calibration procedure was estimated to 1.13% (Tsianti, 2018).

2.4. Uncertainty Analysis

In this study the results are accompanied by the combined standard uncertainty which takes into consideration type A and type B uncertainty components (JCGM/WG 1, et al., 2008). Regarding the type A uncertainty, the peak area uncertainty that is calculated by the γ-spectroscopic analysis is considered to be the principal component. As far as the type B uncertainty, the main components are the weighing of the sample and cation resin mass, which is considered to introduce a relative standard uncertainty of less than 1% (1σ), and the efficiency calibration, which adds a relative standard uncertainty of 2.7% (1σ) for detector XtRa and 1.13% for detector HPGe. Uncertainty due to the

absorption of ^{7}Be in the resin was not taken into consideration at this step.

3. Procedure screening results

All three procedures tested were compared based on their activity concentration (Bql^{-1}). It should be noted that for all measurements decay corrections to the sample collection date were applied. For each procedure, the u-score was calculated between the 2 samples, in order to check for repeatability. The u-score is calculated based on the formula:

$$u-score = \frac{|Value_1 - Value_2|}{\sqrt{unc_1{}^2 + unc_2{}^2}}$$

where, $Value_1$ and $Value_2$ are the individual measurements under comparison and unc_1 and unc_2 are their combined standard uncertainties. The measurements are considered as not statistically different when u-score is <1.96 at a 95% confidence level. The 477.6 keV peak decay corrected activity concentrations determined from each one of the three procedures (6 sub-samples) as well the u-scores are given in Table 1.

Table 1: Comparison of ^{7}Be activity concentration for the three procedure's sub-samples and their corresponding u-scores.

Procedures	Sub-Sample	Sub-sample volume (l)	Activity Concentration ± 1σ (Bq l^{-1})	u-score
1	1	3.666	0.7847 ± 0.0249	1.27
	2	3.666	0.8356 ± 0.0313	
2	3	3.696	0.7948 ± 0.0429	0.33
	4	3.676	0.7753 ± 0.0413	
3	5	3.654	0.1188 ± 0.0107	1.86
	6	3.640	0.1550 ± 0.0163	

From the results presented in Table 1 it is concluded that the use of the folded filter, without the use of resin, gives significantly lower activity concentration. This indicates that only part of ^{7}Be is retained on the filter. Additionally, both of the Procedures #1 and #2 show similar results as well as good repeatability. This indicates that the use of magnetic stir bar for the mixing of resin into the sample does not affect the final result. As a conclusion, based on the aforementioned results and the less laborious way of using the magnetic stir bar, the procedure that was finally adopted is Procedure #1. The activity concentrations of Procedures #1 and #2 were in agreement with the activity concentration range of ^{7}Be measured by previous research performed in NED-NTUA (Savva et al., 2018).

For the filtered water in the Marinelli geometry as well as the folded 3.2×3.2cm^2 filters that were acquired from the procedures #1 and #2, the activity concentrations were below minimum detectable activities (0.37 Bq l^{-1} for the Marinelli geometry and 0.02 Bq l^{-1} for the folded paper filters), which provides strong evidence that most of ^{7}Be was absorbed by the cation resin. However, further measurements need to be performed preferably using the XtRa detector, which has higher relative efficiency than HPGe, to improve minimum detectable activity for the filtrate. This will provide a realistic estimation of the maximum type B uncertainty introduced due the ^{7}Be which may not be absorbed in the resin and ends up in the filtrate.

4. Measurements based on the adopted Procedure #1

In order to further continue the study:

- One rainfall sample was collected on 15/11/2018, along with the environmental humidity before and after the rain, in order to investigate the influence of rainfall to ^{7}Be concentrations in air humidity.
- One rainfall sample of 8.2 l was collected on 18/12/2018 and split into 3 sub-samples in order to investigate the effect of acidification of the sample with HNO_3, to prevent ^{7}Be adsorption on the container walls, in case the sample is not prepared immediately after sampling and needs to be stored. The first sub-sample was prepared and measured immediately, while the other two were stored and prepared after 2 weeks, with one being acidified to pH≈3.
- One snow sample was collected on 08/01/2019.

All those samples were prepared following Procedure #1, and were measured in XtRa detector. From the results of the measurements that are presented in Table 2 it is concluded that ^{7}Be can be measured in rainwater, humidity and snow samples with acceptable accuracy. It is also concluded that ^{7}Be concentration in humidity is much lower than that in rainwater and furthermore ^{7}Be in humidity after the rainfall is below the detection limit, something which is to be expected due to the ^{7}Be wash out from the atmosphere. The ^{7}Be concentration in humidity before the rainfall and in the rainwater may be used to estimate the effect of rainout and washout in the scavenging of ^{7}Be from the atmosphere during a rainfall event. However, this needs to be further investigated with additional measurements. Additionally, the comparison between the sample prepared immediately after collection with i) the 2 weeks stored sample without acidification (u-score=3.86), and ii) the 2 weeks stored sample with HNO_3 acidification (u-score=1.86), gives a strong indication that HNO_3 should be used to acidify the water sample, in order to prevent adsorption to the container walls if it is to be stored before sample preparation. However, it should be noted that the relatively high u-score=1.86, may partly be attributed to the different pH value (3 instead of 5 as proposed in Fig.1). In this case also, further investigation is needed. Surprisingly, the ^{7}Be activity in snow is very low, compared to that in rainfall, contrary to what is expected in the literature (Gaffney et al., 1995), (Ishikawa et al., 1995). This could be due to scavenging during previous rainfall or snowfall events in the area.

5. Conclusions

The sampling preparation method for the analysis of rain, humidity and snow samples that was adopted during this work was as described in Procedure #1, which employs the absorption of ^{7}Be in a cation resin by mixing the resin with the water sample using a magnetic stirrer. The use of a glass rod for the mixing the sample, though labor consuming, did not show any significant effect in the final results. The method of filtering the sample and the subsequent filter analysis showed a significantly lower retention of ^{7}Be. Finally, sample acidification is strongly recommended in case there is a need for water sample to be stored before being mixed with resin; however a more detailed investigation is needed to optimize this part of the procedure.

Based on the above conclusions and the adopted sample preparation procedure, fast analysis of small volumes of water samples (rain, humidity, snow) became possible, and will be included in the NED-NTUA environmental monitoring program for studying of ^{7}Be concentration in precipitations, with good accuracy and low detection limits.

Table 2: Further measurements of samples based on the adopted sample preparation procedure.

Sample	Sample Volume (l)	Sampling Date	Activity Concentration ± 1σ (Bq l^{-1})	MDA (Bq l^{-1})
humidity before rainfall	2.750	15/11/2018	0.07 ± 0.02	0.02
rainfall	3.506	15/11/2018	0.80 ± 0.04	0.02
humidity after rainfall	2.818	19/11/2018	not detected	0.02
rain (immediate sample preparation)	2.738	18/12/2018	1.92 ± 0.09	0.03
rain (2 week stored before preparation)	2.732	18/12/2018	1.48 ± 0.07	0.02
rain (2 week stored before preparation + HNO_3)	2.724	18/12/2018	2.17 ± 0.10	0.02
snow	3.521	08/01/2019	0.14 ± 0.02	0.02

References

Cannizzaro, F., Greco, G., Raneli, M., Spitale, M. C., & Tomarchio, E., 2004. Concentration measurements of 7Be at ground level air at Palermo, Italy-comparison with solar activity over a period of 21 years. Journal of Environmental Radioactivity, 72, 259-271.

Gaffney, J. S., Orlandini, K. A., & Marley, N. A., 1995. Measurements of ^{7}Be and ^{210}Pb in Rain, Snow, and Hail. Environmental Science and Technology, 29(1), 8-9.

Goel, P. S., Jha, S., Lal, D., Radhakrishna, P., & Rama., 1956. Cosmic Ray Produced Beryllium Isotopes in Rain Water. Nuclear Physics, 1(3), 196-201.

Harvey, M. J., & Matthews, K. M., 1989. 7Be Deposition in a High-Rainfall Area of New Zealand. Journal of Atmospheric Chemistry, 8, 299-306.

Ishikawa, Y., Murakami, H., Sekine, T., & Yoshihara, K., 1995. Precipitation Scavenging Studies of Radionuclides in Air Using Cosmogenic ^{7}Be. Journal of Environmental Radioactivity, 26, 19-36.

Ishikawa, Y., Murakami, H., Sekine, T., & Yoshihara, K., 1995. Precipitation Scavenging Studies of Radionuclides in Air Using Cosmogenic ^{7}Be. Journal of Environmental Radioactivity, 26, 19-36.

JCGM/WG 1, BIPM, IEC, IFCC, ILAC, ISO, OIML., 2008. JCGM 100:2008 (GUM 1995 with minor corrections): Evaluation of measurement data-Guide to the expression of uncertainty in measurement (1st ed.).

Jha, A., Schkade, U., & Kirchner, G., 2015. Estimating short-term soil erosion rates after single and multiple rainfall events by modelling the vertical distribution of cosmogenic ^{7}Be in soils. Geoderma, 243-244, 149-156.

Jungck, M. H., Andrey, J.-L., & Froidevaux, P., 2009. Determination of radionuclide levels in rainwater using ion exchange resin and γ-spectrometry. Journal of Environmental Radioactivity, 100, 361-365.

Juri Ayub, J., Di Gregorio, D. E., Velasco, H., Huck, H., Rizzotto, M., & Lohaiza, F., 2009. Short-term seasonal variability in ^{7}Be wet deposition in a semiarid ecosystem of central Argentina. Journal of Environmental Radioactivity, 100, 977-981.

Juri Ayub, J., Velasco, R. H., Rizzotto, M., & Anjos, R. M., 2014. Beryllium-7 content in rain: Evidences for a semiarid environment. In P. Dyer (Ed.), Beryllium-Physicochemical Properties, Applications and Safety Concerns (pp. 83-103). New York: Novinka.

Komura, K., Kuwahara, Y., Abe, T., Tanaka, K., Murata, Y., & Inoue, M., 2007. Measurements of short-lived cosmic-ray-produced radionuclides in rainwater. Journal of Environmental Radioactivity, 96, 103-109.

Lal, D., Malhotra, P. K., & Peters, B., 1958. On the production of radioisotopes in the atmosphere by cosmic radiation and their application to meteorology. Journal of Atmospheric and Terrestrial Physics, 12, 306-328.

Liu, G., Yang, M., Warrington, D. N., Liu, P., & Tian, J., 2011. Using beryllium-7 to monitor the relative proportions of interrill and rill erosion from loessal soil slopes in a single rainfall event. Earth Surface Processes and Landforms, 36, 439-448.

Miyake, Y., & Ohtsuka, Y., 1964. Beryllium-7 in Rain Water. Papers in Meteorology and Geophysics, 15(1), 89-92.

Papandreou, S. M., Savva, M. I., Karfopoulos, K. L., Karangelos, D. J., Anagnostakis, M. J., & Simopoulos, S. E., 2011. Monitoring of ^{7}Be Atmospheric Activity Concentration Using Short Term Measurements. Nuclear technology & Radiation Protection, 26(2), 101-109.

Ródenas, C., Gómez, J., Quindós, L. S., Fernández, P. L., & Soto, J., 1997. ^{7}Be Concentrations in Air, Rain Water and Soil in Cantabria (Spain). Applied Radiation and Isotopes, 48(4), 545-548.

Salvat, F., Fernández-Varea, J. M., & Sempau, J., 2011. PENELOPE-2011, A Code System for Monte Carlo Simulation of Electron and Photon Transport. Barcelona, Spain: OECD Nuclear Energy Agency.

Savva, M. I., Karangelos, D. J., & Anagnostakis, M. J., 2018. Determination of ^{7}Be and ^{22}Na activity in air and rainwater samples by gamma-ray spectrometry. Applied Radiation and Isotopes, 134, 466-469.

Savva, M. I., Karfopoulos, K. L., Karangelos, D. J., Anagnostakis, M. J., & Simopoulos, S. E., 2014. Installation and performance testing of an XtRa-NaI(Tl) Compton Suppression System at the NED-NTUA. Applied Radiation and Isotopes, 87, 361-364.

Savva, M., & Anagnostakis, M., 2016. Experimentally validated Monte Carlo simulation of an XtRa-NaI(Tl) Compton Suppression System response. Applied Radiation and Isotopes, 109, 555-557.

Sepúlveda, A., Schuller, P., Walling, D. E., & Castillo, A., 2008. Use of ^{7}Be to document soil erosion associated with a short period of extreme rainfall. Journal of Environmental Radioactivity, 99, 35-49.

SIGMA-ALDRICH., 2011. Retrieved 06/07/2018 from http://sigma-aldrich.custhelp.com/app/answers/detail/a_id/3082/p/19,1001/session/L3RpbWUvMTUxOTk5ODMyMy9zaWQvTHFQdG1DR24%3D

Simopoulos, S. E., 1989. Soil Sampling and ^{137}Cs Analysis of the Chernobyl Fallout in Greece. Applied Radiation and Isotopes, 40(7), 607-613.

Tokuyama, H., Oonishi, M., & Matsuura, H., 1993. Environmental Background Level of Cosmic Ray Produced ^{22}Na. Journal of Environmental Radioactivity, 21, 213-218.

Tsianti, M., 2018. Measurements of low level natural and artificially induced radioactivity in environmental samples. Athens, Greece: NED-NTUA Diploma Thesis (in Greek).

Preparation of area ^{90}Sr reference sources using Nafion ion exchange membrane

Yanliang Chen[*,a,b], Chao Zhao[a], Linfeng He[a], Fangdong Tang[a]

[a]*Shanghai Institute of Measurement and Testing Technology*

[b]*Shanghai Jiao Tong University*

Abstract

A method was set up to prepare reference sources for calibration of surface contamination monitors using Nafion HP Membrane. By investigating adsorption mechanism parameters, it has been proved the ^{90}Sr could be adsorbed on the membrane effectively. The surface emission rate and the activity were measured. In addition, the uniformity of the sources was evaluated and the standard deviation of the surface emission rates from each individual portion of the whole source was smaller than 5%.

Keywords: radioactivity reference source, ion exchange membrane

[*]Corresponding author, e-mail address: chenyanliang@simt.com.cn

1. Introduction

Radioactive sources are used in many fields, such as geology, industry, agriculture and so on. However, in this work, we are only concerned about the production method of the sources used for radionuclide metrology, especially the reference sources for the calibration of surface contamination monitors.

Surface radioactive contamination threatens the safety of humans and the environment. To control surface radioactive contamination, suitable surface contamination monitors are widely used in all kinds of nuclear facilities. These devices require calibration traceable to relevant national standards and large-area reference sources are needed [1].

As introduced in our previous publication, most of the quantitative radioactive reference sources are currently manufactured with electro-deposition procedures, which pose some unavoidable problems. Ion exchange technology has been considered to be a solution to manufacturing radioactive sources [2]. Thus, we have set up a more convenient method to prepare homogeneous and chemically stable reference sources and have prepared ^{241}Am reference sources successfully. In this work, we have applied this method in preparing β reference sources with ^{90}Sr nuclide, attaching the membrane on the backing material before the adsorption to avoid the membrane from wrinkling. In this work, Nafion HP membrane (DuPont Nafion PFSA membrane) was selected to prepare the reference source because of its high chemical and radiation stability [3, 4]. The parameters of the source, such as the activity, surface emission rate, self-adsorption and uniformity, will be determined by the methods advised by ISO 8769 to evaluate the quality of the source.

2. Experimental

2.1 Reagents and materials

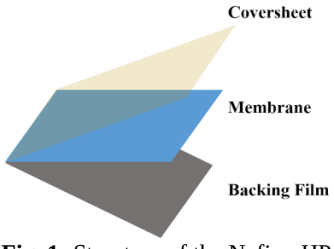

Fig. 1: Structure of the Nafion HP membrane

DuPont Nafion HP membrane is an extended-lifetime reinforced membrane based on chemically stabilized perfluorosulfonic acid/PTFE copolymer in the acid (H^+) form. The membrane is positioned between a backing film and a coversheet, as shown in Fig. 1.

The parameters of the Nafion HP membrane and the rectangular aluminium plate adopted as the backing material have been introduced and detailed in previous work [2].

The polydimethylsiloxane (PDMS) used to form the adsorption tank was produced by Dow Corning Co. Ltd and the UV curing adhesive used to fix the membrane to the backing material was supplied by the Loctite Co. Ltd. In the adsorption experiment, the solution containing strontium was prepared by diluting from a standard solution or dissolving the strontium nitrate. The standard solution and strontium nitrate were purchased from Aladdin Chemistry Co. Ltd. The concentration of the standard solution was 1000 ppm, which was then diluted with deionized water to the various concentrations needed for the adsorption batch experiments. Deionized water was produced by a laboratory water purification system (DW-200) with a resistance of 18 MΩ.

2.2 Preparation of the source

The procedures to prepare a reference source mainly consisted of two steps including fixing the membrane on the backing material and the adsorption of radioactive nuclides. The device for adsorbing radioactive nuclides was set up according to the previous work [2]. A diagrammatic sketch of the whole device is shown in Fig. 2.

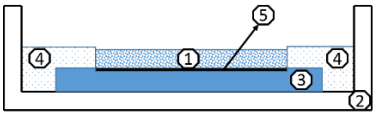

Fig. 2: Diagrammatic sketch of device to prepare the reference source (1: Solutions; 2: Quartz glass reaction tank; 3: Aluminium – backing material; 4: PDMS; 5: Ion exchange membrane)

Unlike the traditional operation of ion exchange resins or membranes, the solution and the ion exchange membrane were relatively motionless. Therefore, the adsorption model for this situation was set up to ensure an effective adsorption of radioactive nuclides. Batch experiments were conducted to investigate the

adsorption behavior, especially the effect of pH, adsorption kinetics and initial concentration.

The adsorption of strontium in solutions of different pH was conducted to find the best condition at which the adsorption reached the maximum capacity. During the pH experiments, to ensure the adsorption reached equilibrium, the contacting time was set long enough, i.e. up to 3 hours.

A solution containing 200 ppm of strontium with a volume of 75 mL and the pH of 7 was added to the reaction tank. After times ranging from 5 minutes to up to 3 hours, the concentration of strontium in the solution was determined by ICP-OES (Varian700, produced by Agilent Technologies Inc.). Then the absorbed amount of strontium along with the adsorption time could be calculated and the adsorption kinetics could be summarized.

In order to investigate the adsorption capacity, adsorption equilibrium isotherms (as shown in Figure 4) have been obtained through the batch experiments for a wide range of initial concentrations of strontium ions. Initial concentration of strontium ions ranged from 0.1 mM to as great as 20 mM, which could ensure the adsorption of strontium onto the membrane attained saturation. The pH of the solutions was 7 and the contact time was 1 hour. The concentration of strontium in the solution before and after the adsorption were determined by ICP-OES.

In order to improve the usage rate of ^{90}Sr, the ratio of adsorbed ^{90}Sr is expected to be as high as possible. However, if all the ^{90}Sr is adsorbed, it is difficult to ensure the uniformity of the sources. A membrane with a size of 100 mm×150 mm has an ion exchange capacity of about 5.4 mmol, which is several thousand times larger than the amount of ^{90}Sr needed to prepare a reference source with a surface emission rate of about 30000 cpm. This is averse to achieving uniform sources. To solve this problem, stable strontium was added to the solutions to control the adsorption of ^{90}Sr due to the same chemical property. According to the results from the adsorption equilibrium isotherm experiments, the amount of adsorbed strontium could be controlled and the ratio of adsorbed ^{90}Sr made to be the same as the total strontium.

According to the adsorption model, under optimal conditions (the pH was 7, the contact time was 1 hour and the initial concentration of strontium was 0.5 mM), the solution containing ^{90}Sr with an activity of about 1850.7 Bq was added to the reaction tank. After a suitable adsorption time, the solution was removed. Finally, the backing material with the membrane which had adsorbed radioactive nuclides was taken out of the quartz glass tank and cleaned of all the polymerized PDMS.

After all these procedures, a new kind of reference source was prepared.

2.3 Characterization of the source

To evaluate the quality of a reference source, the international standard ISO 8769 specifies a series of requirements.

Activity could be calculated according to the concentration of nuclides in the solution before and after the adsorption. To check the adsorption affinity of PDMS for strontium, a batch experiment was conducted. Solution containing strontium was added to the reaction tank without Nafion HP membrane and the concentration of strontium was checked after a period of time. The activity of strontium in solution was determined by a liquid scintillation counter (AccuFLEX LSC LB7, produced by Hitachi Aloka Medical Ltd.).

As suggested in ISO 8769, surface emission rate should be determined by absolute methods at a national or international metrology institute. In this work, the method of 2π proportional counting was conducted using a large-area multi-wired windowless gas-flow proportional counter, which was developed in-house and calibrated to China's national standard. The detector was operated under continuous flow of a mixture of argon (90 %) and methane (10 %).

Uniformity indicates the reproducibility of the emission rate over the surface, expressed as the relative experimental standard deviation derived from the emission rates from each individual portion of the whole source. In this work, uniformity was checked according to the method described previously [2].

The efficiency of the sources reflects the backscattering and self-absorption. It could be defined as the quotient of the surface emission rate and the activity [5]. As reported, if the efficiency exceeds 0.454, the source can be calibrated as a Class 1 reference source in compliance with ISO 8769.

Finally, to evaluate the stability of the source, the wipe-off factor was tested with a swipe. The surface emission rate of the source before and after the wipe-off test was measured and compared.

`

3. Results and discussion

3.1 Adsorption model

In the adsorption experiments, the Nafion HP membrane showed strong adsorption affinity toward strontium in the solutions with a pH ranging from 1 to 8 and the adsorption was a little stronger in pH of 6 to 7 than at other values. Thus, the experiment for the kinetics was conducted under this pH range.

Fig. 3 diagrams the amount of adsorbed strontium on the membrane over time. The adsorbed strontium increases quickly in the initial period of time; adsorption reaches equilibrium after about 1 hour.

A pseudo-first order kinetics model has been adopted to evaluate the mechanism of the adsorption kinetics. It is expressed as follows:

$$q_t = q_e(1-e^{-k_1 t}) \quad (1)$$

where q_t (mg/g) denotes the adsorption quantity at any time before equilibrium; q_e (mg/g) denotes the equilibrium adsorption quantity; and k_1 is constant related to the rate of adsorption.

These adsorption results fit the pseudo-first order kinetics equation well.

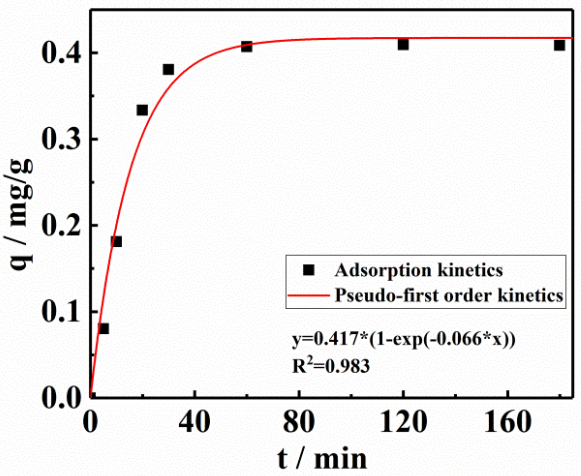

Fig. 3: Adsorption kinetics of strontium

The adsorption equilibrium isotherm is shown in Fig. 4. A theoretical equilibrium isotherm model, the Langmuir equation, has been employed to study the adsorption mechanism and calculate the maximum capacity. The Langmuir equation assumes that the adsorption process is a monolayer adsorption on a homogeneous surface. It is described as:

$$q = \frac{q_e K_L c}{1 + K_L} \quad (2)$$

where c (mmol/L) is the equilibrium concentration of strontium in aqueous phase; q(mmol/g) and q_e (mmol/g) are the adsorption quantity at the equilibrium and the saturation, respectively. K_L (L/mmol) is the Langmuir constant which relates to the energy of adsorption.

The correlation coefficients indicate that the adsorption of strontium obeys the Langmuir model and furthermore the adsorption presents as a monolayer adsorption controlled by homogeneous active sites of the membrane.

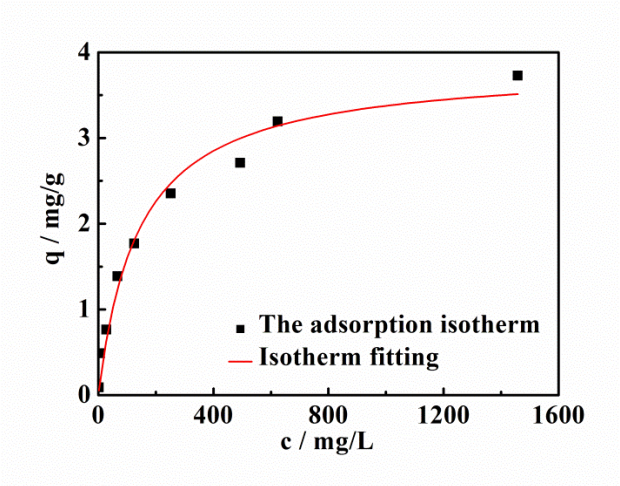

Fig. 4: Adsorption equilibrium isotherm of strontium

With an initial concentration of strontium of 0.5 mM, about 90 % strontium was adsorbed by the membrane. Therefore, this was an acceptable adsorption yield of strontium which also allowed control of the uniformity.

According to the above results, the optimal conditions to prepare the reference sources could be determined. The pH was set as 7. The adsorption time was set as 1 hour. The initial concentration of total strontium, including stable strontium and ^{90}Sr, was set as 0.5 mM.

3.2 Characterization of the source

The activity of the solutions containing ^{90}Sr before and after adsorption is shown in Table 1. Futhermore, in the absence of Nafion HP membrane, PDMS showed no adsorption of strontium because the concentration of strontium in the solution remained constant. Thus the activity of ^{90}Sr adsorbed on the membrane and the adsorption yield could be calculated and the results are listed in Table 1.

As measured by the large-area multi-wired windowless gas-flow proportional counter, the surface emission rates are shown in Table 1. According to the emission rate of each portion, the uniformity was calculated as about 4.25 % which is better than 5 % and can satisfy the requirements of a Class 1 reference source in compliance with ISO 8769. It shows that the ^{90}Sr distributes uniformly on the membrane.

It can be calculated that the efficiency of the source was about 46.5 %, better than 45.4 %, which is the requirement of a Class 1 reference source in ISO 8769.

After multiple (10 to 15) times wiping with a swipe, the surface emission rate of the source kept constant, proving that the stability of the source was satisfactory. As a comparison, a reference source manufactured by electro-deposition and purchased from the China National Institute of Metrology was used freely. Without any intentional wiping, the surface emission rate of that source decreased by about 10 % every year after daily use, clearly indicating that the source should not be wiped or soaked in water.

Table 1: Characteristics of the ^{90}Sr reference sources

Number	^{90}Sr in the solutions (Bq)		^{90}Sr adsorbed (Bq)	Adsorption yield (%)	Surface emission rate (min^{-1})	Efficiency (%)
	Before adsorption	After adsorption				
^{90}Sr-001	1850.7	259.1	1591.6	86.0	44850.0	47.0
^{90}Sr-002	1871.3	260.2	1611.1	86.1	44875.6	46.4
^{90}Sr-003	1831.5	250.2	1581.3	86.3	44795.1	47.2
^{90}Sr-004	1891.3	267.1	1624.2	85.9	45001.3	46.2
^{90}Sr-005	1809.5	231.7	1577.8	87.2	44125.3	46.6

4. Conclusions

A procedure to prepare radionuclide reference sources using DuPont Nafion HP ion exchange membrane was set up. The adsorption mechanism was clarified and the best conditions for the adsorption of strontium were found. With this method, a reference source with an accurate surface emission rate and satisfactory uniformity has been manufactured successfully; it is convenient to prepare similar reference sources with different active region areas by changing only the size of the aluminium backing plate and the membrane. In addition, by changing the radioactive nuclides and determining the adsorption properties of these nuclides, sources emitting different particles can be prepared. All these results suggest that this method to prepare reference sources using ion exchange membrane is effective and feasible. The sources show better stability than traditional electro-deposition products. The main characteristics of the prepared sources all meet the requirements of a Class 1 reference source according to ISO 8769.

In further investigations, we will focus on manufacturing novel membranes which are more suitable for preparing reference sources. New membranes, especially thin ones with smaller cross-linkage and with functional groups distributing uniformly only on the surface, are needed. A membrane with anion exchange ability will be developed to prepare sources of nuclides like ^{36}Cl.

Acknowledgements

Part of this work is financially supported by the Talent program (Yangfan program) of Shanghai Science and Technology Commission of Shanghai Municipality (19YF1441600) and the National Natural Science Foundation of China (No. 11605113).

References

1. Unterweger MP, De Felice P (2015) Uncertainties in surface emission rate measurements. Metrologia 52 (3):S165-S171. doi:10.1088/0026-1394/52/3/s165

2. Yanliang C, Chao Z, Lingfeng H, Fangdong T (2018) Preparation of reference sources for calibration of surface contamination monitors using Nafion ion exchange membrane. Journal of Radioanalytical and Nuclear Chemistry 318:2307–2311.https://doi.org/10.1007/s10967-018-6259-5
3. Balko EN, Chaklos JT (1981) Effects of ionizing radiation on perfluorosulfonic acid ion-exchange polymer. J Appl Polym Sci 26 (5):1519-1531
4. Iwai Y, Hiroki A, Tamada M, Isobe K, Yamanishi T (2010) Radiation deterioration of ion-exchange Nafion N117CS membranes. Radiat Phys Chem 79 (1):46-51. doi:10.1016/j.radphyschem.2009.08.001
5. Janssen H, Klein R (1994) Characterization of large-area reference sources for the calibration of alpha-contamination monitors. Nuclear Instruments and Methods in Physics Research Section A: Accelerators, Spectrometers, Detectors and Associated Equipment 339 (1–2):318-321

Implications of the sampling method on the determination of ^{222}Rn in groundwater

J. Vaquero, J.C. Lozano*, M.C. Pedrosa

Laboratorio de Radiaciones Ionizantes-Datación. Universidad de Salamanca.Spain.

Abstract

According to the Directive 2013/51/Euratom, Spanish regulations establish a limit value for the presence of ^{222}Rn in drinking water of 1000 Bq·L^{-1}, although a parametric value has discretionally been set at 500 Bq·L^{-1}. This radionuclide presents high volatility and, therefore, sampling is crucial to report correctly its activity concentration in water samples. The constructive characteristics of the access point to the aquifer, as well as the used sampling method, are both very important aspects that are addressed in this work.

Keywords: ^{222}Rn; LSC; Sampling methods; Water samples

* Corresponding author, email address: jll390@usal.es

1. Introduction

Unlike the rest of the radionuclides of the ^{238}U series, the gaseous character of ^{222}Rn implies high diffusivity. The water adjacent to the rocky substrate dissolves radon, and then the gas passes to the atmosphere once the water has surfaced.

The consumption of water containing high concentrations of ^{222}Rn is a risk factor for health. The recommendations offered by the International Commission on Radiological Protection (ICRP) have been adopted by the European Commission (Council Directive 2013/51 / Euratom of the Council on October 22, 2013), establishing a parametric value of 100 Bq·L^{-1} for radon in drinking water, equivalent to 0.1 mSv/year of Dose Index (DI), and a limit value of 1000 Bq·L^{-1}. In Spain, the parametric value has been set at 500 Bq·L^{-1}.

The representative measure of radon present in the water is difficult because the gas escapes easily into the atmosphere while the sample is being handled (Jobbagy et al., 2019). By moving or pouring water from one container to another, the dissolved radon in the water will be released. On the other hand, the increase in temperature of the sample will cause radon losses due to its transfer from the water into the air (WHO, 2015). In addition, the time elapsed from the sampling to the measurement will also condition the accuracy of the determination of the gas activity concentration in the sample. Due to its relevance, it is important to develop efficient methods of collecting samples and transporting them, which is the focus of this work.

2. Materials and methods

2.1. Sampling sites

The province of Salamanca covers areas where there are the largest uranium reserves in Spain (Both et al., 1994; Martínez-Alegría et al., 2014) with a high presence of radon in the air (Quindós Poncela et al., 2004).

For the study, three surface aquifers located northwest of the province of Salamanca were selected. The Nuclear Safety Council cataloged this area as a high radon potential exposure zone (CSN, 2000).

From the first aquifer (AQ1), located on the richest uranium area, 84 water samples were collected, divided between four sampling points with different construction characteristics, all of them sited in the village Vilavieja de Yeltes (UTM coordinates: 715013E, 4528843N; Zone 29). From the second (AQ2) and the third aquifer (AQ3), located on granodioritic substrate and shales, 20 and 16 samples were collected, respectively. The sampling points corresponding to AQ2 were sited in the village Fuenteliante (UTM coordinates: 705092E, 4523326N; Zone 30), and those corresponding to AQ3 were located in the village Bogajo (UTM coordinates: 709206E, 4531400N; Zone 30).

The samplings were programmed for the summer months of 2018 and winter of 2018-2019 and distributed in 7 campaigns.

2.2. Description of sampling points

The sampling points were chosen to cover as many situations as possible that health workers often face during a routine sampling campaign. These points consisted of:

- Groundwater tank (TANK).- At this type of access point, samples at a known depth are obtained; however, the stratum of water in the aquifer is unknown. Here, the water is not accessible by hand and some collection device is necessary to reach the water body. The population frequently uses this point and so it is of interest for health workers.
- Water faucet (FAUC).- Here, the use of special collection devices is not necessary because water is available on the surface. Being the upwelling channel most commonly used by the population, this is, together with the groundwater tank, the point of most interest for health workers.
- Borehole (BORE).- The collection is conditioned by the already installed water access device, which was a manual piston pump in our study. As in the groundwater tank, the stratum of water in the aquifer is unknown. The advantage is that it does not require additional capture systems to reach water, although the depth of sampling is not selectable.
- Well (WELL).- It allows for obtaining simple selective samples in-depth. It is necessary to use some external collection system to obtain the water samples as in the case of the groundwater tank.

2.3. Sampling methods

The way to handle the sample, its preservation and its transport, cause alterations that may affect the radon content of water. The tested methods are classified as "*ex situ"* if the sample once collected should be transported to the laboratory for the preparation of the vial for liquid scintillation counting, or as "*in situ*" if the collection of the sample and the preparation of the vial for counting is done at the same sampling point. The different methods used were the following:

- "*Ex situ*" method of the bottle (BOTT): Price & Alvarez (1999) described this method. The recipients were completely submerged

and closed under the water surface. Once the recipient was filled, ensuring the absence of air bubbles, the sample was transported to the laboratory for preparation of the counting vial. High-density polyethylene bottles (PE) of different volume were used for water sampling. For comparison, glass bottles were also used in certain sample campaigns.

- Syringe method of the US EPA (SEPA): It is an "*in situ*" procedure, which is derived from the method proposed by Burtkhan et al. (1991). The way of accessing the water defines two variants: the first, the syringe is directly submerged in the water body by using an extender pole if necessary (SEPA-DIR), and the second (EPA recommended), the syringe collects water from a bucket (SEPA-IND). In our study, the syringe was used without the conventional stainless steel needle to avoid cavitation effects. The 10 mL sample was carefully introduced into the vial pouring the sample slowly onto the cocktail.
- "*In situ*" method using a submersible pump (PUMP): In order to fill the vial, water was collected by means of a 9 V pump, using a clear PVC hose of inner diameter 8 mm (wall thickness 1 mm) and up to 4 m in length to reach the water body. It was also used by submerging the pump into a bucket.
- Method of the depressurized syringe (DEPR): This tentative method was probed to enhance the sampling of water in points with difficult access. A polypropylene plug in the nozzle ensured the tightness of the syringe, which was previously depressurized keeping its plunger fixed for the intake of a volume of 10 mL. Attached to a telescopic pole, the syringe was driven to the desired depth in the aquifer. Once submerged, the plug was removed by pulling a thread.

Both in TANK and WELL points, the depth of the table water conditioned the access to the water body. In the aquifers studied, despite being affected by seasonal conditions, this depth never exceeded 3.5 m. The collection of water in these points was carried out by fixing the sampling devices with flanges to a multilayer graduated tube of inner diameter 1.6 cm (wall thickness 0.2 cm) and 4 m in length used as a telescopic pole or using the pump with its clear PVC hose. All the samples were taken 3 cm below the water surface.

On the other hand, in the points with already installed supply devices (FAUC and BORE), a 5 L bucket was placed at the device outlet keeping submerged the faucet while the bucket was filling. The flow was permanently maintained allowing the water overflow for 5 minutes, and then the samples were taken by the methods already mentioned.

Once collected, either the samples prepared "*in situ*" or the samples collected by the so-called "*ex situ*" methods were immediately transported to the laboratory in a portable icebox with melted ice. The time between sampling and measuring was never more than 5 hours, nor less than 3.5 hours.

2.4. Measurement and counting conditions

Using "*ex situ*" methods, once at the laboratory, 10 mL of water from each sample were pipetted with the syringe and were introduced in standard 22 mL Teflon-coated PE vials of low diffusion already containing 10 mL of the scintillation cocktail. For "*in situ*" methods, the same vials already prepared with the same ratio water/cocktail arrived at the laboratory ready for counting. The cocktail used was Proscint Rn/AB, an oil-based cocktail specific for radon and immiscible with the aqueous phase.

Once the vials were prepared, a Quantulus 1220™ liquid scintillation counter was used for counting. Optimized counting conditions corresponded to a PSA discrimination level of 55 and the High option of the Coincidence Bias function was always activated.

The background rate, evaluated from blank samples and measured for a one week period, presented an average value of 0.349(6) cpm selecting the complete window of the alpha spectrum (1-1024 channels), which was reduced to 0.040(2) cpm using the optimal analysis windows (690-890 channels). This window, including the alpha emissions of ^{222}Rn, ^{218}Po, and ^{214}Po, was selected for all the alpha spectra analyzed. It covered the slight shifts observed for the peak positions associated with the small variations of the quenching parameter SQP(E) observed and expected for a two-phase sample/cocktail configuration.

Results with analysis windows that included ^{222}Rn, ^{218}Po, and ^{214}Po emissions, with an extinction-level similar to that observed in environmental samples (average SQP(E) = 854(12)), gave an average integral efficiency ε = 243(3) %. The minimum detectable activity (MDA) obtained was 0.093 Bq·L^{-1} for a counting time of 60 min, well below the limit value set by the Spanish legislation of 10 Bq·L^{-1}. MDA was evaluated by applying the implementation of ISO 11929:2010 proposed by De Felice et al., 2017.

2.5. Activity calculus

The initial activity of radon present in the sample, C°_{Rn} (cpm, at the time of the vial preparation, t_0), was obtained by means of least-squares fitting of the following equation to the counting results obtained at different times after the vial preparation:

$$C_{Rn}(t) = C^{\circ}_{Ra} + (C^{\circ}_{Ra} - C^{\circ}_{Rn}) \cdot e^{-\lambda_{Rn}\cdot(t_i - t_0)} \cdot \frac{(e^{-\lambda_{Rn}\cdot T} - 1)}{T\lambda_{Rn}} \quad \text{Eq. 1}$$

where $C_{Rn}(t)$ represents the net count rates of ^{222}Rn (in cpm) at different times t; λ_{Rn} is the decay constant of ^{222}Rn (1.26·10^{-4} min^{-1}); C°_{Ra} is the initial activity of ^{226}Ra in the vial (in cpm); t_i represents the beginning of the counting interval; and T is the counting time (min).

The study of the activity evolution with time was carried out using vials prepared with known activities of ^{226}Ra. For this, 10 cycles of 60 min measurements spread over a period of 30 days were carried out for each sample to reach the secular equilibrium between radon and its progenitor. From these measurements, leaving λ_{Rn} as a fit parameter in Eq.1 ($\lambda_{Rn\text{-}effective}$), the tightness of the vial was evaluated, obtaining an average value $\lambda_{Rn\text{-}effective}$ = 1.48(3)·10^{-4} min^{-1}. The value found was greater than the theoretical constant λ_{Rn} = 1.26·10^{-4} min^{-1}, pointing out that small losses were produced by diffusion in the counting vials (low diffusion PE-Teflon-coated vials).

The activity concentration of ^{222}Rn of the samples at the time of the vial preparation is calculated by the following expression:

$$A^0_{Rn}(Bq \cdot L^{-1}) = \frac{C^0_{Rn}(cpm)}{\varepsilon \cdot 60 \cdot V} \qquad \text{Eq. 2}$$

where C^0_{Rn} (in cpm) is the net radon count rate at t_0, ε is the detection efficiency for the selected window (in cpm/dpm), V is the volume of the sample (in L), and factor 60 transforms the dpm into Bq.

3. Results and discussion

3.1. The validity of the DEPR method

This tentative method was probed during the first and the second sampling campaigns, on the collecting points of AQ1 with the water not available by hand, i.e. TANK and WELL points. Compared to the other applied methods in these points (PUMP and BOTT methods), the DEPR method provided the lowest activity concentrations of ^{222}Rn. These results can be seen in Fig.1.

The other syringe-based method, SEPA-DIR, was also used for sampling water of AQ1 through the points FAUC and BORE. Contrary to the DEPR method, the SEPA-DIR method gave the highest activity concentrations compared with those obtained by using the PUMP and the BOTT methods (shown in Fig.1).

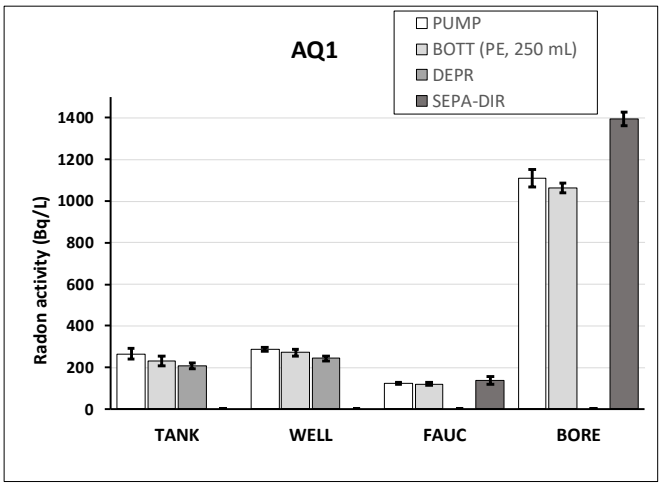

Fig. 1: Comparison of sampling methods for the four access points of the aquifer AQ1.

The efficacy of the DEPR method regarding the SEPA method was tested at the laboratory. For this test, a suspension of $^{226}Ra(Ba)SO_4$ particles of known activity was used to generate ^{222}Rn. Due to ^{222}Rn exhalation from these particles does not reach 100% of its production by ^{226}Ra decay, the objective was not to determine the accuracy of both methods but to compare them in relative terms.

The test confirmed losses of ^{222}Rn for the DEPR method regarding the SEPA method, probably due to cavitation effects during the rapid filling of the syringe when the vacuum acts. The DEPR method became up to 40% less efficient than SEPA method (results not shown). The DEPR method was rejected for the rest of the sampling campaigns, hoping for improvements in its design to ensure the representativeness of the samples.

3.2. Constructive characteristics of the access points

3.2.1. Aquifer AQ1

In the first two sampling campaigns, a total of 32 samples distributed among the four sampling points of the same aquifer (AQ1) were collected. Fig.1 shows the results of ^{222}Rn activity concentrations for each sampling point taking into account the sampling method used.

The lowest activity values were found in the samples taken at the FAUC point, with activity concentrations between 9 and 10 times lower than those obtained in the water samples collected at the BORE point and half of the activities found at the TANK and WELL points.

For the two points with constructive characteristics more similar to each other, that is, for TANK and WELL points, more similar activity levels were recorded (Fig.1). However, there were significant differences between both points taking into account separately each sampling method (T-test for BOTT method: 95% confidence, p-value=0.014<0.05; T-test for PUMP method: 95% confidence, p-value=0.034<0.05; T-test for DEPR method: 95% confidence; p-value=0.004<0.05). Therefore, the differences of the average values can be attributable to the constructive characteristics of both points.

Samples collected at the point BORE showed activity concentrations greater than 1000 $Bq \cdot L^{-1}$ using all the sampling methods (Fig.1). The maximum value obtained in this supply, applying the SEPA-DIR method, was 1418(32) $Bq \cdot L^{-1}$.

The different configurations of the collection points condition the activity concentration of ^{222}Rn in water. The BORE point represents the most direct access to the water in the aquifer, constructed as a deep drilling with a narrow tube. In a general definition, both TANK and WELL points represent dynamic reservoirs with much larger dimensions than BORE, which enhance the water-to-air transfer of ^{222}Rn. In AQ1, the FAUC point represents the largest losses of ^{222}Rn probably due to aeration and turbulence effects during the water conduction from the aquifer to the surface.

3.2.2. Aquifers AQ2 and AQ3

Again, the lowest activity concentrations of ^{222}Rn were found for the FAUC points, although depending on the aquifer the relative differences with regard to the TANK points were more or less severe. While for the aquifer AQ1 the activity concentration ratio TANK/FAUC was almost two-fold (Fig.1), this ratio for AQ2 was practically the unity (T-test: 95% confidence; p-value=0.084>0.05, using the BOTT method) and around 1.6 for the aquifer AQ3. These last ratios can be obtained from the results in Table 1 and Fig.2.

Table 1: Average results of activity concentration of ^{222}Rn in groundwater collected in points of the three aquifers using different sampling methods. The version direct or indirect of the SEPA method is indicated between brackets.

SC[a]	AQ[b]	Access point	Activity concentration ($Bq \cdot L^{-1}$)		
			SEPA [DIR or IND]	PUMP	BOTT
5	1	BORE	1066(25) [DIR]	831(20)	617(18)
5	2	TANK	454(11) [IND]	448(11)	417(10)
5	2	FAUC	447(11) [IND]	441(11)	399(10)
6	3	TANK	728(17) [IND]	687(16)	682(16)
6	3	FAUC	438(11) [IND]	440(11)	432(10)
7	1	BORE	1949(45) [DIR]	1400(33)	1322(31)
7	1	FAUC	21.3(0.7) [DIR]	17.4(0.6)	17.8(0.6)

[a]SC: Sampling campaign; [b]AQ: Aquifer

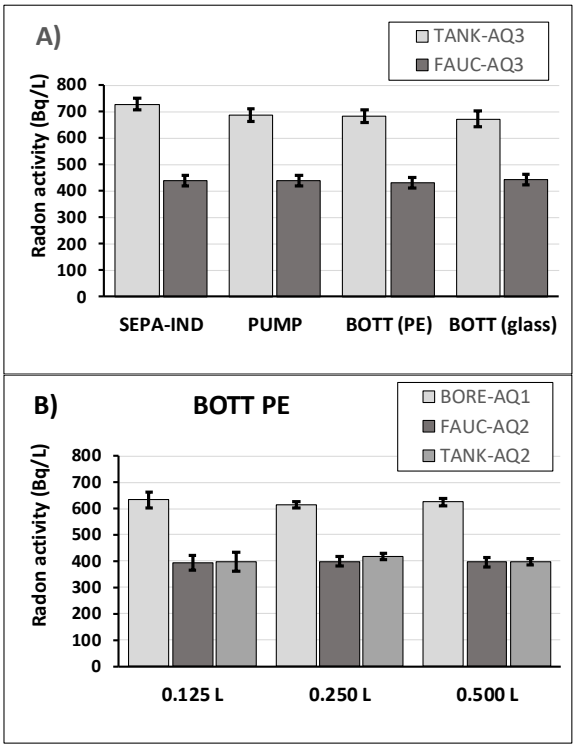

Fig. 2: Influence of the size and material of the bottles using the "*ex situ*" BOTT method on the activity concentration of ^{222}Rn for samples collected in different points. Chart A): effects of the bottle material and comparison with other sampling methods; chart B): effects of the polyethylene bottle size.

Although a clear positive trend is observed for the activity concentration ratio TANK/FAUC as the activity concentration of ^{222}Rn increases, no objective reason has been found except the characteristics of each point for the different aquifers.

3.3. Sampling methods

During the third and fourth campaigns, samples were taken from the BORE point using different sampling methods, already discarding at this point the method of the depressurized syringe (DEPR). The results of these two campaigns are listed in Table 2. For comparison effects, Table 2 also shows the weighted average values per sampling method, considering that the level of the water table and the temperature were practically constant during these two campaigns, and so few differences were expected for the activity concentration of ^{222}Rn.

Table 2: Activity concentration of ^{222}Rn in groundwater (Bq·L^{-1}) collected at BORE point of the aquifer AQ1 using different sampling methods. Results were obtained for the third and fourth campaigns.

Sampling method	SEPA-DIR	PUMP	BOTT (PE, 250 mL)
	1871(43)	1473(34)	1281(30)
	1820(42)	1481(34)	1289(30)
	1779(41)	1396(32)	1312(31)
	1740(40)	1435(33)	1328(31)
	1883(43)	1745(40)	1728(40)
	1601(37)	1578(36)	1771(41)
	1974(45)	1649(38)	1795(42)
	1908(44)	1382(32)	1701(39)
Weighted average	1809(117)	1500(130)	1463(250)

While the results obtained applying either PUMP or BOTT (PE, 250 mL) methods are statistically compatible, the use of the SEPA method in its direct version (SEPA-DIR) provided greater activity concentrations of ^{222}Rn in the water collected at the BORE point of AQ1.

In campaigns 5, 6, and 7, samples were collected using the same sampling methods, also including results of applying the SEPA-IND method. Again, the statistical compatibility between PUMP and BOTT results is observed, but also their similarity with SEPA-IND results. On the other hand, the activity concentrations of ^{222}Rn obtained from the direct version SEPA-DIR were higher than those obtained using the PUMP and BOTT methods. The activity values have been already shown in Table 1. Similar conclusions are obtained from the data represented in Fig. 3 where all those methods were applied for sampling in the BORE point of AQ1.

The values obtained from BORE point of AQ1 using SEPA-DIR, PUMP and BOTT (PE, 250 mL) methods were tested by means of variance analysis (ANOVA). The results of the Post-Hoc comparison are shown in Table 3 in which three different tests (Tukey´s HDS, DMS, and Bonferroni) have been applied.

From this analysis, it can be seen that the "*in situ*" method SEPA-DIR offers significantly greater activity concentrations of ^{222}Rn than those obtained with the rest of the methods. The use of the submerged pump causes slight losses, but its preparation "*in situ*" provides performances similar to those obtained with the "*ex situ*" BOTT method, so the choice of one method or another will be reduced to its practicality.

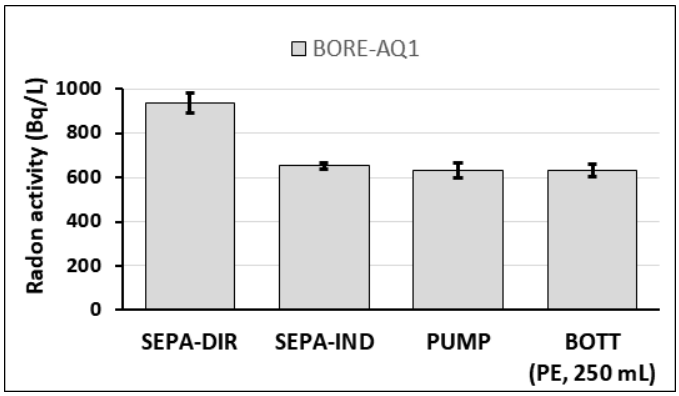

Fig. 3: Comparison between the different sampling methods applied to samples from the survey BORE of AQ1 during the sixth campaign.

Table 3: Post-Hoc comparison between three sampling methods: SEPA-DIR, PUMP, and BOTT (PE, 250 mL).

Test	Method (i) vs Method (j)	Average diffs.(i-j)	Sign.	Results
Tukey's HSD	SEPA-DIR vs PUMP	326.9	0.032	*
	SEPA-DIR vs BOTT	370.9	0.013	*
	BOTT vs PUMP	-44.1	0.913	NS
DMS	SEPA-DIR vs PUMP	326.9	0.012	*
	SEPA-DIR vs BOTT	370.9	0.005	**
	BOTT vs PUMP	-44.1	0.725	NS
Bonferroni	SEPA-DIR vs PUMP	326.9	0.036	*
	SEPA-DIR vs BOTT	370.9	0.014	*
	BOTT vs PUMP	-44.1	1.000	NS

Significance level: 0.05 ; variance homogeneity test (Levene's statistic): Sig. value 0.743.
ANOVA result before the Post-Hoc analysis: Sig. 0.034; $F_{Snedecor}$: 5.332.
Results: *Significant; **Highly significant; NS. Not significant.

3.4. Volume and material of the bottles

From samples taken in campaign 5, results of which are shown in Fig. 2, it was shown that the size of the bottle for the transport of the sample had no influence on the final concentration results. Between 150 mL, 250 mL and 500 mL bottles, the average concentration ranges were [632(15) – 617(17) Bq·L^{-1}] for the samples taken in AQ1. For the second aquifer, the same bottles produced ranges [417(10) – 396(9) Bq·L^{-1}] and [399(9) – 394(9) Bq·L^{-1}] in the samples taken in the TANK and FAUC points, respectively.

Samples were also collected using 1000 mL glass bottles with a screw cap with a Teflon-septum. They were used to collect samples from the FAUC and TANK points of AQ3 in order to compare the results with those obtained using 250 mL polyethylene bottles (Fig.2A). The average results obtained were: for FAUC point, 430(10) Bq·L^{-1} with glass bottle, and 432(10) Bq·L^{-1} with the polyethylene bottle; for TANK point, 672(30) Bq·L^{-1} with the glass bottle, and 682(24) Bq·L^{-1} with the polyethylene bottle.

Neither glass nor polyethylene determines *per se* the radon diffusion. Rather, it is the existence of a gaseous phase (air volume) in the bottle, which causes the gas diffusion and losses of ^{222}Rn in the water.

4. Conclusions

This study assesses the influence that, in relative terms, both the characteristics of the different access points to an aquifer and the application of different sampling methods have on the determination of the activity concentration of ^{222}Rn in groundwater.

Given an aquifer, significant differences are found in the activity concentrations for samples obtained from the different access points, mainly due to the way in which the water is brought to the surface at these points. The results obtained for samples collected in the upwelling indicate significant losses of ^{222}Rn when they are compared to the activity concentrations of samples directly obtained from the water body. Even between access points of similar typology (TANK and WELL), it is possible to observe different results, which are attributable to local characteristics.

Being not always possible to access the body of water, it is the authors' opinion that surveillance with health protection purposes should not only be linked to the aquifer in question, which is variable mainly due to environmental factors, but also to its access points where other specific factors must be considered. Then, the sampling methods to be recommended should give information about the activity concentration of ^{222}Rn in the upwelling water. The regularization of the response of different sampling methods can be achieved with indirect methods, using a bucket of enough volume where continuous flow is maintained for sampling.

If the access to the water body is of concern and it is feasible, the "*in situ*" method SEPA-DIR (syringe plus an extensible pole, if necessary) provides the greater activity concentrations, higher than the method based on a depressurized syringe (DEPR), which did not provide satisfactory results, or by the use of a low flow pump (PUMP).

On the other hand, using an intermediate bucket, the results of applying the methods SEPA-IND, PUMP, and the "*ex situ*" BOTT, were statistically compatible with each other. From a practicality point of view, the "*in situ*" SEPA-IND method will be preferred. However, if the sampling plan requires it, the use of hermetic bottles for the transport of the samples to the laboratoty for the vial preparation (BOTT method) is also a valid alternative. Hermetic bottles of high density polyethylene and 250 mL are a practical choice as long as the absence of air bubbles is ensured.

References

Both, R., Arribas, A. and Saint-André, B., 1994. The origin of breccia-hosted uranium deposits in carbonaceous metasediments of the Iberian Peninsula: U–Pb geochronology and stable isotope studies of the Fé deposit, Salamanca province, Spain. Econ. Geol. 89, 584-601.

Burkhart, J. F., Gray & D., Martin, R.D., 1991. A Comparison of Current Collection/Sampling Techniques for Waterborne Radon Analysis. Annual AARST National Fall Conference. Preprints, Vol. 11.

CSN, 2000. Consejo de Seguridad Nuclear. Proyecto Marna. Mapa de radiación gamma natural (Reference: INT-04-02).

De Felice, P., Jerome, S., Petrucci, A., 2017. Practical implementation of ISO 11929: 2010. Applied Radiation and Isotopes, 126, 256-262.

Jobbagy, V., Stroh, H., Marissens, G., Hult, M., 2019. Comprehensive study on the technical aspects of sampling, transporting and measuring radon-in-water. Journal of Environmental Radioactivity, 197, 30–38.

Martínez-Alegría, R., Sanz, G., Oliveira, S., Montequi, I., Campos, F., 2014. Spanish Nuclear Industry - Future perspectives and reserves' analysis. Procedia Earth and Planetary Science, 8, 81-85.

WHO, 2015. Manual de la OMS sobre el radón en interiores. Una perspectiva de salud pública. (ISBN 978 92 4 354767 1)

Price, S. G. & Alvarez, B.V., 1999. Radon in Water Sampling Problems May Cast a Dark Shadow Over the Most Recent Federal Regulations. J. L. Alvarez, Ph.D. Auxier and Associates. Oak Ridge, TN.

Quindós Poncela, L.S., Fernández Navarro, P.L., Gómez Arozamena, J., Ródenas Palomino, C., Sainz, C., Martin Matarranz, J.L., Arteche, J., 2004. Population dose in the vicinity of old Spanish uranium mines. Sci. Total Environ., 329, 283-288.

Towards a suitable gross α and β activity determination in drinking water

Borrego D.*, Quintana B., Lozano J.C., Pedrosa M.C., Marcos M.T.

Ionizing Radiation Laboratory, Department of Fundamental Physics, University of Salamanca, Spain.

Abstract

Drinking water samples from Castilla y León (Spain) have been studied to establish a leading protocol to provide reliable gross alpha and beta activities of the radionuclide content. These samples were also radiologically characterised by measuring the main natural radionuclides by γ-ray spectrometry and α-particle spectrometry. Counting sources were prepared following the evaporation method and were directly spiked with several standard solutions for efficiency calculation. Natural uranium has shown to be the most suitable standard to obtain reliable gross alpha and beta activities.

Keywords: gross α activity, gross β activity, drinking water, direct efficiency, cross-talk

* Corresponding author, e-mail address: davidin@usal.es

1. Introduction

Gross alpha and beta activity (gross α/β) determinations are commonly used as screening techniques in environmental monitoring. According to European Council Directive 2013/51/Euratom (EURATOM, 2013) and the current Spanish legislation (RD, 2016), screening levels for gross α/β activities in drinking water are 0.1 Bq/L and 1.0 Bq/L, respectively. Specific radionuclides need to be determined when these established limits are surpassed. Nevertheless, the analysis of gross α/β activities in drinking waters from different provenance is not exempted from analytical difficulties that, when not solved, lead to failures in the decisions adopted following the obtained results. Specific radionuclides could be alternatively determined using spectrometric techniques, which are more expensive. Therefore, it is paramount to the application of a suitable gross α/β analysis to provide a robust predictive power avoiding, on the one hand, potentially hazardous health effects to the population and, on the other hand, unnecessary extra costs. The methods applied for gross α/β activity determination are not exempted of some drawbacks and, at certain times, unreliable, and non-comparative gross activity results are consequently reported (Jobbágy et al., 2014). So it is crucial to know the real content of radionuclides of the water samples and parameters such as the radionuclides used for efficiency determination or the volume of the aliquot of the sample analysed should be stated.

Radioactivity in drinking water from several water resources distributed throughout the Castilla y León region was monitored and analysed since 2017 in our laboratory. Radionuclides present in the studied water samples came mainly from the uranium and thorium decay series. The granitic rocks and slates which occupy the entire western Castilla y León region show the highest natural uranium concentrations of Spain. Accordingly, the uranium concentration values reported in the soils derived from these rocks are significantly higher than the worldwide earth crust mean values (Santos-Francés et al., 2018), highlighting the drinking waters from this study area as potentially hazardous to human consumption. The radionuclides reached water masses from the bedrock minerals by weathering and leaching in a concentration that depends on the water chemical conditions. Overall, the primary process for the uranium transfer from the bedrock and soils to water masses are the redox reactions. Oxidising conditions increase the solubility of uranium and its concentration in the water samples. Therefore, it is essential to keep in mind the geological context of hydric resources in the gross α/β analysis approach because the method employed can be highly dependent on the chemical composition.

One of the most extended and accepted methods for gross α/β activity determination in drinking water is the one based on evaporation of an aliquot to complete dryness in a stainless steel planchet, which is measured in a gas flow proportional counter (ISO, 2019). Furthermore, co-precipitation and total evaporation/LSC methods could be applied to assess gross activities (Montaña et al., 2013). The gross α and β activities determined with the proportional counter from now on will be referred to as I_α and I_β, respectively. It is widely known that in many laboratories, synthetic water matrices are prepared with different substrate concentrations (i.e. Na_2CO_3) to obtain efficiency calibration curves (Ruano Sánchez et al., 2013). However, the chemical composition in real drinking water samples usually is a mixture of substrates in different proportions, which lead to a wide range of efficiency values. It is the reason why efficiency evaluation is made in our laboratory at the University of Salamanca for each sample by direct spiking with a standard radionuclide solution, which provides a direct efficiency determination that is fully representative of the chemical composition of each sample and, consequently, minimises systematic deviations.

The main objective of this work is to lay down a procedure leading to a significant upgrade in the predictive power of I_α and I_β. The method is based on the measurement of several replicas, some of them directly spiked in order to determine efficiencies and cross-talk, which ensures the reproducibility of the measurement and the correct efficiency determination. For this purpose, ^{241}Am, ^{90}Sr, ^{210}Pb, natural uranium and ^{210}Po standard solutions with different emission energies are tested for a proper direct efficiency estimation. The ^{90}Sr/^{90}Y standard solution was also used to evaluate the ^{40}K contribution to I_β correcting deviations in the results due to this contribution. Furthermore, in order to minimise the effect of other factors such as chemical composition and non-uniformities in residue mass, the aliquot volume was adjusted. Residue mass (m_r) could be decisive since the energy loss of α-particles for I_α calculation is especially significant (Jobbágy et al., 2010). Finally, but also important, alternatives to the use of a ^{241}Am solution are studied in order to obtain a proper α-to-β cross-talk factor ($c_{\alpha\text{-}\beta}$), defined as the α counts detected in the β channel. Specifically, a natural uranium solution, free of β emitters, was studied. This method shows some highlighted advantages such as the relatively quick and low-cost sample preparation, high overall yield, while the chemical composition is almost unaltered. Results show, as seen in section 3, excellent performance of the overall method, which allows obtaining some general conclusions about the gross α and β analysis.

2. Material

2.1 Water samples

Since 2017, more than two hundred drinking water samples were analysed in our laboratory for the Regional Health Council. Its staff collected 25 L samples from water intakes spread all over Castilla y León. This region is the largest one of Spain consisting of nine provinces (Ávila, Burgos, León, Palencia, Salamanca, Segovia, Soria, Valladolid, and Zamora) with a diverse geological context (granites, shales, limestones, sandstone) and devoted mainly to agricultural and farming practices. The water intakes considered in the study were located in the proximities of villages and cities. The samples contained in 5 L vessels were received in our lab where, immediately, their electrical conductivity (σ) was measured, and they were acidified with 1 mL/L of 69% HNO_3 for conservation.

2.2 Radionuclide standard solutions

The standard solutions considered in order to calculate a reliable efficiency were: a 100.1(18) Bq/g ^{210}Pb solution, a 417.3(85) Bq/g ^{90}Sr/^{90}Y solution (in secular equilibrium), a 966.7(97) Bq/g ^{241}Am solution, 1.9337(89) Bq/g ^{209}Po solution, and a natural uranium solution with 7.70(18) Bq/g, corresponding to the α emitters and 7.69(13) Bq/g corresponding to the β ones. The first three were provided by CIEMAT and the ^{209}Po solution by NIST. The ^{210}Pb solution also contained ^{210}Bi and ^{210}Po in secular equilibrium with their progeny. The natural uranium solution was characterised in our laboratory by α-particle and γ-ray spectrometry.

2.3 Preparation of samples

The general protocol followed to prepare counting sources consists of several steps. First, water aliquots were concentrated by evaporation on a heater plate at a constant temperature of 85 ºC. Once reduced to 5 mL, evaporation to dryness is performed in stainless steel planchets previously weighed and registered. 9-ridges stainless steel planchets have an area of 26 cm^2 and have been made by a non-commercial manufacturer. This step was carried out using a system of infrared lamps, which assures a uniform temperature of 45 ºC on the platform where planchets were placed. Third, once water aliquots are entirely evaporated, planchets were stored in a desiccator during 24-72 hours, weighed and placed on the detector.

From the whole of drinking water samples, a set of twenty-four samples referred to as DW01, DW02, DW03,…, DW24 were chosen to test the evaporation method by taking aliquots with constant volume, specifically V = 100 mL. One of the four replicas prepared of each sample was spiked with 10 µL of ^{210}Pb/^{210}Po/^{210}Bi standard solution in order to assess the efficiency. However, some m_r values were higher than 150-200 mg, which produced an irregular residue distribution on the planchets. In these cases, sources corresponding to the same samples became statistically different.

At this point, the procedure was changed, aliquot volumes were varied according to the electrical conductivity (σ) of the samples. DW01 to DW24 samples were prepared following this approach to obtain a constant m_r in the planchets. The proper volume was determined by using the linear relation between m_r, obtained taking V = 100 mL, and σ. For each sample, the aliquot volume was individually calculated applying the least-squares regression obtained from the experimental data shown in Fig. 1, in which a strong linear correlation (R^2=0.9224) was observed. It is worth pointing out that eighty-one drinking water samples were employed to obtain this linear fit. An interval of tolerance for the residue mass m_r was established to minimise the energy loss of α-particles, but ensuring mass enough to guarantee a functional minimum activity detection level and a regular deposit. We calculated the thickness to produce an energy loss of 15-20% for the most intense alpha emission of ^{238}U, E_α = 4198 keV (I_α = 77.5%). In a transmission simulation, the SRIM-2013 software (Ziegler et al., 2010; Ziegler, 2019) was used to calculate the corresponding range, R. A theoretical residue matrix made up of Na_2CO_3 was considered for this purpose, obtaining R values in the interval between 6.17 and 8.23 µm. The equivalent values for m_r were 28.9 and 38.5 mg, respectively, and were obtained taking into account the planchet area, A = 26 cm^2, and the sodium carbonate density, ρ = 1.8 g/cm^3. Then, a compromise value of m_r = 30 mg was selected as target value to determine the aliquot volume for each water composition by using the curve shown in Fig 1.

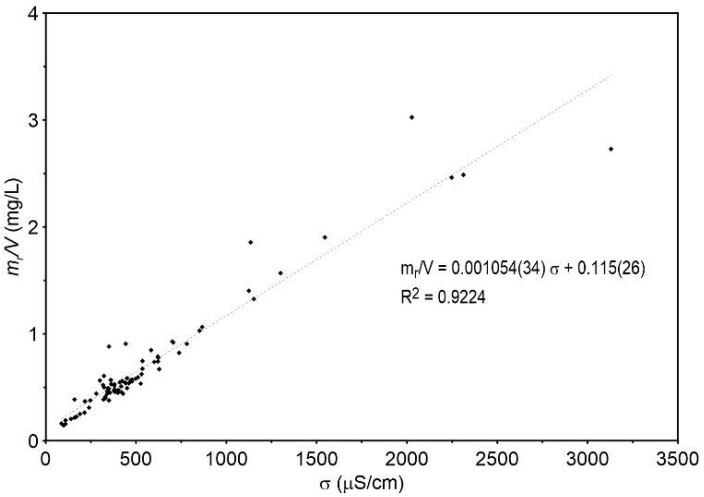

Fig. 1: Residue mass per aliquot volume of 100 mL, m_r/V, measured in mg/L versus electrical conductivity, σ, in µS/cm. The dashed line represents the linear fit obtained by using the least-squares method. The result of this linear fit is also given, including the linear correlation statistic, R^2.

2.4 Measurement equipment

Measurements were performed with a Berthold LB770 gas-flow proportional counter. Counting planchets were placed in the ten 2π-solid-angle ionisation chambers supplied with the P10 gas mixture (90% Ar and 10% methane). This equipment enabled simultaneous α and β measurements in two independent channels. Underground location, active and additional passive shielding ensured a low detector background, which is in average 0.02 cpm in the α channel and 0.4 cpm in the β one.

Gamma-ray spectrometry was performed with a coaxial p-type Canberra BEGe detector (Quintana et al., 2018). The α-particle spectrometry was performed using an Alpha Ensemble-8 (Ortec-Ametek) with eight ultra-low background PIPS detectors.

3. Results and discussion

The analysis of uranium (^{238}U, ^{235}U and ^{234}U), thorium (^{232}Th, ^{230}Th and ^{228}Th) and radium (^{228}Ra, ^{226}Ra and ^{224}Ra) isotopes, as well as ^{210}Po, ^{210}Pb and ^{40}K were performed in all the samples by α-particle spectrometry using PIPS detectors (Hallstadius, 1984; Lehritani et al., 2012) and low-background γ-ray spectrometry using a HPGe detector (Quintana et al., 2018). The determination of the radionuclide activity concentrations allowed calculating the sum of α and β activities (Σ_α, Σ_β), which can be compared with I_α and I_β, respectively. Σ_α is obtained considering the following radionuclides: ^{210}Po, ^{238}U, ^{234}U, ^{235}U, ^{226}Ra, and ^{224}Ra; while Σ_β was calculated adding the contribution of ^{210}Pb, ^{210}Bi, ^{234}Pa, ^{234}Th, ^{228}Ra and ^{40}K activities. Negligible activities of ^{232}Th, ^{230}Th, and ^{228}Th were reported in all drinking water samples analysed. Therefore, they were not taken into account in Σ_α and Σ_β.

Table 1: Σ_α, I_α, I_α/Σ_α and t obtained from DW01 to DW24 samples. Results were ordered from lower to higher Σ_α. Superscript C refers to values obtained from counting sources prepared with 100 mL aliquots. Superscript V refers to values obtained for aliquot volumes adjusted to produce a residue mass m_r = 30 mg. Results in bold correspond to the samples whose t-Student value was $t < 1.96$.

Sample	Σ_α (Bq/m^3)	$I_\alpha{}^C$ (Bq/m^3)	$I_\alpha{}^V$ (Bq/m^3)	$I_\alpha{}^C/\Sigma_\alpha$	$I_\alpha{}^V/\Sigma_\alpha$	t^C	t^V
DW06	13.4(12)	15.8(46)	18.1(28)	1.18(36)	1.35(24)	**0.52**	**1.58**
DW18	32.7(21)	46(28)	31.2(31)	1.39(86)	0.95(11)	**0.46**	**0.39**
DW19	60.2(52)	47.7(35)	42.0(62)	0.70(12)	0.792(90)	2.23	1.98
DW23	87.1(24)	161(19)	153(14)	1.85(22)	1.76(17)	3.93	4.65
DW11	115.5(48)	192(12)	115.8(70)	1.66(12)	1.003(73)	6.11	**0.04**
DW14	158.4(79)	92.8(81)	57.4(94)	0.586(59)	0.363(62)	5.80	8.26
DW17	185.7(64)	183(14)	171.3(93)	0.987(84)	0.923(59)	**0.16**	**1.27**
DW20	232(12)	80(16)	126(12)	0.346(72)	0.544(60)	7.61	6.22
DW12	239.0(20)	299(15)	911(33)	1.250(65)	3.81(14)	3.88	20.42
DW05	265.5(66)	189(22)	93.3(72)	0.713(83)	0.351(28)	3.38	17.70
DW24	269.7(15)	93.5(75)	220(48)	0.347(34)	0.81(18)	10.45	**1.00**
DW08	280(42)	585(45)	785(43)	2.09(35)	2.81(44)	4.96	8.49
DW01	280.8(38)	220(13)	173(13)	0.785(48)	0.617(48)	4.40	7.77
DW10	371.3(46)	197(18)	203(14)	0.530(48)	0.547(39)	9.64	11.34
DW03	392(22)	222(18)	198(22)	0.567(56)	0.504(64)	5.95	6.16
DW04	402.9(17)	238(16)	201(30)	0.591(47)	0.498(77)	7.03	5.90
DW22	442(10)	938(173)	380(79)	2.12(39)	0.86(18)	2.87	**0.78**
DW02	452(43)	291(31)	281(12)	0.645(92)	0.622(66)	3.01	3.79
DW07	503.9(88)	398(27)	175(40)	0.790(55)	0.348(80)	3.78	8.02
DW16	505.4(82)	419(47)	353(19)	0.828(94)	0.699(39)	**1.82**	7.32
DW21	613(53)	195(15)	269(21)	0.318(37)	0.438(52)	7.55	6.00
DW09	828(25)	567(52)	804(68)	0.684(66)	0.971(87)	4.54	**0.33**
DW15	1771(88)	915(206)	1274(51)	0.52(12)	0.719(46)	3.81	4.86
DW13	3439(241)	2830(168)	3384(140)	0.823(76)	0.984(80)	2.07	**0.20**

3.1 Determination of ε_α and ε_β using ^{210}Pb solution for efficiency calculation

For efficiency calculation, a ^{210}Pb solution in equilibrium with its descendants, ^{210}Bi and ^{210}Po, was chosen because it allowed the calculation of ε_α and ε_β at the same time. Two sets of sources spiked with ^{210}Pb were prepared from water samples DW01 to DW24. In the first set, the sources were prepared with constant 100 mL volume aliquots of each water. The second set was prepared to adjust the volume of water to approximately obtain a constant m_r of 30 mg for each source.

The I_α and I_β values obtained for the DW01 to DW24 samples showed significant deviations concerning Σ_α and Σ_β, as shown in Tables 1 and 2. The deviations which resulted when the aliquot volume was chosen to obtain an approximately constant m_r were also significant. The average values of the relative uncertainties for I_α were 13.1 and 9.9 % for constant and adjusted volumes, respectively, pointing out that a better reproducibility was achieved when sources were prepared using a constant m_r. Average values of I_α/Σ_α were 0.611(35) and 0.622(66) for constant and adjusted volume, respectively, which meant that ε_α was overestimated when using the ^{210}Pb solution. This fact can be explained by the different energy range of the α particles emitted by the natural radionuclides contained in the samples in relation to the energy of ^{210}Po. Most of the samples showed high activity concentrations of natural uranium, becoming the main component in the drinking water samples analysed. Student t values indicated I_α results to be slightly better for constant m_r than for V = 100 mL. The average values of I_β/Σ_β were 1.208(73) and 0.643(78) for constant and adjusted volume, respectively. These results indicate a different trend for I_β results obtained with constant volume compared to those obtained with a volume taken to get approximately constant m_r. This effect can be attributed to the low energy of one of the ^{210}Pb β emissions, which in average is E_β = 4.3 keV. The higher residue obtained for 100 mL aliquots made that ε_β was widely underestimated. This effect disappeared with 30 mg residues, but still, the β energy range of ^{210}Pb solution is different from the one of the leading natural radionuclides present in the samples. These results suggested that the ^{210}Pb solution was not suitable for I_α and I_β determination of the drinking water samples analysed. These results also suggested that efficiency determination using radionuclides with β emission energies closer to the primary energy of β emitters present in the samples studied could significantly improve I_α and I_β determinations.

3.2 Determination of ε_α and ε_β using ^{241}Am, ^{90}Sr/^{90}Y, ^{209}Po and natural uranium for efficiency calculation

In order to choose the best match for the ε_α and ε_β determination, ^{241}Am, ^{90}Sr/^{90}Y, natural uranium, and ^{209}Po standard solutions were chosen to obtain spiked counting sources corresponding to DW02, DW11 and DW15 water samples. These samples were selected because they showed significant differences in their activity concentrations, they produce different m_r values starting from the same aliquot volume, and they present significant deviations in the previous tests, as seen in Tables 1 and 2. Water samples were prepared, taking a constant m_r = 30 mg. Counting sources spiked with natural uranium provided lower ε_α and ε_β values than using ^{241}Am,

leading to the best I_α and I_β values when compared with Σ_α and Σ_β, as shown in Table 3. The deviations in I/Σ ratios were overall reduced in these samples analysed, obtaining the following results: I_α/Σ_α = 1.07(11) and I_β/Σ_β = 1.24(12) for DW02 sample; I_α/Σ_α = 1.66(14) and I_β/Σ_β = 1.04(13) for DW11 sample; and, finally, I_α/Σ_α = 1.066(71) and I_β/Σ_β = 0.957(52) for DW15 sample. Nevertheless, I_α results did not show significant differences when spiking with natural uranium or ^{241}Am as can be checked in Table 3. Therefore, both choices led to high I_α values. Finally, ε_α is strongly underestimated when the ^{209}Po solution was used (ranging from 7.8% to 11%), due likely to its higher emission energies (Table 3), which led to discarding ^{209}Po to determine I_α values.

Another set of sources from samples DW25 to DW109 was prepared using natural uranium for efficiency calculation. The sources were prepared with constant m_r = 30 mg. Results showed suitable I_α values, as seen in Fig. 2, leading to obtaining more reliable activity in the samples analysed.

Regarding the appropriate radionuclide to calculate ε_β, the results showed that the ^{90}Sr led to an overestimation of ε_β, probably due to the low β emission energies of the radionuclides contained in the analysed samples. However, the results of I_β improved when using natural uranium as a consequence of a better ε_β determination through the beta energies of the ^{238}U descendants, as seen in Table 3.

Table 2: Σ_β and I_β, I_β/Σ_β and t obtained from DW01 to DW24 samples. Results were ordered from lower to higher Σ_β. Superscript *C* refers to values obtained from counting sources prepared with 100 mL aliquots. Superscript *V* refers to values obtained for aliquot volumes adjusted to produce a residue mass m_r = 30 mg. Results in bold correspond to the samples whose *t*-Student value was $t < 1.96$.).

Sample	Σ_β (Bq/m^3)	$I_\beta{}^C$ (Bq/m^3)	$I_\beta{}^V$ (Bq/m^3)	$I_\beta{}^C/\Sigma_\beta$	$I_\beta{}^V/\Sigma_\beta$	t^C	t^V
DW18	40.5(26)	ND	93(24)	-	2.30(62)	-	2.14
DW06	50.1(31)	79(12)	59(15)	1.58(25)	1.18(31)	2.43	**0.59**
DW19	63.0(93)	122(10)	108.9(93)	1.93(33)	1.73(29)	4.22	3.50
DW17	81.7(91)	87(15)	77.5(9.6)	1.06(22)	0.95(16)	**0.28**	**0.32**
DW14	104.9(56)	98(38)	93(24)	0.93(36)	0.89(24)	**0.19**	**0.48**
DW05	126.2(66)	341(50)	244(33)	2.70(42)	1.93(28)	4.23	3.46
DW23	150(16)	215(30)	191(29)	1.43(26)	1.27(24)	**1.88**	**1.23**
DW16	184.4(51)	243(22)	462(228)	1.32(13)	2.51(16)	2.54	9.89
DW20	191.8(23)	413(22)	554(58)	2.15(12)	2.89(31)	10.07	6.19
DW04	239.7(53)	391(26)	663(104)	1.63(11)	2.77(44)	5.69	4.08
DW03	282.9(67)	573(108)	598(71)	2.03(39)	2.11(25)	2.68	4.44
DW02	311(25)	302(21)	444(18)	0.97(10)	1.43(13)	**0.27**	4.35
DW07	326.7(64)	561(44)	909(195)	1.72(14)	2.78(60)	5.25	2.98
DW10	334.9(73)	423(37)	706(47)	1.26(11)	2.11(15)	2.34	7.83
DW24	353(13)	822(47)	819(171)	2.33(16)	2.32(49)	9.63	2.71
DW11	413(35)	706(74)	737(32)	1.71(23)	1.78(17)	3.57	6.87
DW21	423(11)	381(35)	602(50)	0.899(85)	1.42(13)	**1.17**	3.46
DW01	498(23)	868(42)	1144(68)	1.74(14)	2.30(20)	7.00	8.65
DW22	548(18)	1317(70)	1204(254)	2.40(15)	2.20(47)	10.68	2.58
DW09	846(21)	1019(92)	1902(137)	1.20(11)	2.25(17)	**1.84**	7.61
DW12	1150.2(10)	1046(53)	463(18)	0.910(46)	0.402(16)	**1.95**	37.77
DW15	1161(40)	863(165)	1024(44)	0.74(15)	0.882(49)	**1.75**	2.30
DW08	1204(21)	1214(56)	1331(54)	1.008(50)	1.106(49)	**0.17**	2.19
DW13	2290(68)	2915(167)	3116(126)	1.273(82)	1.361(68)	3.46	5.77

Table 3: Σ_α, I_α, Σ_β, I_β, ε_α and ε_β resulting from the analysis of DW02, DW11, and DW15 samples using different radionuclides for efficiency calculation.

Sample	Σ_α(Bq/m^3)	Σ_β(Bq/m^3)	Standard solution	ε_α (%)	I_α(Bq/m^3)	ε_β (%)	I_β (Bq/m^3)
DW02	452(43)	311(25)	^{241}Am	18.8(14)	441(28)	-	-
			^{209}Po	8.69(14)	808(50)	-	-
			^{90}Sr	-	-	42.4(10)	308(36)
			^{nat}U	14.05(35)	482(23)	26.26(48)	387(21)
DW11	115.5(48)	413(35)	^{241}Am	13.4(14)	179(17)	-	-
			^{209}Po	7.80(39)	238(20)	-	-
			^{90}Sr	-	-	43.2(11)	380(19)
			^{nat}U	10.05(25)	192(14)	25.79(47)	429(37)
DW15	1771(88)	1161(40)	^{241}Am	17.9(11)	1692(95)	-	-
			^{209}Po	11.21(52)	2176(130)	-	-
			^{90}Sr	-	-	44.2(11)	717(30)
			^{nat}U	17.52(44)	1888(83)	26.83(50)	1113(47)

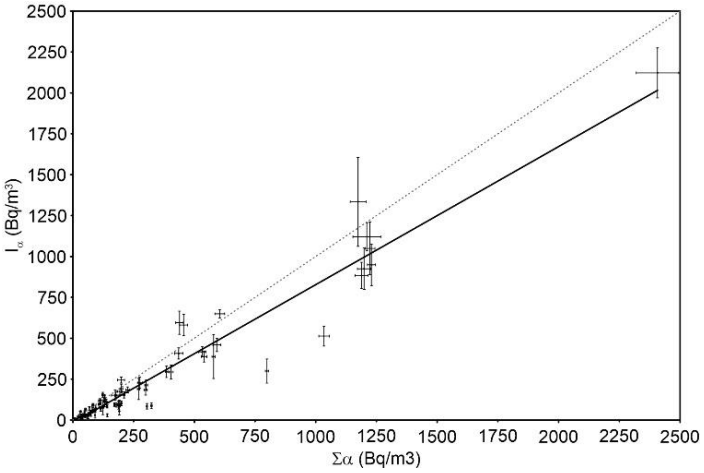

Fig. 2: Gross-alpha activity I_α (Bq/m^3) obtained using natural uranium for efficiency calculation versus the sum of alpha activity Σ_α (Bq/m^3) calculated considering the contribution of ^{210}Po, ^{238}U, ^{234}U, ^{235}U, ^{226}Ra and ^{224}Ra activities. The values depicted with black dots correspond to the water samples referred to as DW025 to DW109. The solid line represents the linear fit obtained from the water samples studied. $I_\alpha = \Sigma_\alpha$ is plotted as a reference (dotted line). Uncertainties are given as 1σ.

3.3 The ^{40}K correction

Since the use of ^{238}U β daughters was shown to improve the evaluation of ε_β, use of the ^{90}Sr solution appeared suitable when the contribution of ^{40}K is significant in the sample, because its average β emission energy of 508.32 keV is included in the β emission range of the ^{90}Sr/^{90}Y solution, with an average β energy of 196 keV for ^{90}Sr and 926.7 keV for ^{90}Y. Therefore, an appropriate correction was proposed to evaluate the contribution of ^{40}K to I_β, reducing the distorting effect of ^{40}K in its accurate determination, given that not all samples contained ^{40}K to the same extent.

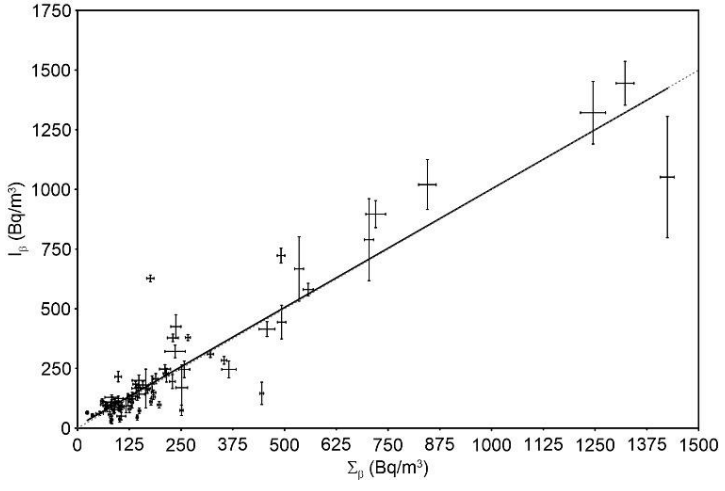

Fig. 3: Gross-beta activity I_β (Bq/m^3) obtained using natural uranium for efficiency calculation versus the sum of alpha activity Σ_β (Bq/m^3) calculated considering the contribution of ^{210}Pb, ^{210}Bi, ^{234}Pa, ^{234}Th, ^{228}Ra and ^{40}K activities. The values depicted with black dots correspond to the water samples referred to as DW025 to DW109. The solid line represents the linear fit obtained from the water samples studied. $I_\beta = \Sigma_\beta$ is plotted as a reference (dotted line). The α-to-β cross-talk factor ($c_{\alpha\text{-}\beta}$) and the ^{40}K correction were also considered. Uncertainties are given as 1σ.

Previous studies had shown that the higher the ^{40}K activity in the samples, the better the I_β obtained when spiking with the ^{90}Sr solution. Thus, the sources spiked with ^{90}Sr prepared with aliquots of the water samples DW26 to DW109 were used to calculate the corresponding β counting rate for each sample. The ^{40}K activity obtained by γ-ray spectrometry and the ε_β calculated from the ^{90}Sr-spiked counting source provided the counting rates by using the mathematical relation between counting rate and activity. Afterwards, the ^{40}K-free I_β was calculated using the ε_β values obtained with the natural uranium solution. Finally, the ^{40}K activity concentration result was added to obtain the total I_β. Results obtained applying the ^{40}K correction were compiled in Table 2.

3.4 Determination of cross-talk $c_{\alpha\text{-}\beta}$

Accurate $c_{\alpha\text{-}\beta}$ values are needed to evaluate the β counting rates correctly when high activities are present in the counting sources (García-León et al. 1984; Semkow and Parekh, 2001). The $c_{\alpha\text{-}\beta}$ is influenced mainly by the residue characteristics. The first approach employed in this work to calculate $c_{\alpha\text{-}\beta}$ was to use the four ^{241}Am-spiked sources prepared with DW09, DW10, DW11, and DW15 aliquots. The $c_{\alpha\text{-}\beta}$ values obtained gave an average of 41.264(12) %. When these values were applied, the I_β obtained were lower than Σ_β. This likely overestimation of $c_{\alpha\text{-}\beta}$ could come from the low-energy ^{241}Am electromagnetic emissions together with conversion electrons emitted in the ^{241}Am disintegration. Thereby, a radionuclide free of this kind of emissions and, at the same time, in the α-energy range of the radionuclides commonly contained in the analysed samples was tested for $c_{\alpha\text{-}\beta}$ evaluation. An α-pure standard solution of uranium was prepared from the natural uranium one by radiochemical separation of the ^{234}Th β emitter. The procedure consisted of the precipitation of Th(IV) as fluoride with the addition of Nd^{3+} in excess and 48% hydrofluoric acid and stirring in the cold, once ensured the oxidation state of U(VI) by adding hydrogen peroxide. U(VI) remains dissolved in these conditions. The resulting solution was filtered to retain ^{234}Th on the 0.1 µm PP Resolve Filter (Eichrom, USA), preconditioned with 80 % ethanol before use. The ^{234}Th-free solution worked temporarily until ^{234}Th and ^{234}Pa grew in in the separated uranium, but counting sources are measured in an elapsed time of only 8 hours after preparation, so the β count increase (<1% in the β channel) is negligible taking into account the uncertainty of $c_{\alpha\text{-}\beta}$ values. This solution was tested by preparing counting sources of deionised water spiked with it. Afterwards, counting sources of DW25 and DW26 water samples, spiked with the ^{234}Th-free natural uranium solution were prepared. The $c_{\alpha\text{-}\beta}$ results obtained for deionised water, DW25 and DW26 did not statistically differ as seen in Table 4, but they were lower than the previously obtained using ^{241}Am as a tracer.

Table 4: Cross-talk α-to-β ($c_{\alpha\text{-}\beta}$) results obtained from the measurement of sources prepared with the natural uranium solution.

Dissolution	Water sample	N replicas	t (min)	$c_{\alpha\text{-}\beta}$ (%)
UN-S-NdF	Blank	9	360	30.4(42)
UN-S-NdF	DW25	10	360	38.0(67)
UN-S-NdF	DW26	10	360	30.6(44)

Then, counting sources spiked with the ^{234}Th-free solution from DW27 to DW109 water samples (m_r = 30 mg) were used to calculate the corresponding $c_{\alpha\text{-}\beta}$ values. I_β results were obtained applying the ^{40}K correction, and the $c_{\alpha\text{-}\beta}$ evaluation with the ^{234}Th-free natural uranium solution was shown more reliable than the ones previously obtained applying a constant $c_{\alpha\text{-}\beta}$ value or the $c_{\alpha\text{-}\beta}$ value obtained with ^{241}Am in sources spiked with ^{210}Pb for efficiency calculation. The results obtained reinforce the new approach in the preparation procedure, as shown in Fig. 3, in which I_β determination was more

representative of the real radionuclide content and a better fit to the line $I_\beta = \Sigma_\beta$ was found.

4. Conclusion

The primary target of the current study was to state a robust screening technique which improves the predictive power of gross alpha and gross beta determination to obtain representative results of the real radionuclide content in drinking water samples. Routinely, mass calibration curves for gross counting have been prepared with saline matrices spiked with ^{241}Am or ^{90}Sr standard solutions for efficiency assessment. However, the direct efficiency calculation in the sources prepared from each water sample is a better approach due to the great diversity of saline contents. This work evidenced, likewise, the significance of the similarity among the emission energies of the radionuclides used for efficiency calculation, and the energies of the most common radionuclides dissolved in waters. The gross α/β activities obtained applying the improvements adopted in the method have been directly compared with the sum of the activities of the individual α and β emitters obtained by α-particle and γ-ray spectrometry. The samples were prepared using the evaporation method whose efficiency was determined with a direct standard radionuclide solution spike in the counting sources. The aliquot volume was chosen to accomplish an approximately constant residue mass that ensures small energy loss of the α-particles, improving, at the same time, the homogeneity of residue in the planchet. Natural uranium standard solution has shown to provide reliable I_α and I_β results when the ^{40}K correction is applied for β counting, and direct $c_{\alpha\text{-}\beta}$ evaluation is obtained with a source spiked with a ^{234}Th-free solution derived from the original natural uranium solution.

Acknowledgements

We acknowledge the close cooperation in the development of this work with Enrique Estrada Velez and Roberto Gago Gutiérrez, from the Directorate General of Public Health, Health Department of Castilla y León Government, Spain.

References

EURATOM, 2013. Council Directive 2013/51/Euratom of 22 October 2013 laying down requirements for the protection of the health of the general public concerning radioactive substances in water intended for human consumption.

Fernández-Timón, A., Jurado Vargas, M., Álvarez Gallardo, P., Sánchez-Oro, J., Peralta, L., 2018. ALPHACAL: A new user-friendly tool for the calibration of alpha-particle sources. Appl. Radiat. Isot. 135, 78-82.

García-León, M., García-Montaño, E., Madurga, G., 1984. Characterisation of ^{99}Tc by the shape of its plateau with a gas-flow proportional counter. Int. J. Appl. Radiat. Isot. 35(3), 195-200.

Hallstadius, L., 1984. A method for the electrodeposition of actinides. Nucl. Instrum. Methods Phys. Res. 223, 266-267.

ISO, 2019. ISO 10704; Water quality: measurement of gross α and gross β activity in non-saline water – thin source deposit method. International Organization for Standardization, Geneva, Switzerland.

Jobbágy, V., Wätjen, U., Merešová, J., 2010. Current status of gross α/β activity analysis in water samples: A short overview of methods. J. Radioanal. Nucl. Chem. 286(2), 393-399.

Jobbágy, V., Merešová, J., Wätjen, U., 2014. Critical remarks on gross alpha/beta activity analysis in drinking waters: conclusions from a European interlaboratory comparison. Appl. Radiat. Isot. 87, 429-434.

Lehritani, M., Mantero, J., Casacuberta, N., Masqué, P., García-Tenorio, R., 2012. Comparision of two sequential separation methods for U and Th determination in environmental samples by alpha-particle spectrometry. Radiochim. Acta 100, 431-438.

Montaña, M., Fons, J., Corbacho, J.A., Camacho, A., Zapata-García, D., Guillén, J., Serrano, I., Tent, J., Baeza, A., Llauradó, M., Vallés, I., 2013. A comparative experimental study of gross alpha methods in natural waters. J. Environ. Radioact. 118, 1-8.

Quintana, B., Pedrosa, M.C., Vázquez-Canelas, L., Santamaría, R., Sanjuán, M.A., Puertas, F., 2018. A method for the complete analysis of NORM building materials by γ-ray spectrometry using HPGe detectors. Appl. Radiat. Isot. 134, 470-476.

RD, 2016. Real Decreto 314/2016, de 29 de julio. Boletín Oficial del Estado, 30 de julio de 2016, 183, 53106-53126.

Ruano Sánchez, A.B., Martín Sánchez, A., De la Torre Pérez, J., 2013. Gross α and β indices in water samples revisited. Appl. Radiat. Isot. 81, 136-139.

Santos-Francés, F., Gil Pacheco, E., Martínez-Graña, A., Alonso Rojo, P., Ávila Zarza, C., García Sánchez, A., 2018. Concentration of uranium in the soils of the west of Spain. Environ. Poll. 236, 1-11.

Semkow, T.M., Parekh, P.P., 2001. Principles of gross α and β radioactivity detection in water. Health Phys. 81(5), 567-574.

Ziegler, F., Ziegler, M.D., Biersack, J.P., 2010. SRIM – the stopping and range of ions in matter. Nucl. Instrum. Methods Phys. Res. Sect. B 268, 1818–1823.

Ziegler, J.F., 2019. SRIM.EXE, © 1984-2013, in http://www.srim.org (accessed November 21st 2019).

Uncertainty analysis on the response of a thyroid gamma spectrometer using different calibration phantoms

Mirela Angela Saizu

Horia Hulubei National Institute for Physics and Nuclear Engineering – IFIN HH
30 Reactorului Street, P.O.Box MG-6, 077125 Magurele, Ilfov, Romania

Abstract

A theoretical study of uncertainties of I-131 estimation due to measurement geometry variability of the thyroid monitoring system from IFIN-HH using two physical neck-thyroid phantoms and a male voxel phantom is presented. The code MCNP was used for the calculations. The detector of the thyroid measurement equipment is a shielded and collimated NaI(Tl) detector of 2"x2". The results obtained emphasize the need of appropriate thyroid phantoms in order to achieve accurate and reliable I-131 activity measurement.

Keywords: Monte Carlo, thyroid, phantom, uncertainty, I-131

* Corresponding author: Mirela Angela Saizu, saizu@nipne.ro

1. Introduction

Accurate detector efficiency calibration of *in vivo* monitoring gamma spectrometric systems was always essential to obtain reliable results of the radionuclide activity retained in the whole body or in different target organs (International Organization for Standardization, 2006; International Commission on Radiation Units and Measurements, 2003).

The important role of I-131 in nuclear medicine (International Organization for Standardization, 2016) involves not only refining the detector efficiency calibration methods based on various physical neck-thyroid phantoms, but also the design of these phantoms to be more and more realistic. Phantoms are developed in accordance with the standard specifications regarding the basic anatomical and physical data of the thyroid, its size and shape and the attenuation properties and thickness of the overlaying tissue (International Commission on Radiological Protection, 2002). It is important to have in mind that all the physical phantoms are based on average data resulting from the anatomical variability of the thyroid gland, introducing uncertainty when individuals are measured by using a reference calibration based on average data. Moreover, nowadays, due to the progress of computer tomography and magnetic resonance imaging, voxel phantoms have been developed (International Commission on Radiological Protection, 2009). They are challenging for internal dosimetry because they can describe accurately the anatomy of individuals and they can be used for the calibration of *in vivo* measurement systems (Gómez Ros, 2007) applying Monte Carlo techniques.

The work presented here is a theoretical study of the different sources of uncertainties (International Organization for Standardization, 2011) that can arise in thyroid measurements of the internal contamination resulting from uncertainty of the neck-to-detector distance, the thyroid overlaying tissue thickness and the positioning of the detector with direct effect on the counting efficiency of a thyroid monitoring system and on the accuracy of the monitoring results. Two physical neck-thyroid calibration phantoms designed to have one or two radioactive source inserts equivalent to the two lobes of the thyroid and a male voxel phantom were used for the evaluation of the uncertainties on the response of the thyroid gamma-spectrometer measurement system existing in IFIN-HH, equipped with a NaI(Tl) scintillation detector. The Monte Carlo code MCNP5 (MCNP, 2005) was used for the simulations of the gamma-ray transport in the thyroid and the NaI(Tl) detector.

2. Materials and Methods

2.1 Detection system

The thyroid monitoring system from IFIN-HH uses a chair geometry design and is based on an ORTEC NaI(Tl) scintillation detector that is commonly used for I-131 thyroid monitoring because it can operate at room temperature. The main energy line of I-131 that has to be processed is the 364 keV gamma-ray (International Atomic Energy Agency, 1996). The detector crystal has a 5.08 cm diameter and a length of 5.08 cm and is housed in an aluminum case of 0.05 cm thickness. The scintillator is coupled to an ORTEC – Scintipack™ Photomultiplier Base. The detector is shielded by a 0.55 cm aluminum layer and, additionally, it is equipped with an external cylindrical detector shielding (27 cm length, 0.2 cm thickness and external diameter of 5.1 cm) including a dedicated cone-shaped collimator (lower base diameter of 7 cm, upper base diameter of 9.8 cm and 7.7 cm height) made of lead.

For the calculations of the thyroid detector efficiencies for the three thyroid phantoms, a standard detector position with the detector placed horizontally at mid-height of the thyroid and at 8 cm from the neck was defined.

2.2 Radioactive sources

Two anthropomorphic neck-thyroid phantoms, described in Table 1, and a voxel phantom were used for the numerical evaluation and comparison of detector efficiencies. The ORTEC phantom has one cylindrical thyroid source cavity being equivalent, regarding the efficiency response, with the ANSI/HPS N44.3 thyroid phantom (American National Standard Institute, 1973). The two-lobe phantom (TLP) is a simplified adult physical phantom obtained from a more complex one used in an intercomparison exercise (Project CAThyMARA, 2015), having two cylindrical thyroid source cavities. The inserts for the ORTEC and TLP phantoms simulate a 19 cm^3 thyroid as recommended by ICRP (International Commission on Radiological Protection, 2002).

As computational male voxel phantom, we used the adult voxel phantom Golem (International Commission on Radiological Protection, 2009) with 1.76 m height, 69 kg mass and 0.208x0.208x0.8 cm^3 voxel resolution. Each voxel of the thyroid organ with a volume of 24.5 cm^3 is considered as a radiation source when the thyroid monitoring detector efficiency is computed.

Table 1: Geometric and material parameters of the physical phantoms.

Parameters	ORTEC	TLP
Neck diameter [cm]	10.20	13.00
Neck height [cm]	7.60	13.00
Thyroid Cavity diameter [cm]	2.85	2.20
Thyroid Cavity height [cm]	6.30	7.00
Neck thickness [cm]	1.10	1.50
Distance between thyroid cavities [cm]	-	3.40
Neck material	Lucite – density (1.16 ± 0.03) g	
Thyroid vials material	polyethylene – density (0.92 ± 0.02) g	
Thyroid volume (adult) [mL]	20	
Radionuclide for thyroid sources	I-131	

2.3 Monte Carlo simulation

The Monte Carlo code MCNP5 was used to simulate the photon transport in the 2"x2" NaI(Tl) detector (MCNP, 2005). It is an accurate and reliable code if the physics models are selected appropriately to the application. MCNP5 is able to yield by the F8 tally the detector pulse height per emitted particle in the source that is equivalent to the full-energy peak detector efficiency of the detector, commonly determined experimentally.

The code has extensive cross-section libraries necessary for the simulation of the photon's transport, in a large energy range and in all the considered materials. The detector and phantom models were based on the design provided by the manufacturer. The computational model also included the shielding system around the detector.

The total number of histories was taken large enough to obtain minimum statistical uncertainty associated with the simulation. For a number of 1.0E+06 histories, a maximum value of 2% for the fractional 1-sigma estimated uncertainty in the F8 tally mean was obtained for the I-131 energy line of 364 keV.

Schematic views of the models obtained by the Monte Carlo simulation of the ORTEC and TLP neck-thyroid phantoms, using the data from Table 1, are presented in Fig. 1 and Fig. 2.

A cross-section of the NaI(Tl) detector and of the voxel phantom obtained by MCNP5 using the visual editor is shown in Fig. 3.

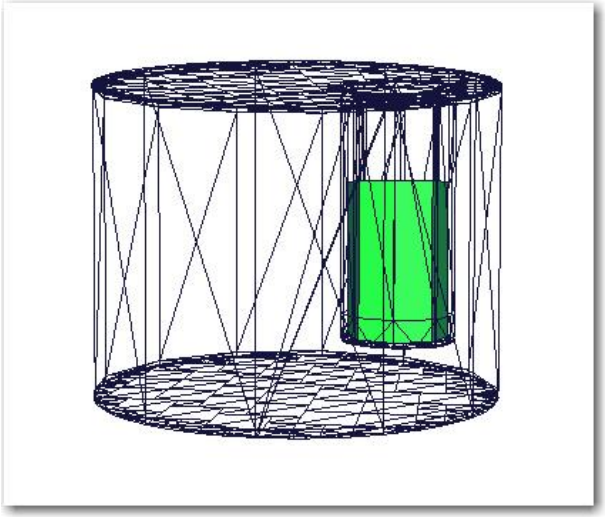

Fig. 1: ORTEC - Neck-thyroid phantom with one cavity. MCNP simulation.

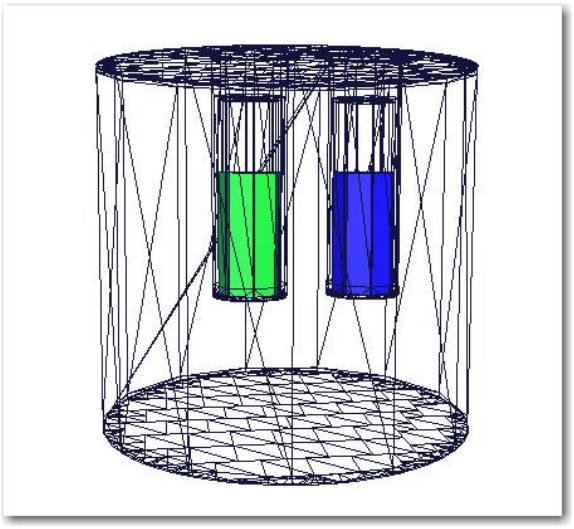

Fig. 2: TLP - Neck-thyroid phantom with two cavities. MCNP simulation.

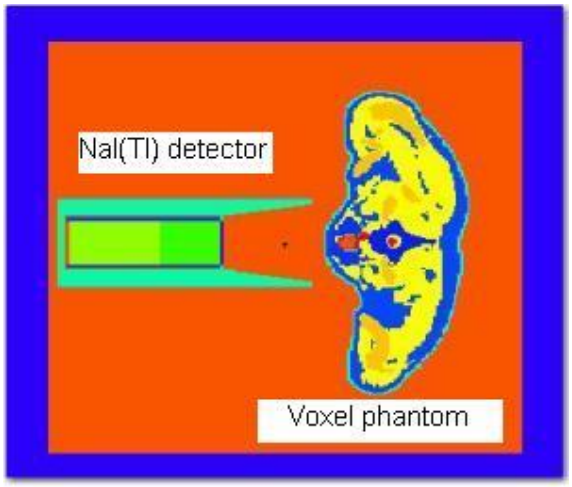

Fig. 3: NaI(Tl) detector with collimator model and voxel phantom cross-section.

3. Results and discussion

A detailed analysis of the effects of the neck-to-detector distance on the counting efficiency, for the 364 keV gamma-ray of I-131, was performed for each phantom. The results are shown in Fig. 4.

The counting efficiencies, for all three phantoms, have the highest value when the collimator and the thyroid neck phantom are in contact and decrease with increasing neck-to-detector distance. The relative differences between the counting efficiencies when the neck-to detector distance is between 10-20 cm and the reference position at 8 cm, for each of the phantoms, were determined. Values ranging from 28.5% to 76.3%, from 27% to 75% and from 24.6% to 75.9%, were obtained for the ORTEC phantom, TLP phantom and for the voxel phantom, respectively. For the TLP thyroid phantom, the counting efficiencies are slightly higher than those of the one cavity thyroid phantom with differences in the range 1.5% to 6.4% with neck-to-detector variations in the range 8 to 20 cm.

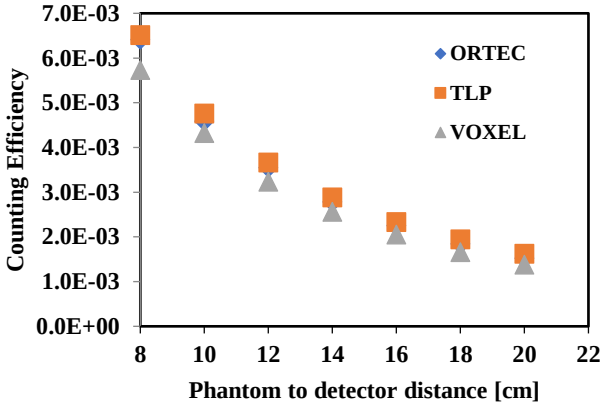

Fig. 4: The counting efficiency at 364 keV as a function of the thyroid phantom neck-to-detector distance for a 0.5 cm thyroid overlaying tissue thickness.

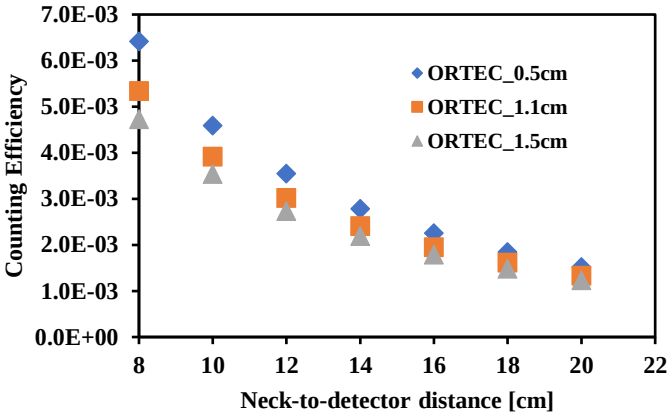

Fig. 5: Variation of the counting efficiency at 364 keV versus ORTEC thyroid phantom neck-to-detector distance for 0.5, 1.1 and 1.5 cm thyroid overlaying tissue thickness.

The counting efficiencies of the voxel phantom are considerably lower than those of the ORTEC and TLP phantoms, with differences between -6% to -12% and -10% to -17% relative to the ORTEC and the TLP phantoms, respectively. This can be explained by the geometrical differences between the physical and voxel phantoms, being known that the physical neck phantoms approximate the real thyroid, using average volumes, overlaying tissue thickness and attenuation tissue factors and contain a uniform distribution of the radionuclide which can be different in a real thyroid. In addition to the variation of the neck-to-detector distance during thyroid monitoring, also vertical positioning effects can occur involving the longitudinal dimension of the phantoms.

Table 2 gives the calculated counting efficiency for the ORTEC, TLP and voxel phantoms for vertical displacements in a range [-1,1] cm relative to the vertical reference position (0 cm-plane). From the results, it can be deduced that the relative efficiency variation is from 0.972 to 0.998, 0.985 to 0.999, and from 0.979 to 0.997 for the ORTEC, TLP and voxel phantoms respectively. The corresponding geometrical relative errors yield 0.2% to 2.8% for the ORTEC phantom, from 0.1% to 1.5% for the TLP phantom and from 0.3% to 2.1% for the voxel phantom.

For the ORTEC phantom, we also studied the effect of the neck overlaying tissue thickness on the counting efficiency. Fig. 5 gives the counting efficiency for I-131 as a function of the neck-to-detector distance for three different values of the thyroid overlaying tissue thickness: 0.5 cm, 1.1 cm and 1.5 cm.

More added tissue means increased attenuation and thyroid-to-detector distance and, consequently, a decreased counting efficiency. An addition of a tissue layer of 0.6 cm and 1 cm to the overlaying tissue thickness of 0.5 cm decreased the counting efficiency with 16.7% and 26.3%, respectively.

Table 3 gives the partial uncertainty budget for I-131 activity determination in the thyroid based on the variability of counting efficiency due to the variability of the measurement geometry in the limits considered for the thyroid monitoring system from IFIN-HH. The rectangular distribution was considered for each parameter and the associated standard uncertainties were combined with the assumption that the sources of uncertainty are independent.

The maximum value of 8.2% for the partial combined standard uncertainty of the measured I-131 activity determined by gamma spectrometry using a NaI (Tl) scintillator detector applies also to the detection limit value of 70 Bq. For workers from nuclear medicine, where I-131 is currently used for therapy, the measured activities of the I-131 retained in the thyroid are much larger than the upper value of the detection limit of the monitoring system. This value can be considered as the total combined standard uncertainty of the measured I-131 activity, because it does not change significantly when considering the uncertainty of the counting statistics of the spectrum analysis (0.3%) and of nuclear data (0.5% for the emission probability of the energy line 364.84 keV of I-131).

Table 2: Variation of the detector efficiency as a function of the vertical displacement of the detector relative to the thyroid phantoms with the reference position at 8 cm.

Phantom \ Shift [cm]	-1	-0.8	-0.6	-0.4	-0.2	0	0.2	0.4	0.6	0.8	1
ORTEC	0.972	0.983	0.986	0.993	0.995	1	0.998	0.992	0.991	0.993	0.989
TLP	0.985	0.992	0.993	0.998	0.998	1	0.999	0.999	0.999	0.998	0.997
VOXEL	0.979	0.986	0.989	0.994	0.996	1	1	1	0.997	0.996	0.994

Table 3: Partial uncertainty budget for I-131 activity determination in the thyroid.

Parameter	Limits of deviation from the reference position	Standard Uncertainty [%]
Neck-to-collimator distance [cm]	0 – 1	0 – 8
Vertical displacement [cm]	±0.5	±0.06
Overlaying tissue thickness [cm]	0 – 0.1	0 – 1.8
Combined Standard Uncertainty		0 – 8.2

4. Conclusions

The Monte Carlo simulations were successfully applied to evaluate the variability of the counting efficiency due to the geometrical variability related to the shape of the source and the attenuation, the detector to source distance. This variability that contributes to the uncertainty of the I-131 measurement was evaluated for the thyroid monitoring system from IFIN-HH using two adult physical neck thyroid phantoms and a male voxel phantom.

The counting efficiencies for the ORTEC and TLP physical thyroid neck phantoms are quite similar, the differences ranging from 1.5% to 6.4% with the variation of neck – to – detector distance from 8 to 20 cm.

The computed counting efficiency based on the adult voxel phantom is lower than the one obtained with the physical phantoms, with maximum values of 12% and 17% relative to the ORTEC phantom and the TLP phantom, respectively, when the detector and the neck thyroid phantom are in contact. These results give some insight into the influence on the counting efficiency of the differences between the physical neck thyroid phantoms and the realistic voxel phantom for adults. The lower counting efficiency for the voxel phantom suggests an increased attenuation of the radiation due to the greater thyroid volume of Golem voxel phantom and of its realistic anatomical shape.

The results obtained in this study showed that the impact of the neck-to-detector distance and overlaying thyroid tissue thickness variation on the counting efficiency are of major importance for the evaluation of I-131 activity in the thyroid. Increasing the neck-to detector distance by 1 cm, changes the counting efficiency by -14%.

When the overlaying tissue thickness for the ORTEC thyroid phantom is increased from 0.5 cm to 1.5 cm, the counting efficiency changes by -26.3%.

For a vertical displacement of the detector by -1cm and +1cm with respect to the reference plane, the counting efficiency changes with -0.2 % respectively -2.8% for the ORTEC phantom, -0.1% respectively -1.5% for the TLP phantom and -0.3% respectively -2.1% for the voxel phantom .

Fixing the ranges in which geometrical parameters (the neck-to-collimator distance, vertical displacement and overlaying tissue thickness) influencing the counting efficiency may deviate from the reference geometry during thyroid measurements, allows estimating the standard uncertainty of the counting efficiency. For I-131 detection in the thyroid a maximum combined standard uncertainty of 8.2% due to variability of the measurement geometry was obtained.

References

American National Standard Institute, 1973 and Health Physics Society. ANSI/HPS N44.3: Thyroid radioiodine uptake measurements using a neck phantom.

Gómez Ros, J. M., Moraleda, M., López, M. A., Navarro, T. and Navarro, J. F., 2007. Monte Carlo based voxel phantoms for in vivo internal dosimetry. Radiat. Prot. Dosimetry 125:161-165.

International Atomic Energy Agency, 1996. Direct methods for measuring radionuclides in the human body. Safety Series No. 114.

International Commission of Radiation Units and Measurements, 2003. Direct Determination of the Body Content of Radionuclides. ICRU Report 69, J. ICRU 3(1).

International Commission on Radiological Protection, 2002. Basic Anatomical and Physiological Data for Use in Radiological Protection. Reference Values. ICRP Publication 89. Ann. ICRP 32 (3-4).

International Commission on Radiological Protection, 2009. Adult Reference Computational Phantoms. ICRP Publication 110. Ann. ICRP 39 (2).

International Organization for Standardization, 2006. ISO 20553: Radiation Protection – Monitoring of workers occupationally exposed to a risk of internal contamination with radioactive material.

International Organization for Standardization, 2011. ISO 27048: Radiation Protection – Dose assessment for the monitoring of workers for internal radiation exposure.

International Organization for Standardization, 2016. ISO 16637: Radiation Protection – Monitoring and internal dosimetry for staff exposed to medical radionuclides as unsealed sources.

MCNP, 2005. MCNP – A General Monte Carlo N-Particle Transport Code, Version 5, Volume 1-3. Los Alamos National Laboratory – Monte Carlo Team, LA-UR-03-1987.

Project CAThyMARA, 2015. Child and adult thyroid monitoring after reactor accident. EU Research Project under the 7th Framework Programme. Contract Nr. OPERRA-604984

The follow-up intercomparison of the radionuclide calibrators between FTMC, CMI and SMU

A. Gudelis[a*], I. Gorina[a], P. Dryak[b], Z. Vesela[b], A. Javornik[c], M. Krivosik[c], J. Ometakova[c], K. Skovorodko[a, d]

[a] Center for Physical Sciences and Technology (FTMC), Metrology Department, Ionizing Radiation Metrology Laboratory, Savanorių Ave. 231, LT-02300 Vilnius, Lithuania
[b] Czech Metrology Institute (CMI), Inspectorate for Ionizing Radiation, Radiova 1, CZ-10227 Praha 10, Czech Republic
[c] Slovak Institute of Metrology (SMU), Karloveska 63, SK-84255 Bratislava 4, Slovak Republic
[d] Vilnius University Hospital Santaros Klinikos, Santariškių 2, LT-08661 Vilnius, Lithuania

Abstract

Measurement standards of CMI, FTMC and SMU have been compared with the secondary standard chamber of CMI for the activity measurement of radionuclides used in nuclear medicine. Radionuclide solutions of ^{18}F, ^{67}Ga, ^{99m}Tc, ^{111}In, ^{123}I, ^{125}I, ^{131}I, ^{201}Tl and ^{223}Ra have been measured in two standard geometries: 10 mL P6 vials from old stock and 5 mL BS ampoules. The discrepancy of 4.2 % from the reference value for ^{111}In measurement with the Capintec-15R in P6 geometry should be investigated further. Results of the participants are consistent with the reference values within a coverage factor of $k = 2$.

Keywords: comparison; radionuclide calibrators; short-lived radionuclides; secondary standard chamber; nuclear medicine; traceability

* Corresponding author, e-mail address: arunas.gudelis@ftmc.lt

1. Introduction

Different radioactive sources and radiopharmaceuticals are extensively used in hospitals for diagnostic and therapeutic purposes (Kim et al., 2005; Tyler et al., 2003). The most widely used radionuclide globally is ^{99m}Tc. It was estimated that more than 80 % of all nuclear medicine procedures are performed using this radionuclide (Vargas et al., 2018). The characteristic feature of the field of nuclear medicine is an extensive application of radiopharmaceuticals around the world: e.g. in 2008, the total number of procedures performed with ^{99m}Tc was about 25-30 million, 6–7 million of those taking place in Europe (Vargas et al., 2018). Currently, according to the World Nuclear Association, over 40 million nuclear medicine examinations are performed each year, and demand for radioisotopes is increasing at up to 5 % annually (Qaim, 2017; WNA, 2019). Meanwhile, the average annual growth of hybrid positron emission tomography with computed tomography (PET/CT) imaging was about 20 % from 2005 to 2013 (Costa et al., 2018; WNA, 2019). In some European countries, the use of PET/CT imaging equipment increased by more than 50 % from 2011 to 2016 (Eurostat, 2018).

In order to reduce the risk of radiopharmaceutical misadministration, it is necessary to ensure that the amount of radioactivity administered to the patient is measured accurately (Zimmerman and Judge, 2007; Ferretti et al., 2018; IAEA, 2019). An accurate and precise measurement of the activity is also important for diagnostic image quality, effective therapy activity, patient dose optimisation, setting the local diagnostic reference levels, and for cross-calibration between imaging modalities (SPECT, PET).

Most measurements of radiopharmaceuticals are carried out using re-entrant ionization chambers (also called ‘dose calibrators’ or ‘radionuclide calibrators’). Such instruments have to be calibrated for the radionuclides to be measured. In accordance with good practice (Gadd et al., 2006), national and international standards (IEC, 1992), guidelines and recommendations, radionuclide calibrators also require regular quality control and annual checks that include measurements traceability through comparisons (IAEA, 2006; Carey et al., 2012; IAEA, 2019).

In 2013, the Ionizing Radiation Metrology Laboratory of the Center for Physical Sciences and Technology (FTMC), together with the Czech Metrology Institute (CMI) organized the comparison of radionuclide calibrators as the EURAMET TC Project No. 1243 (EURAMET, 2016). The activity measurements were performed for the radionuclides (^{18}F, ^{99m}Tc, ^{123}I, ^{131}I, ^{137}Cs) that are most commonly used in routine nuclear medicine practice in Lithuania and Czech Republic. The results showed that consistent, safe and effective radioactivity measurement services to the medicine community are provided. To be in compliance with the ISO/IEC 17025 standard and to ensure the continuation of the services at the appropriate level of quality, a follow-up comparison was proposed in 2018 as the EURAMET TC Project No. 1437 (EURAMET, 2019). A new partner from SMU (Slovakia) joined this comparison. The ionization chambers from FTMC and SMU had been shipped to Prague for the measurements. The measurements were carried out at CMI headquarters in Prague 9-12 April 2018. The target for this comparison was to demonstrate the accuracy of the measurements within 5 % of a reference value.

In this paper, results of the EURAMET TC Project No. 1437 are presented and discussed.

2. Materials and methods

The aim of the comparison was ensuring traceability for activity measurement in both P6 vial and 5 mL BS ampoule geometries of the most common radionuclides used by nuclear medicine departments in hospitals: ^{18}F, ^{67}Ga, ^{99m}Tc, ^{111}In, ^{123}I, ^{125}I, ^{131}I, ^{137}Cs, ^{201}Tl and ^{223}Ra. A secondary standard ionization chamber of CMI was used as the reference standard (CMI 4π γ ionization chamber). Calibration factors for the reference chamber for P6 vial and 5 mL BS ampoule geometries were determined earlier by means of absolute standardization. The purpose to apply the phased-out vials (P6) in this comparison again was the performance check of the radionuclide calibrators which were used in the former comparison for the activity measurements in the P6 vial geometry (EURAMET, 2016).

For this comparison, the short-lived radionuclide solutions were produced in the cyclotron facility in Prague. The solutions of nominal volume of 5 cm^3 were initially provided in the standard P6 vials, the

mass of solutions varied from 5.0 g to 5.2 g. Then, the solutions in P6 geometry had been standardised with the CMI 4π γ ionization chamber prior to the measurements with radionuclide calibrators listed in Table 1. Minimum detectable activities of likely impurities were determined in the solutions by high-resolution gamma-ray spectrometry. Calibration of the radionuclide calibrators themselves was traceable to primary standards, e.g. NPL-published calibration factors were used for both the Fidelis and NPL CRC No. 400001 instruments (Table 1). It should be noted that the NPL CRC and the Fidelis are essentially the same instrument.

Table 1: Radionuclide calibrators used by participants.

Participant	Description of the radionuclide calibrators
CMI	1. NPL CRC No. 400001
	2. Bqmetr 8 No. 02
	3. Bqmetr 8 No. 15
FTMC	1. FIDELIS (NPL chamber) No. 06048
	2. Capintec-CRC 15R No. 158488
SMU	1. VacuTec 70 129 No. 98012 with the steel liner of 2.2 mm, connected to the electrometer Keithley 6517A No. 0695463
	2. Curiementor 2 No. 783-1029, with the chamber No. 233652-1198

Table 2: Activity determined by different radionuclide calibrators of CMI, geometry No. 1 (P6). The CMI 4π instrument is being used as the reference.

Nuclide	CMI 4π γ ionization chamber		Measured activities by different instruments [MBq] (k = 1)		
	Activity [MBq] (k = 1)	Date time	NPL CRC	Bqmetr 8 SN 02	Bqmetr 8 SN 15
^{18}F	297.3 ± 2.7	10.4.2018 12:00	300.9 ± 2.8	295.8 ± 3.1	296.9 ± 2.8
^{67}Ga	469.8 ± 6.6	5.4.2018 12:00	467.0 ± 6.7	476.5 ± 7.8	474.6 ± 6.7
^{99m}Tc	352.2 ± 4.2	11.4.2018 12:00	354.7 ± 4.3	357.9 ± 5.6	359.7 ± 4.4
^{111}In	407.0 ± 3.7	9.4.2018 12:00	412.0 ± 3.8	412.0 ± 5.0	412.0 ± 3.9
^{123}I	107.3 ± 2.0	12.4.2018 12:00	109.7 ± 2.2	107.0 ± 2.2	107.4 ± 2.5
^{131}I	231.0 ± 2.1	4.4.2018 12:00	234.8 ± 2.2	234.8 ± 3.4	234.8 ± 2.2
^{137}Cs	15.08 ± 0.15	1.3.2011 12:00	14.77 ± 0.15	15.07 ± 0.35	15.16 ± 0.16
^{201}Tl	307.8 ± 5.5	9.4.2018 12:00	328.8 ± 6.8	321.1 ± 6.9	317.8 ± 6.8
^{223}Ra	1.226 ± 0.017	12.4.2018 12:00	1.212 ± 0.036	1.172 ± 0.099	1.248 ± 0.022

After the run of measurements with radionuclide calibrators listed in Table 1 in P6 geometry, solutions (except of ^{223}Ra because of its low activity and of ^{137}Cs, which was used as a check source in solid state) were transferred to the standard 5 mL BS ampoules and standardized with the CMI 4π γ ionization chamber again. Still being at CMI, solutions in BS ampoules had been measured by participants with some radionuclide calibrators (Tables 5 and 6) in this new geometry.

At least ten readings of experimental values were taken with each instrument for each radionuclide solution. Every reading was recorded together with the time when the reading was taken. Each individual reading was corrected for the background current. The typical correction for the background was 2 % for ^{223}Ra, 0.4 % for ^{125}I, and was less than 0.03 % for the remaining radionuclides. After the corrections for the background current readings were decay-corrected for a starting time of a measurement run, the mean value and the standard deviation were calculated. The mean value was then decay-corrected to a reference date and time and compared with a reference value. For the decay correction, the half-lives were taken from the Decay Data Evaluation Project (DDEP, 2013). The list of all radionuclide calibrators used in the comparison is presented in Table 1.

3. Results and discussion

Results of activity measurements in P6 vial geometry are shown in Tables 2 to 4 while results of activity measurements in BS ampoule geometry are presented in Tables 5 and 6.

Table 3: Activity determined by different radionuclide calibrators of FTMC, geometry No. 1 (P6). The CMI 4π instrument is being used as the reference.

Nuclide	CMI 4π γ ionization chamber		Measured activities by different instruments [MBq] (k = 1)	
	Activity [MBq] (k = 1)	Date time	Fidelis	Capintec 15R
^{18}F	297.3 ± 2.7	10.4.2018 12:00	297.5 ± 2.9	305.7 ± 3.1
^{67}Ga	469.8 ± 6.6	5.4.2018 12:00	468.9 ± 6.3	465.5 ± 6.3
^{99m}Tc	352.2 ± 4.2	11.4.2018 12:00	356.8 ± 4.3	356.6 ± 4.3
^{111}In	407.0 ± 3.7	9.4.2018 12:00	410.5 ± 3.3	424.1 ± 5.2
^{123}I	107.3 ± 2.0	12.4.2018 12:00	106.6 ± 2.2	107.8 ± 2.2
^{125}I	16.95 ± 0.25	9.4.2018 12:00	16.92 ± 0.35	16.30 ± 0.34
^{131}I	231.0 ± 2.1	4.4.2018 12:00	232.0 ± 2.2	235.6 ± 2.9
^{137}Cs	15.08 ± 0.15	1.3.2011 12:00	14.89 ± 0.16	15.08 ± 0.16
^{201}Tl	307.8 ± 5.5	9.4.2018 12:00	315.0 ± 5.6	307.3 ± 5.5
^{223}Ra	1.226 ± 0.017	12.4.2018 12:00	1.246 ± 0.028	1.231 ± 0.043

One can see from the results of measurements in P6 vial geometry that the largest discrepancy from the reference value was obtained with the ^{201}Tl activity measurement due to the presence of short-lived impurities ^{200}Tl and ^{202}Tl (with half-lives of 1.087 (4) d and 12.24 (3) d respectively).

The relative amount of these two isotopes in ^{201}Tl solution was estimated by gamma-ray spectrometry as 0.16 % and 0.28 %, respectively. Corrections for ^{200}Tl and ^{202}Tl were applied as they had a significant impact on the ^{201}Tl results – e.g. in case of the Fidelis calibrator and the measurement in P6 vial geometry, the discrepancy from the reference value was more than 5 %, and that was unacceptable. The correction led to acceptable results in terms of relative discrepancies from the reference values: for the Fidelis instrument, the discrepancy lowered from 8.6 % to 2.34 %, and from 2.3 % to 0.7 %, for P6 vial and BS ampoule geometries, respectively. The discrepancy value of 2.34 % can be compared with that of 3.3 % obtained for the Fidelis instrument in P6 vial geometry within the previous EURAMET TC Project No. 1243 (EURAMET, 2016). Generally, in case of ^{201}Tl, final results are compatible with the reference value (307.8 ± 5.5) MBq (k = 1) within the coverage factor k = 2 for all radionuclide calibrators.

Table 4: Activity determined by different radionuclide calibrators of SMU, geometry No. 1 (P6). The CMI 4π instrument is being used as the reference.

Nuclide	CMI 4π γ ionization chamber		Measured activities by different instruments [MBq] (k = 1)	
	Activity [MBq] (k = 1)	Date time	Curiementor 2	VacuTec 70 129
^{18}F	297.3 ± 2.7	10.4.2018 12:00	301.3 ± 2.3	300.6 ± 2.0
^{67}Ga	469.8 ± 6.6	5.4.2018 12:00	461.4 ± 6.1	464.0 ± 6.1
^{99m}Tc	352.2 ± 4.2	11.4.2018 12:00	356.0 ± 3.0	353.2 ± 2.5
^{111}In	407.0 ± 3.7	9.4.2018 12:00	411.2 ± 3.1	406.3 ± 2.6
^{123}I	107.3 ± 2.0	12.4.2018 12:00	109.4 ± 1.4	108.99 ± 0.87
^{125}I	16.95 ± 0.25	9.4.2018 12:00	17.29 ± 0.17	*
^{131}I	231.0 ± 2.1	4.4.2018 12:00	231.1 ± 2.0	230.1 ± 1.8
^{137}Cs	15.08 ± 0.15	1.3.2011 12:00	15.07 ± 0.18	15.21 ± 0.22
^{201}Tl	307.8 ± 5.5	9.4.2018 12:00	302.4 ± 3.5	304.5 ± 3.3
^{223}Ra	1.226 ± 0.017	12.4.2018 12:00	1.256 ± 0.041	1.251 ± 0.029

Remark: * - not measured due to relatively thick liner

Another significant discrepancy of 4.2 % from the reference value was obtained in case of ^{111}In activity measurement by the Capintec-15R in the P6 vial geometry (Table 3). This result is consistent with the former determination obtained within the EURAMET TC Project No. 1243 (EURAMET, 2016) when the discrepancy for the ^{111}In activity measurement in the same conditions was 5.9 %. However, the instrument had been calibrated by the manufacturer using ^{111}In in BS ampoules, so the difference may be due to the different containers used. The instrument should be recalibrated using the same container for both the reference solution and the sample, and further investigations carried out if this does not resolve the discrepancy.

Table 5: Activity determined by different radionuclide calibrators of FTMC, geometry No. 2 (BS). The CMI 4π instrument is being used as the reference.

Nuclide	CMI 4π γ ionization chamber		Measured activities by different instruments [MBq] (k = 1)	
	Activity [MBq] (k = 1)	Date time	Fidelis	Capintec 15R
^{18}F	292.2 ± 2.7	10.4.2018 12:00	*	*
^{67}Ga	463.3 ± 6.6	5.4.2018 12:00	463.6 ± 6.6	464.4 ± 6.6
^{99m}Tc	347.9 ± 4.2	11.4.2018 12:00	351.2 ± 4.4	354.7 ± 4.4
^{111}In	399.1 ± 3.7	9.4.2018 12:00	399.2 ± 3.7	398.4 ± 3.7
^{123}I	106.1 ± 2.0	12.4.2018 12:00	106.8 ± 2.0	105.4 ± 2.0
^{125}I	16.88 ± 0.25	9.4.2018 12:00	16.98 ± 0.32	16.91 ± 0.26
^{131}I	228.1 ± 2.1	4.4.2018 12:00	228.5 ± 2.1	228.0 ± 2.1
^{201}Tl	304.3 ± 5.5	9.4.2018 12:00	302.3 ± 5.5	305.8 ± 5.5

Remark: * - not measured

Table 6: Activity determined by different radionuclide calibrators of SMU, geometry No. 2 (BS). The CMI 4π instrument is being used as the reference.

Nuclide	CMI 4π γ ionization chamber		Measured activities by different instruments [MBq] (k = 1)	
	Activity [MBq] (k = 1)	Date time	Curiementor 2	VacuTec 70 129
^{18}F	292.2 ± 2.7	10.4.2018 12:00	*	*
^{67}Ga	463.3 ± 6.6	5.4.2018 12:00	463.6 ± 6.6	464.4 ± 6.6
^{99m}Tc	347.9 ± 4.2	11.4.2018 12:00	351.2 ± 4.4	354.7 ± 4.4
^{111}In	399.1 ± 3.7	9.4.2018 12:00	399.2 ± 3.7	398.4 ± 3.7
^{123}I	106.1 ± 2.0	12.4.2018 12:00	106.8 ± 2.0	105.4 ± 2.0
^{125}I	16.88 ± 0.25	9.4.2018 12:00	16.98 ± 0.32	16.91 ± 0.26
^{131}I	228.1 ± 2.1	4.4.2018 12:00	228.5 ± 2.1	228.0 ± 2.1
^{201}Tl	304.3 ± 5.5	9.4.2018 12:00	302.3 ± 5.5	305.8 ± 5.5

Remark: * - not measured due to relatively thick line

Table 7: Uncertainty components quadratically added for the radionuclide activity measurement in P6 vials (for the case of the Fidelis instrument).

Nuclide	Uncertainty component (%) due to:					Combined standard uncertainty (%) at $k = 1$
	Repeatability	Background	Impurities	Reference activity of a solution	Half-life (DDEP, 2013)	
^{18}F	0.156	0.002	0.1	0.908	0.013	0.93
^{67}Ga	0.056	0.03	0.1	1.405	0.016	1.41
^{99m}Tc	0.04	0.012	0.1	1.193	0.017	1.21
^{111}In	0.048	0.008	0.1	0.909	0.015	0.92
^{123}I	0.066	0.08	0.1	1.864	0.028	1.87
^{125}I	1.365	0.42	0.1	1.475	0.048	2.06
^{131}I	0.04	0.03	0.1	0.909	0.024	0.92
^{137}Cs	0.02	0.02	0.1	1.0	0.267	1.04
^{201}Tl	0.073	0.012	0.3	1.787	0.056	1.81
^{223}Ra	1.409	0.33	0.1	1.387	0.263	2.02

The remaining results of the comparison are in good agreement with the reference values (within the coverage factor $k = 1$). As an example of the uncertainty budget typical for this comparison, the budget for the Fidelis instrument is shown in Table 7. For other devices, the uncertainty components for the half-life, the reference activity of a solution and the impurities remain the same, whereas the repeatability and the background may vary.

4. Conclusions

The activities of the short-lived radionuclides used in nuclear medicine have been measured with different instruments from National Metrology Institutes of the Czech Republic, Lithuania and Slovakia during the implementation of the EURAMET TC Project No. 1437 "The follow-up interlaboratory comparison of the radionuclide calibrators": ^{18}F, ^{67}Ga, ^{99m}Tc, ^{111}In, ^{123}I, ^{125}I, ^{131}I, ^{201}Tl and ^{223}Ra. Radionuclide solutions have been measured in two standard geometries: 10 mL P6 vials and 5 mL BS ampoules. The comparison revealed the necessity to correct for impurities in case of ^{201}Tl activity measurement due to the significant impact of ^{200}Tl and ^{202}Tl on the results. A significant discrepancy of 4.2 % was observed in activity measurements with the Capintec-15R instrument for ^{111}In samples in P6 vials. Since the instrument had been calibrated using BS ampoules, the difference may be due to the different containers used. Recalibration of the instrument should be performed using the same container for both reference solution and sample. If this does not resolve the discrepancy, further investigations need to be carried out. Generally, results of the participants are consistent with the reference values within the coverage factor $k = 2$ for all radionuclides measured in both geometries.

Acknowledgements

This comparison was financially supported by the Lithuanian Ministry of Economy, Program for Enlargement of Economy Development and Competitiveness (Project number 5100-P153).

References

Carey, J. E., Byrne, P., DeWerd, L., Lieto, R., Petry, N. 2012. The Selection, Use, Calibration, and Quality Assurance of Radionuclide Calibrators Used in Nuclear Medicine. American Association of Physicists in Medicine, Report No. 181, College Park, MD. ISSN: 0271-7344.

Costa, P., Reinhardt, M., Poppe, B. 2018. Occupational exposure from F-18-FDG PET/CT: implementation to routine clinical practice. Radiat. Prot. Dosim. 179(3), 291-298.

DDEP, 2013. Decay Data Evaluation Project. <http://www.nucleide.org/DDEP_WG/DDEPdata.htm>. Accessed 18/11/2019.

EURAMET, 2016. Euramet TC Project Nr. 1243 "The interlaboratory comparison of the radionuclide calibrators". Final report.

EURAMET, 2019. Euramet TC Project Nr. 1437 "The follow-up interlaboratory comparison of the radionuclide calibrators". Final report.

Eurostat, 2018. Healthcare resource statistics – technical resources and medical technology. European Comission. <https://ec.europa.eu/eurostat/statistics-explained/index.php?title=File:Use_of_imaging_equipment_%E2%80%94_number_of_PET_scans,_2011_and_2016_(per_100_000_inhabitants)_HLTH18.png>.Accessed 20/11/2019.

Ferretti, A., Chondrogiannis, S., Rampin, L., Bellan, E., Marzola, M. C., Grassetto, G., Gusella, S., Maffione, A. M., Gava, M., Rubello, D. 2018. How to harmonize SUVs obtained by hybrid PET/CT scanners with and without point spread function correction. Phys. Med. Biol. 63(23):235010.

Gadd, R., Baker, M., Nijzan, K. S., Owens, S., Thomson, W., Woods, M. J., Zananiri, F. 2006. Protocol for Establishing and Maintaining the Calibration of Medical Radionuclide Calibrators and their Quality Control. NPL Measurement Good Practice Guide No. 93, Teddington, Middlesex, UK.

IAEA, 2019. International Atomic Energy Agency, Human Health Campus. <https://humanhealth.iaea.org/HHW/MedicalPhysics/NuclearMedicine/QualityAssurance/Radioactivitycalibrators/index.html>. Accessed 06/03/2019.

IAEA, 2006. Quality Assurance for Radioactivity Measurement in Nuclear Medicine. International Atomic Energy Agency, Technical Reports Series No. 454, Vienna, Austria.

IEC, 1992. Calibration and use of ionization chamber systems for assay of radionuclides. International Electrotechnical Commission, IEC 61145, Geneva, Switzerland.

Kim, G.-Y., Lee, H.-K., Jeong, H. K., Woods, M. J. 2005. Comparison of radioactivity measurements with radionuclide calibrators in the Republic of Korea. Appl. Radiat. Isot. 63, 201–205.

Qaim, S. M. 2017. Nuclear data for production and medical application of radionuclides: Present status and future needs. Nucl. Med. Biol. 44, 31-49.

Tyler, D. K., Baker, M. I., Woods, M. J. 2005. Comparison of Strontium-89 Solution Sources in UK Hospitals, 2003. NPL Report DQL-RN 012.

Vargas, C. S., Pérez, S. R., Baete, K., Pommé, S., Paepen, J., Van Ammel, R., Struelens, L. 2018. Intercomparison of ^{99m}Tc, ^{18}F and ^{111}In activity measurements with radionuclide calibrators in Belgian hospitals. Phys. Med. 45, 134-142.

WNA, 2019. World Nuclear Association. <http://www.world-nuclear.org/information-library/non-power-nuclear-applications/radioisotopes-research/radioisotopes-in-medicine.aspx>. Accessed 06/03/2019.

Zimmerman, B. E., Judge, S. 2007. Traceability in nuclear medicine. Metrologia 44, S127.

Appendix

Conference papers published in *Applied Radiation and Isotopes*

Session: Alpha- and Beta-particle Spectrometry

M. Marouli, S. Pommé, Automated optical distance measurements for counting at a defined solid angle, https://doi.org/10.1016/j.apradiso.2019.108821 ..... vol. 153, 2019

S. Pommé, J. Paepen, M. Marouli, Conversion electron spectroscopy of the 59.54 keV transition in ^{241}Am alpha decay, https://doi.org/10.1016/j.apradiso.2019.108848 ..... vol.153, 2019

E. García-Toraño, T. Crespo, M. Marouli, V. Jobbágy, S. Pommé, P. Ivanov, Alpha-particle emission probabilities of ^{231}Pa derived from first semiconductor spectrometric measurements, https://doi.org/10.1016/j.apradiso.2019.108863 .. .. vol. 154, 2019

A. Singh, X. Mougeot, B. Sabot, D. Lacour, A. Nourreddine, Beta spectrum measurements using a quasi-4π detection system based on Si detectors, https://doi.org/10.1016/j.apradiso.2019.108897 ..... vol. 154, 2019

M. Loidl, J. Beyer, L. Bockhorn, C. Enss, S. Kempf, K. Kossert, R. Mariam, O. Nähle, M. Paulsen, P. Ranitzsch, M. Rodrigues, M. Schmidt, Beta spectrometry with metallic magnetic calorimeters in the framework of the European EMPIR project MetroBeta, https://doi.org/10.1016/j.apradiso.2019.108830 ..... vol. 153, 2019

Session: Gamma-ray Spectrometry

H. Paradis, C. Bobin, J. Bobin, J. Bouchard, V. Lourenço, C. Thiam, R. André, L. Ferreux, A. de Vismes Ott, M. Thévenin, Spectral unmixing applied to fast identification of γ-emitting radionuclides using NaI(Tl) detectors, https://doi.org/10.1016/j.apradiso.2020.109068 ..... vol. 158, 2020

O. Sima, A. De Vismes Ott, M.S. Dias, P. Dryak, L. Ferreux, D. Gurau, S. Hurtado, P. Jodlowski, K. Karfopoulos, M.F. Koskinas, M. Laubenstein, Y.K. Lee, M.C. Lépy, A. Luca, M.O. Menezes, D.S. Moreira, J. Nikolič, V. Peyres, P. Saganowski, M.I. Savva, R. Semmler, J. Solc, T.T. Thanh, K. Tyminska, Z. Tyminski, T. Vidmar, I. Vukanac, H.Yücel, Consistency test of coincidence-summing calculation methods for extended sources, https://doi.org/10.1016/j.apradiso.2019.108921 ..... vol. 155, 2020

M.C. Lépy, C. Thiam, M. Anagnostakis, R. Galea, D. Gurau, S. Hurtado, K. Karfopoulos, J. Liang, H. Liu, A. Luca, I. Mitsios, C. Potiriadis, M.I. Savva, T.T. Thanh, V. Thomas, R.W. Townson, T. Vasilopoulou, M. Zhang, A benchmark for Monte Carlo simulation in gamma-ray spectrometry, https://doi.org/10.1016/j.apradiso.2019.108850 ..... vol. 154, 1919

N.M. Murphy, L. León Vintró, C.I. Burbidge, L. Currivan, An automated programme for the optimisation of HPGe detector parameters using an evolutionary algorithm with GESPECOR, https://doi.org/10.1016/j.apradiso.2019.108883 ..... vol. 156, 2020

B.J. Kim, K.B. Lee, J.M. Lee, S.H. Hwang, D.H. Heo, K.H. Han, Design of optimal digital filter and digital signal processing for a CdZnTe high resolution gamma-ray system, https://doi.org/10.1016/j.apradiso.2020.109171, ... vol. 162, 2020

J. Xu, J. Bobin, A. de Vismes Ott, C. Bobin, Sparse spectral unmixing for activity estimation in γ-ray spectrometry applied to environmental measurements, https://doi.org/10.1016/j.apradiso.2019.108903 ..... vol. 156, 2020

Session: Source Preparation Techniques

M.C. Ferrari, V. Peyres, N. Navarro, M.P. Rossi, G. Cerutti, M. Mejuto, T. Crespo, On the equivalence between homogeneously prepared sources and sources prepared by seeding in

layers for different geometries, energies and matrix parameters,
https://doi.org/10.1016/j.apradiso.2019.108894 ..... vol. 154, 2019

R. Galea, K. Moore, Production of a carrier-free standard ^{56}Mn source for the NRC manganese salt bath, https://doi.org/10.1016/j.apradiso.2019.108896 ..... vol. 154, 2019

Session: Measurement Standards and Reference Materials

F. Mertes, S. Röttger, A. Röttger, A new primary emanation standard for Radon-222,
https://doi.org/10.1016/j.apradiso.2019.108928 ..... vol. 156, 2020

B. Sabot, M. Rodrigues, S. Pierre, Experimental facility for the production of reference atmosphere of radioactive gases (Rn, Xe, Kr, and H isotopes),
https://doi.org/10.1016/j.apradiso.2019.108934 ..... vol. 155, 2020

Session: Low-level Radioactivity Measurement Techniques

M. Hult, M. Charette, G. Lutter, G. Marissens, P. Henderson, K. Sobiech-Matura, H. Simgen, Underground gamma-ray measurements of radium isotopes from hydrothermal plumes in the deep Pacific Ocean, https://doi.org/10.1016/j.apradiso.2019.108831 ..... vol. 153, 2019

V. Thomas, O. Delaune, G. Le Petit, J.P. Fontaine, The Mobile Analyzer of Radioactive Gases OuTflows (MARGOT): A promising environmental xenon radionuclides detection system,
https://doi.org/10.1016/j.apradiso.2019.108820 ..... vol. 153, 2019

F.J. Maringer, H. Wiedner, F. Cardellini, An innovative quick method for traceable measurement of radon 222 in drinking water, https://doi.org/10.1016/j.apradiso.2019.108907 ..... vol. 155, 2020

M.C. Pedrosa-García, M. Fontela, B. Quintana, F. Pérez, G. Francés, T. Marcos, Precise ^{210}Pb determination with high-efficiency gamma spectrometry for dating of marine sedimentary cores,
https://doi.org/10.1016/j.apradiso.2019.108962 ..... vol. 156, 2020

Session: Liquid Scintillation Counting Techniques

D.E. Bergeron, J.T. Cessna, R. Fitzgerald, L. Pibida, B.E. Zimmerman, Standardization of I-124 by three liquid scintillation-based methods,
https://doi.org/10.1016/j.apradiso.2019.108849 ..... vol. 154, 2019

Haoran Liu, Qianqian Zhou, Fuyou Fan, Juncheng Liang, Ming Zhang, Activity determination of ^{231}Pa by means of liquid scintillation counting,
https://doi.org/10.1016/j.apradiso.2019.108944 ..... vol. 155, 2020

M.P. Takács, K. Kossert, O.J. Nähle, Standardisation of ^{85}Sr with digital anticoincidence counting and half-life determination of the 514 keV level of ^{85}Rb,
https://doi.org/10.1016/j.apradiso.2019.07.004 ..... vol. 153, 2019

Ch. Dutsov, K. Mitev, P. Cassette, V. Jordanov, Study of two different coincidence counting algorithms in TDCR measurements,
https://doi.org/10.1016/j.apradiso.2019.108895 ..... vol. 154, 2019

W.M. van Wyngaardt, S.M. Tobin, S. Lee, M.L. Smith, T.W. Jackson, J. Ilter, B. Howe, A. Sarbutt, Primary standardisation of technetium-99m by liquid scintillation coincidence counting,
https://doi.org/10.1016/j.apradiso.2019.108935 ..... vol. 156, 2020

Session: Radionuclide Metrology Techniques

V.H. Elvira, V. Peyrés, M. Roteta, A. Fernández-Sotillo, E. García-Toraño, Absolute determination of low-energy X-ray emission rates with a proportional counter,
https://doi.org/10.1016/j.apradiso.2020.109113 ..... vol. 160, 2020

Y. Seon, S.H. Hwang, J.M. Lee, K.B. Lee, D.H. Heo, M.J. Han, H.J. Kim, The primary system for measurement of beta emitting radioactive gases at KRISS, https://doi.org/10.1016/j.apradiso.2020.109238 ..... vol. 164, 2020

K. Mitev, P. Cassette, D. Pressyanov, S. Georgiev, C. Dutsov, N. Michielsen, B. Sabot, Methods for the experimental study of ^{220}Rn homogeneity in calibration chambers, https://doi.org/10.1016/j.apradiso.2020.109259 ..... vol. 165, 2020

I.M. Yamazaki, M.F. Koskinas, D.S. Moreira, R. Semmler, F. Brancaccio, M.S. Dias, Primary standardization and determination of gamma ray emission intensities of Ho-166, https://doi.org/10.1016/j.apradiso.2020.109237 ..... vol. 164, 2020

R. Fitzgerald, L. King, Accurate integral counting using multi-channel analyzers, https://doi.org/10.1016/j.apradiso.2020.109101 ..... vol. 159, 2020

R.S. Gomes, J.U. Delgado, C.J. da Silva, R.L. da Silva, P.A.L. da Cruz, A.L. Ferreira Filho, M.C.M. de Almeida, A. Iwahara, A.E. de Oliveira, L. Tauhata, Measurement of the absolute gamma emission intensities from the decay of Th-229 in equilibrium with progeny, https://doi.org/10.1016/j.apradiso.2020.109323 ..... vol. 166, 2020

M.T. Durán, Y. Nedjadi, F. Juget, F. Bochud, C. Bailat, Evaluation of digital pulse processing techniques for a β-γ coincidence counting system, https://doi.org/10.1016/j.apradiso.2020.109100 ..... vol. 159, 2020

T. Yamada, Y. Sato, A. Yunoki, Y. Kawada, α-particle discrimination in the measurement of α/β decaying chains by the use of ultra-thin plastic scintillation sheets, https://doi.org/10.1016/j.apradiso.2020.109069 ..... vol. 159, 2020

T. Ziemek, R. Broda, T. Dziel, A. Listkowska, Z. Tymiński, A new coincidence module using pulse-mixing method applied in the 4π(LS)-γ coincidence system with TDCR detector, https://doi.org/10.1016/j.apradiso.2020.109081 ..... vol. 159, 2020

T. Ziemek, O. J. Nähle, K. Kossert, S. Leschitzki, M.P. Takács, R. Broda, A.Listkowska, Z. Tymiński, T. Dziel, Comparison of digital coincidence modules used at POLATOM and PTB for TDCR and $4\pi\beta$(LS)-γ coincidence counters, https://doi.org/10.1016/j.apradiso.2020.109231.... vol. 164, 2020

A. Arinc, J.D. Keightley, Standardisation of ^{231}Pa by defined solid angle and liquid scintillation methods at NPL, https://doi.org/10.1016/j.apradiso.2020.109102 ..... vol. 160, 2020

R. Fitzgerald, D.E. Bergeron, S.P. Giblin, D.G. Jarrett, S.M. Judge, C. Michotte, H. Scherer, N.M. Zimmerman, The next generation of current measurement for ionization chambers, https://doi.org/10.1016/j.apradiso.2020.109216 ..... vol. 163, 2020

S.H. Hwang, M.J. Han, Y.G. Seon, J.M. Lee, K.B. Lee, Development of a high-sensitivity radon monitor for a radon calibration system at KRISS, https://doi.org/10.1016/j.apradiso.2020.109228 ..... vol. 164, 2020

Session: Quality Assurance and Uncertainty Evaluation in Radioactivity Measurements

M.C. Ali Santoro, M.J. Anagnostakis, T. Boshkova, A. Camacho, M.C. Fornaciari Iljadica, S.M. Collins, R. Diaz Perez, J.U. Delgado, M. Đurašević, M.A. Duch, V.H. Elvira, R.S. Gomes, A. Gudelis, D. Gurau, S. Hurtado Bermudez, R. Idoeta, A. Jevremović, A. Kandić, M. Korun, K. Karfopolous, M. Laubenstein, S. Long, R.M. Margineanu, I. Mitsios, D. Mulas, J.K. Nikolić, A.Pantelica, V. Peyres Medina, L. Pibida, C. Potiriadis, R.L. Silva, S. Siri, B. Šešlak, L. Verheyen, B. Vodenik, I. Vukanac, H. Wiedner, B. Zorko, Determining the probability of locating peaks using computerized peak-location methods in gamma-ray spectra as a function of the relative peak-area uncertainty, https://doi.org/10.1016/j.apradiso.2019.108920 ..... vol. 155, 2020

D. Glavič-Cindro, E. Hazou, M. Korun, R. Krištof, P. Osterman, T. Petrovič, B. Vodenik, B.Zorko, Measurement uncertainty arising from sampling of environmental samples, https://doi.org/10.1016/j.apradiso.2019.108978 ..... vol. 156, 2020

Session: Nuclear Decay Data

P. Dryák, J. Šolc, Measurement of the branching ratio related to the internal pair production of Y-90, https://doi.org/10.1016/j.apradiso.2019.108942 ..... vol. 156, 2020

L. Pibida, B.E. Zimmerman, L. King, R. Fitzgerald, D.E. Bergeron, E. Napoli, J.T. Cessna, Determination of the internal pair production branching ratio of ^{90}Y, https://doi.org/10.1016/j.apradiso.2019.108943 ..... vol. 156, 2020

X. Mougeot, Towards high-precision calculation of electron capture decays, https://doi.org/10.1016/j.apradiso.2019.108884 ..... vol. 154, 2019

M.A. Kellett, L. Vio, C. Bobin, L. Brondeau, M. Cardot-Martin, H. Isnard, D. Lacour, M.-C. Lépy, V. Lourenço, M. Marie, C. Thiam, Measurement of the absolute gamma-ray emission intensities from the decay of ^{147}Nd, https://doi.org/10.1016/j.apradiso.2020.109349.....vol. 166, 2020

C. Thiam, C. Dulieu, X. Mougeot, A. Nair, C. Bobin, M.A. Kellett, Nuclide++: A C++ module to include DDEP recommended radioactive decay data in Geant4, https://doi.org/10.1016/j.apradiso.2019.108964 ..... vol. 156, 2020

A. Luca, ^{226}Th nuclear decay data evaluation, https://doi.org/10.1016/j.apradiso.2019.108941 ..... vol. 155, 2020

J. Riffaud, M.-C. Lépy, P. Cassette, M. Corbel, M.A. Kellett, V. Lourenço, Measurement of the absolute gamma-ray emission intensities from the decay of ^{103}Pd, https://doi.org/10.1016/j.apradiso.2020.109298 ..... vol. 167, 2021

A.J. Fenwick, S.M. Collins, W.D. Evans, K.M. Ferreira, S.J. Paisey, A.P. Robinson, C. Marshall, Absolute standardisation and determination of the half-life and gamma emission intensities of ^{89}Zr, https://doi.org/10.1016/j.apradiso.2020.109294 ..... vol. 166, 2020

Session: Aspects of International Metrology

L. Karam, S. Judge, W. Louw, The international measurement system for radionuclide metrology: A strategy for the future, https://doi.org/10.1016/j.apradiso.2019.108838 ..... vol. 154, 2019

S. Pierre, C. Thiam, P. Cassette, X. Mougeot, A. Singh, Simulation of the response of an ionization chamber to ^{214}Bi emission. Application to the measurement of ^{222}Rn, https://doi.org/10.1016/j.apradiso.2019.108886 ..... vol. 154, 2019

Session: Intercomparisons

S. Jerome, C. Bobin, P. Cassette, R. Dersch, R. Galea, H. Liu, A. Honig, J. Keightley, K. Kossert, J. Liang, M. Marouli, C. Michotte, S. Pommé, S. Röttger, R. Williams, M. Zhang, Half-life determination and comparison of activity standards of ^{231}Pa, https://doi.org/10.1016/j.apradiso.2019.108837 ..... vol. 155, 2020

R. Galea, C. Michotte, M. Nonis, K. Moore, El Gamal, J. Keightley, A. Fenwick, The first official measurement of ^{11}C in the SIRTI, https://doi.org/10.1016/j.apradiso.2019.108834 vol. 154, 2019

V. Jobbágy, H. Stroh, G. Marissens, V. Gruber, D. Roth, S. Willnauer, M. Bernreiter, H. von Philipsborn, M. Hult, Evaluation of a radon-in-water pilot-proficiency test, https://doi.org/10.1016/j.apradiso.2019.108836 ..... vol. 153, 2019

K. Sobiech-Matura, G. Lutter, R. Van Ammel, G. Marissens, M. Hult, H. Emteborg, Evaluation of a proficiency test of ^{131}I, ^{134}Cs and ^{137}Cs in maize powder, https://doi.org/10.1016/j.apradiso.2020.109156, ... vol. 162, 2020

International Committee for Radionuclide Metrology (ICRM)
Ljubljana, Slovenia, 2020

ICRM technical series on radionuclide metrology – ISSN 2522-4328
URL: https://physics.nist.gov/ICRM/ICRM_technicalseries_2.pdf

Title of this issue:
Proceedings of the 22nd International Conference on Radionuclide Metrology and its Applications (ICRM 2019), 27-31 May 2019, Salamanca, Spain
Editors: Uwe Wätjen, Begoña Quintana Arnés and Eduardo García-Toraño
2020

The International Committee for Radionuclide Metrology (ICRM) is an association of radionuclide metrology laboratories whose membership is composed of delegates of these laboratories together with other scientists (associate members) actively engaged in the study and applications of radioactivity.

It explicitly aims at being an international forum for the dissemination of information on techniques, applications and data in the field of radionuclide metrology. This discipline provides a range of tools for tackling a wide variety of problems in numerous other fields, for both basic research and industrial applications. Radionuclide metrology continues to play an important role in the nuclear industry, supporting activities such as radionuclide production, nuclear medicine, measurement of environmental radioactivity and of radionuclides in food and drinking water, decommissioning of nuclear facilities, nuclear security and emergency preparedness, nuclear physics research, etc.